Leibniz-Institut für Astrophysik Potsdam

Dynamics of the rise of magnetic flux tubes in stellar interiors

A numerical study of compressible non-axisymmetric flux tubes

Dissertation
zur Erlangung des akademischen Grades
"doctor rerum naturalium"
(Dr. rer. nat.)
in der Wissenschaftsdisziplin Astrophysik

eingereicht an der
Mathematisch-Naturwissenschaftlichen Fakultät
der Universität Potsdam

von
Yori Fournier

Potsdam, den 20. Juni 2016

Published online at the
Institutional Repository of the University of Potsdam:
URN urn:nbn:de:kobv:517-opus4-394533
http://nbn-resolving.de/urn:nbn:de:kobv:517-opus4-394533

pour Mamie Odette et Papi Alain

Zusammenfassung

In sonnenähnlichen Sternen erhält ein Dynamo-Mechanismus die Magnetfelder. Der Babcock-Leighton-Dynamo beruht auf einem solchen Mechanismus und erfordert insbesondere die Existenz von magnetischen Flussröhren. Man nimmt an, dass magnetische Flussröhren am Boden der Konvetionszone entstehen und durch Auftrieb bis zur Oberfläche steigen. Es wird ein spezielles Dynamomodell vorgeschlagen, in dem der Verzögerungseffekt durch das Aufsteigen der Flussröhren berücksichtigt wird.

Die vorliegende Dissertation beschäftigt sich mit der Anwendbarkeit des Babcock-Leighton-Dynamos auf andere Sterne. Zu diesem Zweck versuchen wir, die Aufstiegszeiten von magnetischen Flussröhren mit Hilfe von kompressiblen MHD-Simulationen in spärischen Kugelschalen mit Dichteschichtung zu bestimmen und einzugrenzen.

Derartige Simulationen sind allerdings nur in einem unrealistischen Parameterbereich möglich. Deshalb ist eine Skalierungsrelation nötig, die die Ergebnisse auf realistische physikalische Regimes überträgt. Wir erweitern frühere Arbeiten zu Skalierungsrelationen in 2D und leiten ein allgemeines Skalierungsgesetz ab, das für 2D- und 3D-Flussröhren gültig ist. In einem umfangreichen Satz von numerischen Simulationen zeigen wir, dass die abgeleitete Skalierungsrelation auch im vollständig nichtlinearen Fall gilt. Wir haben damit ein Gesetz für die Aufstiegszeit von magnetischen Flussröhren gefunden, dass in jedem sonnenähnlichen Stern Gültigkeit hat. Schließlich implementieren wir dieses Gesetz in einem Dynamomodell mit Verzögerungsterm.

Die Simulationen eines solchen verzögerten Flussröhren/Babcock-Leighton-Dynamos auf der Basis der Meanfield-Formulierung führten auf ein neues Dynamo-Regime, das nur bei Anwesenheit der Verzögerung existiert. Die erforderlichen Verzögerungen sind von der Größenordnung der Zykluslänge, die resultierenden Magnetfelder sind schwächer als die Äquipartitions-Feldstärke. Dieses neue Regime zeigt, dass auch bei sehr langen Aufstiegszeiten der Flussröhren/Babcock-Leighton-Dynamo noch nichtzerfallende Lösungen liefern und daher auf ein breites Spektrum von Sternen anwendbar sein kann.

Abstract

Solar-like stars maintain their magnetic fields thanks to a dynamo mechanism. The *Babcock-Leighton* dynamo is one possible dynamo that has the particularity to require magnetic flux tubes. Magnetic flux tubes are assumed to form at the bottom of the convective zone and rise buoyantly to the surface. A delayed dynamo model has been suggested, where the delay accounts for the rise time of the magnetic flux tubes; a time, that has been ignored by former studies.

The present thesis aims to study the applicability of the *flux tube/Babcock-Leighton dynamo* to other stars. To do so, we attempt to constrain the rise time of magnetic flux tubes thanks to the first fully compressible MHD simulations of rising magnetic flux tubes in stratified rotating spherical shells.

Such simulations are limited to an unrealistic parameter space, therefore, a scaling relation is required to scale the results to realistic physical regimes. We extended earlier works on 2D scaling relations and derived a general scaling law valid for both 2D and 3D. We then carried out two large series of numerical experiments and verified that the scaling law we have derived indeed applies to the fully non-linear case. It allowed us to extract a constraint for the rise time of magnetic flux tubes that is valid for any solar-like star. We finally introduced this constraint to a delayed dynamo model.

By carrying out simulations of a mean-field, delayed, *flux tube/Babcock-Leighton* dynamo, we were able to identify a new dynamo regime resulting from the delay. This regime requires delays about an entire cycle and exhibits subequipartition magnetic activity. Revealing this new regime shows that even for long delays the *flux tube/Babcock-Leighton* dynamo can still deliver non-decaying solutions and remains a good candidate for a wide range of solar-like stars.

Contents

List of Figures

List of Tables

1 Introduction

1.1 Context and motivation

Magnetic fields are everywhere, from the atomic level up to cosmological scales. At most of these levels magnetic fields play a significant role. The present work focuses on stellar magnetic fields. Understanding the influence of the magnetic fields on the evolution and dynamics of stars is crucial to build a unified picture of the large variety of stars found in our Galaxy. By analogy it is crucial to the understanding of our own star: the Sun.

The Sun, like most of the stars, has a magnetic field. Nowadays we observe a great level of detail of the solar atmosphere, from the solar surface at the photosphere up to the higher levels in the corona. At each of these heights magnetic fields play a major role: from the smallest scales of convection to the large-scale coronal field a rich variety of events may occur, all related to the solar magnetic field.

Understanding the complexity of the solar magnetic field will impact our everyday life. Nowadays, communication protocols and GPS are both key ingredients in the well-functioning of our society. Both are strongly influenced by the solar magnetic field: geo-efficient storms might perturb the on-board instruments of GPS and telecommunication satellites. Unraveling the mystery of the origins of solar eruptions could, some day, allow mankind to predict such extraordinary events. A first step toward prediction is the understanding of stellar magnetic activity.

Solar and stellar physicists still disagree on how solar-like stars maintain their own magnetic field. A simple computation of the magnetic diffusion time scale predicts that the large-scale solar magnetic field should diffuse within roughly a hundred years; but as we observe after almost 5 billion years the Sun still exhibit a strong and vigorous magnetic field. The present work is motivated by the following question: *why do the Sun and its solar-like peers still have a magnetic field?*

From the beginning of the last century, when the first observations of magnetic fields on the solar surface became possible, this question has been addressed. A possible mechanism to explain the maintenance of magnetic fields in stars is the *dynamo mechanism*: Stars pump energy from their kinetic budget into their magnetic budget, a process that prevents the stellar magnetic field from decaying. It is

eventually the thermal energy (which drives convection and thereby differential rotation) which fuel the kinetic budget for the dynamo mechanism to operate. While such flows are known to drive dynamos, the location where the dynamo operates leads to several scenarios. One of these scenario, called *Babcock-Leighton dynamo* (Babcock 1961; Leighton 1964), supposes that magnetic flux continuously emerges at the surface and reconnects, fueling the large-scale dipolar field.

A question arises: where does this emerging flux come from? The widely used case of a *Babcock-Leighton dynamo* based on *magnetic flux tubes* suggests that coherent magnetic structures – called *magnetic flux tubes* – form in the deep interior of the Sun. Such magnetic structures rise buoyantly toward the surface, transporting magnetic flux from the interior to the surface of the star, where the magnetic flux is diffused and transported as to regenerate the polar magnetic field. The present work aims to further investigate *the dynamics of the rise of magnetic flux tubes in solar-like stars.*

1.2 The specific case of solar-like stars

In the Milky Way, we observe a large variety of stars. Stars can be defined as a stratified sphere of highly ionized gas in mechanical and thermal equilibrium that is sufficiently massive to trigger fusion processes. This definition is common to all stars, but still allows them to differ in size, mass, luminosity, internal structure and metallicity. In the present work we focus on low-mass stars with masses from 0.3 to 1.2 solar masses, and particularly on solar-like stars.

All stars form from the collapse of an interstellar cloud. The collapse of the cloud forms a stellar object that ultimately reaches an equilibrium. The equilibrium is achieved when the gravitational energy liberated by contraction represents only a small portion of the total luminosity: the star stops collapsing and its center heats sufficiently to ignite hydrogen fusion. The star has reached the zero-age-main-sequence (ZAMS).

When hydrogen fusion is triggered, the star starts to consume the hydrogen in its core and produces helium. That process produces a large amount of energy, which has to be transported to the surface. In the deep interior opacity is sufficiently low to allow efficient energy transport by radiation. The stellar interior becomes radiative up to a certain radius. As temperature decreases toward the surface, opacity increases and radiation inevitably fails to transport the total energy further up. At this radius a more efficient process takes over: convection. Stars in the above-mentioned mass range always possess a radiative interior and a convective envelope, and (during the main-sequence) the thickness of the convective envelope

depends on the stellar mass and metallicity.

Stars leave the main-sequence when the hydrogen in their core is fully consumed, the resulting helium-rich core contracts and the star starts burning the hydrogen surrounding the core. This shell heats the light convective envelope that drastically expands, and the star becomes a red giant.

Along the main-sequence, solar-like stars remain relatively the same: their radius, luminosity, and mass remain of the same order of magnitude. The only property that significantly changes is rotation. Stars with an external convective envelope are magnetically active, magnetic fields together with stellar winds allow them to lose very efficiently their angular momentum: as the star gets older, it rotates more slowly (Schatzman 1962; Kraft 1967; Skumanich 1972).

On the contrary to solid objects, the pole of a star does not necessarily rotate with the same angular velocity as its equator: stars rotate differentially. Differential rotation is observed at the surface, but also inside stars, thanks to helioseismology and astero-seismology (Brown et al. 1989). Theoretically, the non-symmetric Reynolds stress, which naturally arises from a convective stratified plasma in rotation, may be responsible for differential rotation (Rüdiger 1989).

In the Sun we know from helioseismology that the radiative zone rotates approximatively uniformly, and that the convective zone has a significant rotation gradient in latitude: the pole rotates 25% slower than the equator (Howe 2009). In addition, the strong radial differential rotation gradient at the interface between the convective and the radiative zone produces shear. This region is called the *tachocline*. Even though there are still no clear observations of a tachocline in other stars than the Sun, by analogy, we suppose that all solar-like stars possess a tachocline.

To conclude, we define solar-like stars as any stellar object with a similar mass as the Sun. On the main-sequence those stars burn the hydrogen present in their core; their radius, luminosity and mass remain of the same order of magnitudes, over large time scales; they possess a differentially rotating convective envelope, which spans about one third of their radius; and they present a tachocline at the interface between their convective and radiative zone. With age solar-like stars decelerate: young solar-like stars rotate within a few days, while older types rotate up to 40 days (Skumanich 1972; Meibom et al. 2015; Barnes et al. 2016).

1.3 What do we know about stellar activity?

Mankind has been observing the details of the solar surface for at least four centuries. Such a large and detailed data sample is unique and allows us to study the large variety of events occurring on the solar surface.

Observations revealed the occurrence of evanescent dark spots on the solar disk. This discovery dissolved the ideal picture of a uniform and quiet Sun, and introduced the idea that our star is a highly dynamical body. The number of these spots on the solar disk varies from none to about a hundred. Their numbers oscillate with a period of 11 years (on average), we call this period the *activity cycle*. The solar activity cycle is illustrated in Fig. 1.1. This diagram shows every single spot at its latitude over almost 200 years. At the beginning of the cycle, spots appear at high latitudes centered about 30°; and as the cycle goes on, spots appear more often at lower latitudes. Because of the wing-shaped pattern, this plot is called the butterfly diagram.

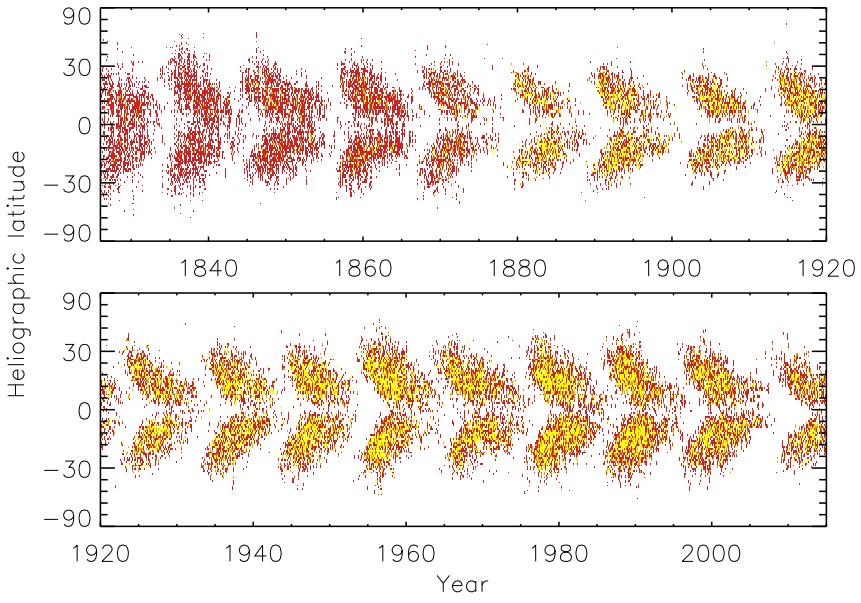

Figure 1.1: The solar butterfly diagram produced by V. Senthamizh Pavai. The colors indicate the number of active regions observed within a one degree bin over one day. Some of the data are taken from Arlt et al. (2013); Diercke et al. (2015), and D. Hathaway (NASA/MSFC website).

It is only since the last century, thanks to the work of Zeeman (1897) and Hale (1908), that scientists recognized the magnetic nature of sunspots. The Zeeman effect predicts that sunspots absorption lines split when they pass through a magnetized medium. The strength of the magnetic flux density determines the separation of the split. Sunspots are regions where the magnetic flux density reaches several kilogauss (kG). There, the magnetic field is strong enough for the plasma to follow the well organized magnetic lines. The turbulent motions of granulation are smoothed and the amount of energy transported by turbulence reduces. As a result, the spot looks darker than its surroundings.

Thanks to the improvement of instruments and analysis methods, we have access

to more details of the structures of spots: they are magnetically dominated regions, where magnetic flux emerges and forms a variety of patterns. Active regions typically appear as a pair of spots or more complex events with several concentrated or fragmented spots. The size of these regions varies from 10^6 – 10^7 meters (1 to 10 Mm), they contain magnetic flux which varies between 10^{20} Mx and 10^{22} Mx for typical active regions, up to 10^{24} Mx for the largest observed ones (Harvey & Zwaan 1993).

Independently of their morphology, active regions are typically bipolar, consisting of a leading spot (in the direction of rotation) which exhibits a given polarity and a following spot with an inverse polarity. Hale et al. (1919) identified that leading spots on the solar northern hemisphere have all the opposite polarity than the ones in the southern hemisphere (Hale's law). The polarity of an hemisphere reverses from one activity cycle to another. This polarity cycle is called the *magnetic cycle* and lasts for 22 years (on average).

A further remarkable characteristic of active regions is the relative position of the spots. The line linking the centers of the spots forms an angle with the equator, called the *tilt angle*. On average, the leading spot emerges closer to the equator than the following spot. There exist several statistical studies on tilt angles (e.g. Hale et al. 1919; Howard 1991, 1993; Baranyi 2015), it has been shown that the average tilt angle over a cycle is not zero but between 5 to 7 degrees (e.g. Dasi-Espuig et al. 2010; McClintock & Norton 2013; Wang et al. 2015; Senthamizh Pavai et al. 2016). A further relevant result is the latitudinal dependence of the tilt angle, also called *Joy's law*: active regions emerging at lower latitude statistically exhibit lower tilt.

The tilt is not the only characteristic that varies with latitude: the proper motion of active regions also has a latitudinal dependence. They follow closely the solar surface differential rotation – spots are used for measuring solar and stellar differential rotation –, but not exactly. This small difference suggests that their proper motion may follow deeper rooted flows. This observational fact supports a scenario where active regions form due to the emergence of a *magnetic flux tube* that originates from the convective zone.

The Sun is not the only active star in the Galaxy: a large fraction of stars emit X-rays. The precise mechanism responsible for the X-ray emission remains unclear, but it is accepted that the ratio of X-rays luminosity over the bolometric luminosity is proportional to the large-scale magnetic field and is therefore a good proxy for stellar magnetic activity (Jakimiec et al. 1986; Preminger et al. 2010). Large data set of stars showing X-ray emissions are now available (Wright et al. 2013), some even show magnetic cycles (Wilson 1978; Oláh & Kolláth 1999; Strassmeier 2009).

By the distance that separates us from stars, there are no direct observations of

magnetic structures on stellar surface. Indirect observations become possible. The (Zeeman) Doppler Imaging offers the great opportunity to reconstruct temperature (and even magnetic) maps of stellar surfaces (Vogt 1981; Semel 1989; Strassmeier 2009). The level of details is naturally low compared to the solar case, but we are now able to identify evolution and migration of active regions, as well as magnetic cycles (Vidotto et al. 2014; Waite et al. 2015; Folsom et al. 2016; Mengel et al. 2016; Hackman et al. 2016).

1.4 Maintaining the stellar magnetic fields: the Babcock-Leighton dynamo

Given the low molecular viscosity inside the Sun of about 10^4 cm^2/s (Spitzer 1962), the convective envelopes of solar-like stars are expected to be highly turbulent. Turbulence is a very efficient mixing process that enhances the magnetic diffusivity of the system. The turbulent magnetic diffusivity at the surface of the Sun (η_t) is expected to be about $10^{12}\,\mathrm{cm^2\,s^{-1}}$, but this value maybe lower in the convective envelope where the flows are less turbulent. Without a process acting against the turbulent magnetic diffusion, the solar magnetic field would diffuse within a time scale $\tau_{\mathrm{diff}} = R_\star^2/\eta_t \approx 150\,\mathrm{yr}$. This process is called the *dynamo* (Rädler et al. 2003; Charbonneau 2010).

Before explaining the concept of dynamo, we need to introduce some general aspects of stellar magnetic fields. Magnetic fields are divergence-free or *solenoidal*, that is, they have no source or sink points. This particular aspect allows us to describe any three dimensional magnetic configuration with only two components: the *poloidal* and the *toroidal* components. In Fig. 1.2 we illustrate the geometry of the poloidal and toroidal components of a hypothetical axisymmetric magnetic dipole. In that case, the toroidal component points in the azimuthal direction and changes sign across the equator. The poloidal field is the one dominating the observable surface fields and defines – with its large-scale average – the magnetic poles of the configuration.

Considering the magnetic cycle of the Sun, and its most famous representation – the butterfly diagram, cf. Fig. 1.3 – one can notice the alternation of toroidal and poloidal components. At the maximum of the cycle, most of the flux emerges at low latitude under the form of active regions, the east-west orientation of active regions suggests that the field was mostly toroidal before. The toroidal component of the large-scale magnetic field is at maximum, and the poloidal component at minimum. At the minimum of the activity cycle, most of the surface flux concentrates at the

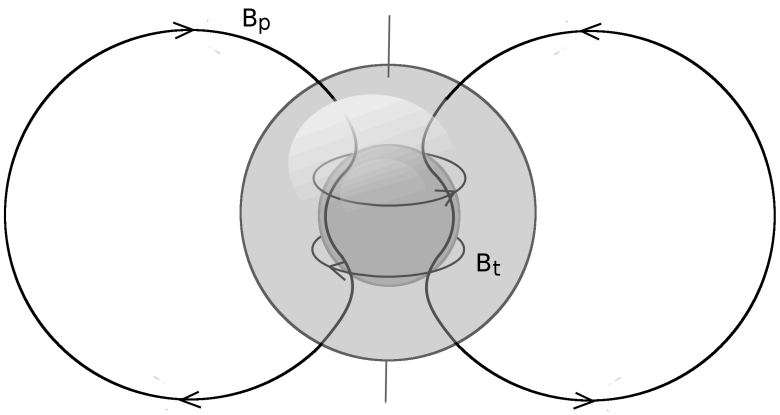

Figure 1.2: Illustration of the geometry of the poloidal ($B_{\rm p}$) and the toroidal ($B_{\rm t}$) components of an arbitrary large-scale dipolar magnetic field. The transparent grey sphere represents the surface of a solar-like star; the solid grey sphere the radiative interior. The black solid lines represent the toroidal and poloidal components of an hypothetical large-scale dipolar field. The arrows show the direction of the field. The rotation axis of the star is shown by the thin vertical axis crossing the star.

pole mostly following the poloidal component: the poloidal component of the large-scale magnetic field is at maximum, the toroidal component at minimum. We face a non-decaying oscillatory system. Such a system requires a mechanism that generates poloidal magnetic fields from toroidal ones, and vice versa.

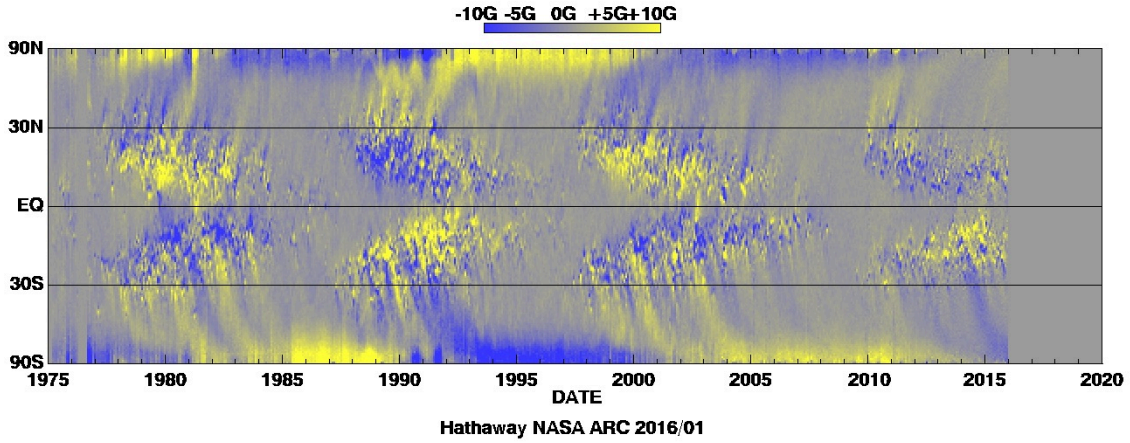

Figure 1.3: The magnetic butterfly diagram. In contrast to the standard butterfly diagram, here the polarity information is also indicated. The yellow color indicates a positive polarity where the blue indicates a negative polarity. Credit: D. Hathaway, NASA.

Because of the nature of solar-like stars, it is commonly accepted that the dominating process responsible for the generation of toroidal component from the poloidal component is differential rotation. In the Sun the large shear that occurs at the bottom of the convective zone may wind up the large-scale poloidal magnetic field

around the radiative interior. It concentrates and forms strong bundles of toroidal magnetic flux at the bottom of the convection zone, this effect is called the Ω-*effect*.

In contrast to the Ω-*effect*, the location where the poloidal field is generated is still under debate. This situation leads the solar community to suggest several processes that may apply to the Sun.

One of these processes, the *turbulent dynamo* supposes that the turbulent motions in the convective zone are responsible for the regeneration of the poloidal field: the unorganized convective flow twists the magnetic field lines at small scales, the field reconnects at larger scale and regenerates the large-scale poloidal field. The presence of helical turbulent velocity field produces a mean-field source term in the induction equation, called the *turbulent* α-*effect* (Steenbeck & Krause 1966; Brun et al. 2004; Käpylä et al. 2010, 2012; Brown et al. 2010; Racine et al. 2011).

When both the Ω-*effect* and the α-*effect* operate the magnetic energy grows until it clears out the kinetic budget. This situation is unrealistic therefore a non-linear limiting mechanism is required. Several limiting mechanism have been suggested; one particularly accepted, the *turbulent quenching*, assumes that highly magnetized plasma are less turbulent than poorly magnetized plasma. In such a situation, the net-effect of the turbulent electromotive force diminishes as it amplifies magnetic field. This mechanism frames the solution to finite amplitudes. However, for highly turbulent medium, this type of quenching may become catastrophic and leads to decaying solutions.

In order to avoid catastrophic quenching, it has been suggested that the source terms of the poloidal and toroidal field operate at two different locations (Parker 1993). Such dynamos are called *interface dynamos*.

The *Babcock-Leighton dynamo* is a particular case of an *interface dynamo*[1] In such a dynamo the Ω-*effect* operates at the tachocline. The resulting toroidal magnetic flux is transported to the surface, where it forms active regions which exhibit tilt angles. At the surface, the magnetic flux of the active region diffuses and advects toward the pole under the action of the random walk of granulation and the meridional circulation. Reaching the pole the remnant magnetic field reconnects with the large-scale dipolar field. This mechanism is called the *Babcock-Leighton mechanism*. Formulating this effect as a source term in the induction equation leads to a system capable of driving a dynamo.

In contrast to other dynamos, *Babcock-Leighton dynamos* require the presence of active regions to operate, while turbulent dynamos, for instance, suggest that active

[1]Interface dynamos supposes that the source of poloidal field and the source of toroidal field operate at two different locations. But it is possible to build a Babcock-Leighton dynamo where the source term of toroidal field is not the Ω-effect but the shear at the sub-surface shear layer. Such a dynamo is an exception and is not an interface dynamo.

regions are a manifestation of the dynamo mechanism.

All *interface dynamos* require a mechanism to transport magnetic flux from one location to the other. The most used case of Babcock-Leighton dynamos is the one where magnetic flux tubes are responsible for the transport of the magnetic flux from the bottom to the top of the convective zone; and where meridional circulation and turbulent pumping are responsible for the transport of flux from the poles to the tachocline. The toroidal field is amplified and stored at the tachocline until instabilities form magnetic flux tubes. The latter rise buoyantly, transporting the toroidal magnetic flux up to the surface, where the *Babcock-Leighton mechanism* operates and eventually leads to a reversal of the large-scale polar field.

The present study addresses the dynamical rise of magnetic flux tubes in the frame of a Babcock-Leighton dynamo.

1.5 The magnetic flux tube scenario

1.5.1 The concept: E. Parker (1955)

The concept of magnetic flux tubes was introduced by Parker (1955). The author discussed the possible buoyant non-equilibrium of closed magnetic structures in an adiabatically stratified background, such as a convective envelope. Due to its magnetic nature, a magnetic flux tube in mechanical and thermal equilibrium with its surroundings will always lack density and buoyantly rise in the opposite direction of gravity. Parker suggested that these magnetic structures may transport magnetic flux from the stellar interior to the surface.

1.5.2 The thin flux tube era: from Spruit (1981) to Weber (2011)

This original idea of Parker found a crucial realization, when Spruit in 1981 (Spruit 1981) derived the equation of motion of a thin magnetic flux tube. This approximation reposes on the idea that magnetic flux tubes are thin compared to the length scale (the pressure scale height) of their surroundings. Under such an approximation the internal thermal and magnetic properties of magnetic flux tubes remain constant across the flux tube diameter. Inside the Sun, this approximation holds from the bottom of the convective zone up to the last ten megameters (Mm).

The discreet description of the internal properties of magnetic flux tubes allows to solve a simple set of equations. Solving this set of equations is computationally inexpensive and permits large parameter studies.

The first remarkable result of the thin flux tube approximation was to obtain an order of magnitude for the initial magnetic flux density of solar magnetic flux tubes at the bottom of the convective zone. Supposing that emerging magnetic flux tubes form active regions, the equatorial migration requires that they emerge at high latitudes in the beginning of the cycle ($\approx 30°$) and at lower latitudes by the end of the cycle ($\approx 10°$). In axisymmetric simulations, flux tubes with magnetic fields of at least 10^5 G were necessary to emerge at such low latitude. (Choudhuri & Gilman 1987; Choudhuri 1989; Fan et al. 1994; Schüssler et al. 1994). The latitudinal migration observed in Fig. 1.1 is believed to be the result of the migrating toroidal field at the base of the convective zone.

These results were encouraging but also surprising in many aspects. Magnetic flux tubes with an initial magnetic flux density larger than 60 kG are in super-equipartition with the convective motions: the magnetic energy density of the flux tube is larger than the kinetic energy density of convection. The existence of super-equipartition fields is still debated.

The major issue of the flux tube scenario, however, is how to store magnetic flux at the bottom of the convective zone. Several authors (van Ballegooijen 1982; Schüssler 1983; Moreno-Insertis et al. 1992; Rempel 2004) suggested that a magnetic flux layer can be stable in a sub-adiabatically stratified background. In the solar case, this is just below the convective zone near the *tachocline*. In such an environment, magnetic layers may store magnetic flux on a sufficiently long time scale to form super-equipartition magnetic flux tubes (Rempel et al. 2000).

Several processes have been suggested that may lead to the formation of magnetic flux tubes. The present work is based on one possible scenario: the magnetic flux is stored at the tachocline in the form of a magnetic layer; due to the amplification of the toroidal magnetic flux by differential rotation, the magnetic layer may become unstable similarly to a Rayleigh-Taylor type of instability (Wissink et al. 2000; Fan 2001) and form tubular magnetic structures. These structures enter the convective zone and become buoyantly unstable, they rise on a short time scale and emerge at the surface forming active regions.

1.5.3 On the limits of the thin flux tube approximation

The thin flux tube approximation ignores dynamical effects such as the self fragmentation of magnetic flux tubes under the viscous force arising from their own rising velocity (Schüssler 1979). Such fragmentation may reduce the buoyancy of the remnants and prevent them from reaching the surface. This issue can be tackled by adding a poloidal component to the magnetic flux tube called *twist*. For suffi-

ciently twisted magnetic field lines, the radial magnetic tension (resulting from the azimuthal field) suppresses the generation of vortices and ensures that the magnetic flux tube remains coherent (Emonet & Moreno-Insertis 1998; Fan et al. 1998; Dorch et al. 1999).

However introducing a twist further constrains the formation of magnetic flux tubes (Jouve et al. 2012). This issue still needs to be explored, especially because a rather large twist is required; which may trigger the kink instability.

The question of *how much twist is required* remains open, mostly because viscosity – which controls the fragmentation – has a lower limit in simulations due to their resolution. Modern simulations still fail to reach the molecular viscosity of the solar plasma.

1.5.4 From axisymmetric to non-axisymmetric rise

The fact that the thin flux tube approximation does not require much computation time allowed early on to extend the study of magnetic flux tubes to the non-axisymmetric case. While rising, a non-axisymmetric thin flux tube naturally tilts under the action of rotation. The resulting active regions have a tilt angle that depends on latitude.

Simulations of thin flux tubes also permit statistical studies. Weber et al. (2011) simulated the rise of thin magnetic flux tubes in a turbulent convective environment. Turbulence brings randomness; by carrying out a large amount of simulations, they could extract relevant statistics for the tilt angle: they concluded that magnetic flux tubes of 40–50 kG reproduce Joy's law.

As already mentioned, the thin flux tube model does not account for the required twist, and the latter may impact the final tilt angle of active regions. Jouve et al. (2013) studied thick flux tubes in a convective environment under the anelastic approximation. The latter consists in filtering sound waves to increase the numerical time step. This approximation is valid in almost the full solar convective zone where convective motions are much smaller than the sound speed. The authors indeed found that the tilt angle depends on both the twist and latitude.

Fan (2008) further contributed to the anelastic non-axisymmetric rise of thick flux tubes by finding that non-axisymmetric thick magnetic flux tubes rise radially, in contrast to their axisymmetric counterparts, which are latitudinally deflected under the action of rotation.

1.5.5 Toward a compressible non-axisymmetric study

Both, the thin flux tube approximation and the anelastic approximation may miss some dynamical effects, that only fully compressible simulations could reveal. The first study on the compressible rise of magnetic flux tubes was carried out by Cheung et al. (2006). The authors studied the limits of the thin flux tube approximation. This study was limited by its Cartesian geometry, the two dimensional domain, and the absence of rotation. The present work aims to combine compressibility with the non-axisymmetric rise of a magnetic flux tube in an adiabatically stratified rotating spherical shell.

2 Description of the numerical setup

2.1 Introduction

A few theories aim to explain how low-mass stars maintain their magnetic fields; they are known as dynamo theories. One ensemble of these theories, the *flux transport dynamos*, suggests that the mechanism responsible for the generation of toroidal fields (Ω-effect) and the mechanism that regenerates the poloidal field (Babcock-Leighton mechanism) operate at two different places. In such dynamos the magnetic flux needs to be transported from one place to another. The particular case of the *flux tube/Babcock-Leighton dynamo* suggests that coherent magnetic structures, called *magnetic flux tubes*, form at the place where the toroidal field is generated, buoyantly rise through the convective zone transporting the magnetic flux to the surface, where the Babcock-Leighton mechanism leads to a net transport of poloidal field to the poles. The Sun, and numerous other stellar objects, exhibit cyclic magnetic activity (Saar 2002; Kővári & Oláh 2014). The idea behind any cyclic dynamo mechanism is that the large scale magnetic field alternates between a poloidal and a toroidal topology. It has been shown that there exists non-decaying oscillatory solution of the dynamo equation (induction equation with a non-linear source-term). These solutions could be a good description of stellar cycles.

In the considered scenario, when magnetic flux tubes emerges at the stellar surface, they form magnetic active regions. The magnetic flux that emerges in active regions may partially cancels with the magnetic flux of active regions from the other hemisphere. The remaining flux is advected by the meridional circulation toward the poles. On the way the flux decays and fragments under the action of the random walk of granulation. Finally when it reaches the poles the emerged flux reconnects with the large-scale dipolar field. This entire process taking place at the surface is called the *Babcock-Leighton mechanism*, it is responsible for the reversal of the large scale polar field (Babcock 1961).

In the second phase of the dynamo mechanism, meridional circulation and turbulent pumping transport the poloidal field to the bottom of the convection zone,

where the shear layer, called the *tachocline* (Miesch 2005, sect. 3.2), winds up the large scale poloidal field and generates a layer of toroidal magnetic field deep in the stellar interiors. These regions form magnetic flux tubes and a new cycle starts.

In the present work, we aim to find a universal relation between the rise time of magnetic flux tubes and the stellar parameters. We plan to extract such a relation from direct numerical simulations (DNS) of rising magnetic flux tubes. This relation can be introduced into a mean-field formulation of the Babcock-Leighton dynamo where it acts as a delay, i.e. as a non-linearity whose impact on the dynamo solutions may be manifold.

In the present Chapter, we introduce the concept of the simulations, discuss its implications on the numerical setup and numerical treatments, and underline the limits that such a numerical treatment imposes. Finally, we detail the environment in which we introduce magnetic flux tubes.

2.2 The journey of a deeply rooted buoyant flux tube toward the surface

In this Section, we draw the various phases of the journey of a magnetic flux tube toward the surface: generation, rise and emergence. We justify our choice to focus on the rising phase.

The journey of a magnetic flux tube starts with its generation. Several processes can generate magnetic flux tubes. Helioseismology suggests that the convective bulk of the sun rotates differentially, whereas the radiative interior seems to rotate in a uniform manner. The resulting radial gradient of rotation at the interface produces a shear layer. Here we consider that shear flows at the tachocline build toroidal magnetic layers which concentrate into magnetic flux tubes thanks to an instability. That instability has been discussed by Matthews et al. (1995, and references therein) and several others (Rempel et al. 2000; Wissink et al. 2000; Fan 2001; Gilman & Rempel 2005; Favier et al. 2012; Jouve et al. 2012).

Since the mean-field formulation of the Babcock-Leighton dynamo only requires the rise time of magnetic flux tubes, we exclusively study the rise of magnetic flux tube and exclude the destabilization phase to save computation time. Therefore, we initially consider the magnetic flux tube to be well formed and already in non-equilibrium (like in Fan 2008; Jouve & Brun 2009). We discuss this aspect in detail in Chaps. 4 and 5.

The well-formed twisted magnetic flux tube buoyantly rises through the convective envelope. It can take several paths, it tilts and writhes, and it can even become

unstable against the kink instability, depending on the stellar rotation, its initial twist and its buoyancy (see Chap. 1). Moreover, both convection and differential rotation will impact the dynamics of the rise, they may deform and deflect weak magnetic flux tubes (less than 10 kG in the solar case) (Fan 2008; Jouve & Brun 2009; Weber et al. 2011). That is why we refrain from comparing our results with detailed surface observations (e.g. spot emergence, morphology of spots, tilt angles, spots decay) but we address more general aspects like the rise time, the balance between the various forces controlling the rise of magnetic flux tubes, and universal relations that can apply on a large variety of stars; the goal of this work is to enrich our understanding of the buoyant rise of magnetic structures in rotating stratified interiors.

Eventually the flux tube emerges at the surface and forms active regions that exhibit complex morphologies, asymmetries, and tilt (Caligari et al. 1995, 1996; Moreno-Insertis et al. 1994; Abbett et al. 2001; Jouve et al. 2013). As for the destabilization phase, we exclude the emergence phase of our study and focus exclusively on the rise. Along with this Chapter we will show that emergence is a subtle issue and has to be addressed separately.

2.3 On the need of compressible MHD

We want to design a versatile numerical setup that is capable of evolving to further applications. The present study focuses on solar-like stars: stellar objects of about a solar mass on the main-sequence, possessing a convective envelope spanning about one third of their radius; but the numerical setup should apply to a large range of stellar objects. In Fig. 2.1 we highlight the various stellar types we plan to study in the future: from ZAMS solar-like stars to red giants. These stellar objects share a few aspects: they all have a convective envelope of very different thicknesses, shear flows, and exhibit cyclic magnetic activity; that makes them appropriate candidates for the presence of magnetic flux tubes (Granzer 2004).

Because in solar-like stars the sound speed is high compared to rotation and convective velocities (convective and rotation Mach numbers are both about 10^{-3} within the bulk of the convective zone), and the convective envelope is nearly adiabatic, the anelastic approximation is well justified. But for other types of stars like red giants, the higher Mach number of convective flows (≈ 1) leaves the domain of validity of this approximation, and compressibility has to be considered.

In Fig. 2.2, we show another advantage of compressibility: it allows to study highly subadiabatic regions, such as radiative zones. The anelastic approximation limits the studies to weakly subadiabatic interiors, like the overshoot layer (Jones

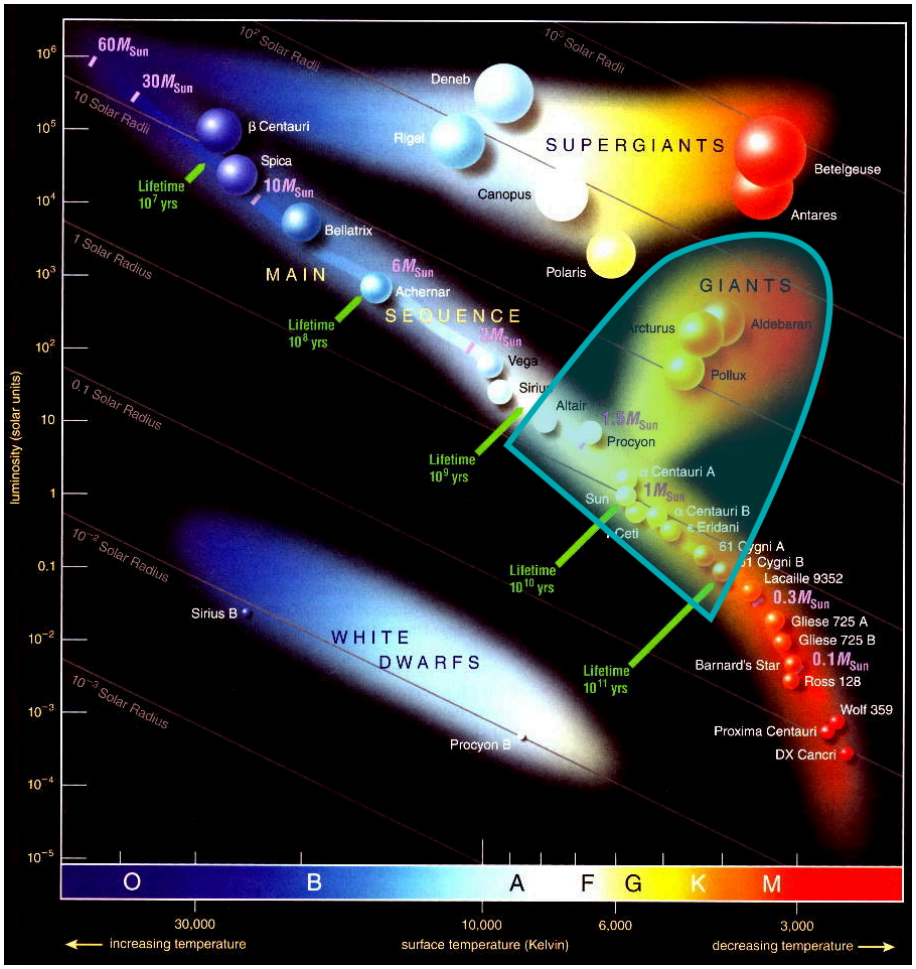

Figure 2.1: Stars of interest in the Hertzsprung-Russell diagram. The cyan area contains main sequence A,F,G and K stars, which have an external convective envelope and supposedly a tachocline. This region also contains giant stars as they also possess an external convective envelope and possibly a tachocline. Adapted from ESO (CC-BY).

et al. 2011; Lantz & Fan 1999). The interaction between the convective zone and the radiative zone can only be studied with compressible MHD. Such a study would help to constrain the role of a tachocline and/or the role of the overshoot region to build magnetic flux tubes.

Simulating stellar surface is a difficult issue. Compressibility should provide an advantage compared to the anelastic approach. Indeed, the Mach numbers of the convective flows occurring at the surface ($\approx 10^{-2}$) are large compared to the ones of the flows at the bottom of the convective zone ($\approx 10^{-7}$). Such large Mach numbers place the anelastic treatment close to the limits of its domain of validity. This is not the case for a compressible treatment, which theoretically should allow us to simulate from the radiative zone up to the photosphere. However, at the surface the numerical resolution becomes a limiter: it fails to catch the stiff stratification, and the small scales of motion. Without a properly simulated surface, we exclude

emergence events from our study. In general, such studies are still limited to local simulations.

Solving the fully compressible MHD set of equations also offers the opportunity to study sound waves. One may apply helioseismologic methods on the self-consistent sound waves obtained from our simulations and try to constrain the helioseismic methods in the presence of a magnetic field.

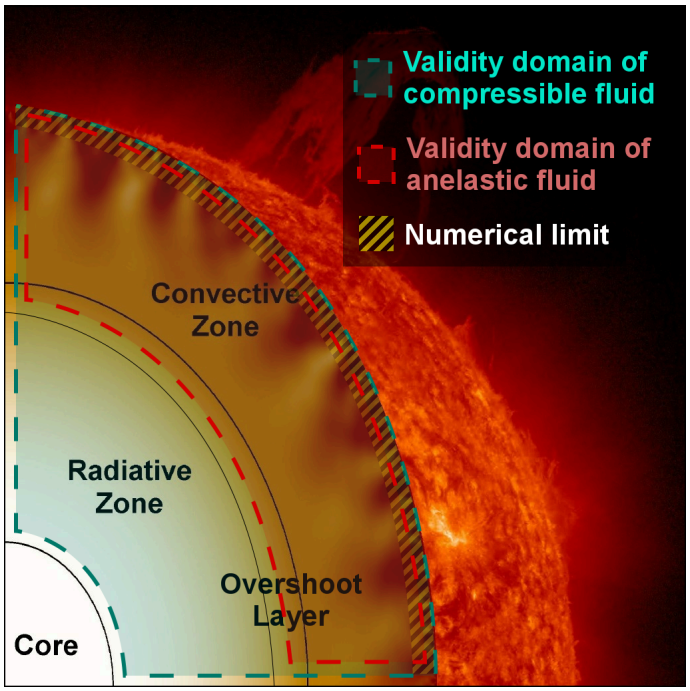

Figure 2.2: Overview of the standard stellar structure of a solar-like star overlayed with the domains of validity for compressible and anelastic simulations. The blue domain represents the compressible validity domain extending from the surface to the deep radiative zone. The anelastic validity domain (in red) extends only from close to the surface to the overshoot layer. The hatched area represents the region where global simulations usually fail to resolve the strong stratification (very) near the surface.

Finally, this work is the first specific study on compressible flux tubes in a 3D spherical shell. A compressible study of rising flux tubes has been carried out by Cheung et al. (2006) (see Fig. 2.3), where the authors studied the 2D rise of a magnetic flux tube in a Cartesian plane and explored the limits of the thin flux tube approximation. Here we go further and verify the agreement between anelastic and compressible simulations; and the effects of both, rotation and spherical geometry, in axisymmetric and non-axisymmetric setups.

These aspects motivated our choice of a compressible interior. We use the parallelized NIRVANA code (see Ziegler 2011) [1] to solve the fully compressible MHD set

[1] http://www.aip.de/Members/uziegler/nirvana-code

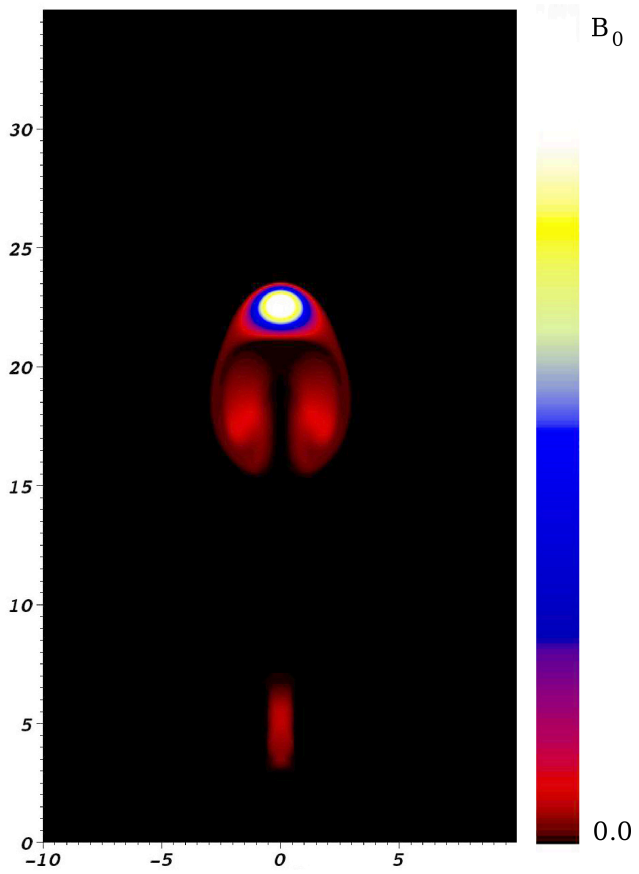

Figure 2.3: Compressible buoyant flux tube in a Cartesian stratified box. The colors represent the magnetic field perpendicular to the plane. Computed after the setup from Cheung et al. (2006).

of equations on a spherical grid:

$$\partial_t \rho + \nabla \cdot (\rho \mathbf{v}) = 0 \quad , \tag{2.1}$$

$$\partial_t (\rho \mathbf{v}) + \nabla \cdot \left[\rho \mathbf{u}\mathbf{u} + p_{\rm tot}\mathbf{I} - \frac{1}{\mu_0}\mathbf{B}\mathbf{B} \right] = \rho \mathbf{g} + \rho \mathbf{f} \tag{2.2}$$

$$\partial_t e + \nabla \cdot \left[(e + p_{\rm tot})\mathbf{v} - \frac{1}{\mu_0}(\mathbf{v}\cdot\mathbf{B})\mathbf{B} \right] = \nabla \cdot \left[\frac{\eta}{\mu_0}\mathbf{B} \times (\nabla \times \mathbf{B}) - \mathbf{F}_{\rm rad} \right] + \rho \mathbf{g}\cdot\mathbf{v} + \rho \mathbf{f}\cdot\mathbf{v} \quad , \tag{2.3}$$

$$\partial_t \mathbf{B} - \nabla \times (\mathbf{v} \times \mathbf{B}) - \eta \nabla^2 (\mathbf{B}) = 0 \quad , \tag{2.4}$$

$$p = \frac{\rho k_{\rm B} T}{m\mu} \quad , \tag{2.5}$$

where, $\mathbf{v}$, $p_{\rm tot}$, $\mathbf{B}$, $\mathbf{g}$, $\mathbf{f}$, T, $\mathbf{F}_{\rm rad}$, $k_{\rm B}$, m and μ are the velocity field, the total pressure being the sum of the thermal (p) and the magnetic pressure ($p_{\rm m} = B^2/2\mu_0$), magnetic flux density, gravitational acceleration, external acceleration [2], the tem-

[2]For the present experiment, we consider only the Coriolis effect, as a result, the last term of the conservation of energy nullifies.

perature, the radiative flux, the Boltzmann constant, the atomic mass unit and the mean molecular weight, respectively. Apart from the usual symbols, $\partial_t(.)$ and $\mathbf{I}$ are the partial time derivative and the identity matrix, respectively. The spherical coordinate system is (r, θ, ϕ).

2.4 On the need of a global domain

As we already mentioned, rising magnetic flux tubes have complex behaviors: they can take a wide range of paths, from purely radial to almost parallel to the rotation axis (Choudhuri & Gilman 1987; Moreno-Insertis 1986; Moreno-Insertis et al. 1992; Schüssler & Solanki 1992). It is difficult to predict the size of the needed domain. Furthermore, to ensure that boundary conditions do not impact the rise of the magnetic flux tube, we prefer to use the largest possible domain.

We chose to simulate the rise of a magnetic flux tube in almost the full northern hemisphere from close to the pole down to the equator. The NIRVANA code would allow to include the pole but the pole is difficult to treat numerically since it is a singularity and the boundary conditions at the pole are computationally very expensive: they require numerous and complex communications between parallel CPU cores. To ensure that excluding the pole does not affect the results, we conducted two simulations with and without the pole. We obtained almost identical results, demonstrating that the pole does not play a major role in our setup.

Our global domain fails to reach the surface, however. The strong stratification at the surface is difficult to capture. We had to find a balance between the largest radial extent and a pragmatic resolution that is sufficient to resolve the top pressure scale height with at least ten points.

We chose a domain from 0.684 to 0.946 solar radii, and from 0 to $0.95\,\pi/2$ in latitude. The azimuthal extent depends on the needs of various non-axisymmetries (see more details in Chap. 5).

Finally, we plan our setup to be versatile: to address other stars and further developments, a global domain appears to be the best choice.

2.5 The power of adaptive mesh refinement (AMR)

The early studies of rising magnetic flux tubes were carried out under the thin flux tube approximation. This is justified because stellar evolution models tell us that the pressure scale height at the bottom of the convection zone is large compared to the

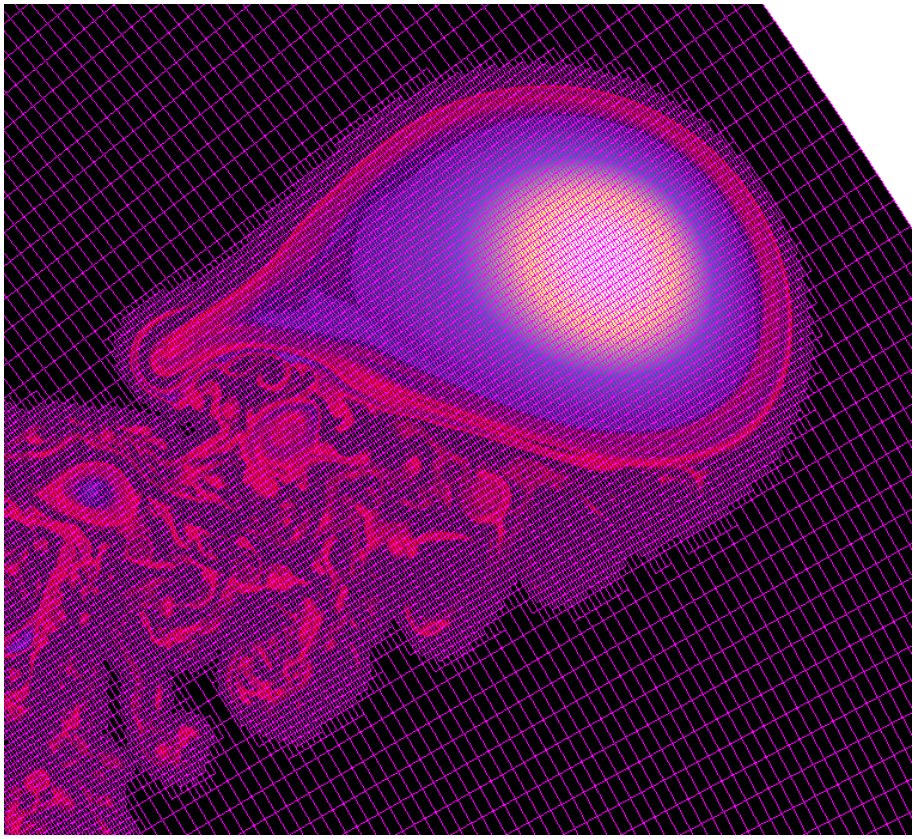

Figure 2.4: Mesh structure of an axisymmetric simulation. The colors represent the intensity of the azimuthal magnetic field normalized by the maximum. The purple grid represents the grid structure. Note that a single cell of this grid represents a block of the simulation. A block consists of 2×2 cells in 2D ($2 \times 2 \times 2$ in 3D).

hypothetical radius of a magnetic flux tube: the hydrodynamical characteristics of the flux tube do not vary much across its diameter. In the 'thick' flux tube approach, we do not approximate the small variations to constant values, nevertheless the magnetic flux tube remains small compared to the pressure scale height. The flux tubes we simulate have a radius of 10^{-3} $R_\star$ [3]; the flux tube is a tiny structure in the global domain.

In the solar interior, the molecular magnetic diffusion time scale for a flux tube is about 15000 yr , which is much longer than the rise time supposedly lasting about one month. Because of the small molecular magnetic diffusion, the tubes conserve their magnetic flux. To ensure conservation (more than 90% of the initial flux remain in the magnetic flux tube), we need to resolve the diameter of the magnetic flux tube with at least 10 grid points. Such a resolution, however, would lead to a global resolution of ≈ 2500 points in the radial direction. This can be achieved, for a single demonstrative simulation, but a large parameter study requires lower

[3] The values we give along this chapter stem from the axisymmetric setup. For more details about the corresponding non-axisymmetric values, please refer to Chap. 5.

resolutions.

The NIRVANA code offers a solution that uses adaptive mesh refinement (AMR). It consists in resolving the stellar interior with a base-resolution, sufficient to capture the stratification at the surface, and refining the base-grid wherever finer structures are interesting. We chose a base-resolution of 512 in the radial direction so that we resolve the top pressure scale height with a few points, and allow two levels of refinement to resolve the flux tube with about 15 points in diameter. The resulting effective resolution is about 2048 in radius. In Fig. 2.4 we show how AMR allows us to obtain fine complex structures.

Choosing the criterion that decides about refinement is not a trivial task. In our setup, we want to refine the magnetic flux tube. Choosing the presence of magnetic field as refinement criterion may sound sensible, but such a simple criterion leads to large refined regions, that increasing the required computational time. It is appropriate to consider the first and second derivative of the magnetic flux density to follow more finely the interesting regions.

We construct the following criterion:

$$\left[\xi_1 \frac{\|\delta B\|_2}{|B|} + (1-\xi_1)\frac{\|\delta^2 B\|_2}{\|\delta B\|_2 + 10^{-2}\cdot|B|}\right]\left(\frac{\delta x^{(l)}}{\delta x^{(0)}}\right)^{\xi_2}\begin{cases} > \mathcal{E}_B & \Rightarrow \text{refinement,} \\ < 0.8\mathcal{E}_B & \Rightarrow \text{derefinement,}\end{cases}$$

where $\|\delta B\|_2$ and $\|\delta^2 B\|_2$ are the 2-norm of the first and second differences of B, ξ_1 is a switch-parameter that controls the first or second derivative nature of the criterion, and ξ_2 is the level dependence parameter that controls refinement across the levels. $\mathcal{E}_B$ is the threshold of the relative gradient and $\delta x^{(0)}$ and $\delta x^{(l)}$ represent the grid size at the base level and at a level l, respectively. The values of ξ_1, ξ_2 and $\mathcal{E}_B$ are empirical. They are adapted to our specific problem such that the refinement follows closely the boundary of the magnetic flux tube. The boundary is defined as the contour that contains 98% of the total magnetic flux. A further constraint is that the flux tube should be uniformly refined. A unique level ensures a constant numerical diffusivity across the flux tube diameter.

The first term of the first factor represents the relative growth of magnetic flux density, the second term represents the curvature of the same quantity. The second factor scales the discretization of a given level with the base-level. When the criterion becomes larger than the threshold, the corresponding block is refined; when the criterion becomes less than 80% of the threshold, the block is coarsened.

In all setups, we used the same parameters: $\mathcal{E}_B = 5.10^{-3}$, $\xi_1 = 0.8$, and $\xi_2 = 1.2$. The choice of this set was obtained by testings.

2.6 The difficulties due to the compressible character of the setup

Compared to the thin flux tube approximation and the anelastic approach, compressibility is more realistic; however, it constrains the system and prevents us from integrating a few ingredients in the simulation. In this section, we justify our choice to limit the complexity of the background to a uniformly rotating, static environment.

2.6.1 Excluding a convective background

The choice of the stellar background is crucial, it needs to be addressed carefully. The main issue in simulating compressible rising flux tubes resides in the limitation on plasma-β ($= p/p_\mathrm{m}$). In the Sun, we expect this parameter to approach 10^5. Because both approaches, the thin flux tube approximation and the anelastic approach, consider only the difference in density between the flux tube and its surroundings, they have the great advantage of reaching this high β with a reasonable resolution.

The remarkable example of anelastic simulations from Jouve & Brun (2009) includes most of the relevant ingredients for a realistic description of rising magnetic flux tubes: turbulence is treated with the large-eddies approximation and differentially rotating convection with meridional circulation in a global simulation. In Fig. 2.5 we show a meridional section of one of their simulations, where a magnetic flux tube rises through a convective environment.

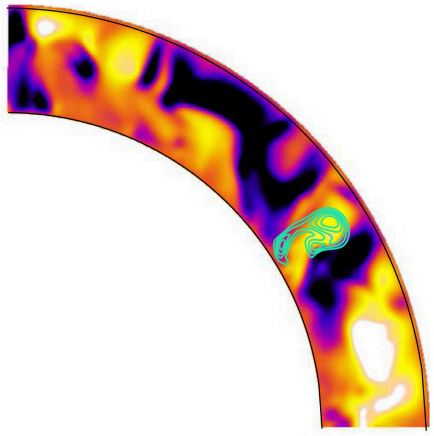

Figure 2.5: Anelastic rising flux tube in a rotating convective spherical shell. The black (yellow) color denote down (up) flows of about -300 m/s ($+200$ m/s), and the green contours are B_ϕ levels associated with the flux tube. Adapted from Jouve & Brun (2009).

In contrast to anelastic simulations, compressible simulations solve the mass conservation expressed in absolute density. The discretization error, inherent to any

numerical experiment, produces oscillations in the thermal pressure term. These oscillations are clearly unphysical and need to be considered as noise. In our setup, thanks to its high precision, these oscillations have an amplitude of 10^{-4} times the thermal pressure. However, a $\beta \approx 10^5$ would lead to a magnetic pressure signal of the order 10^{-5} times the thermal pressure, which is below the amplitude of the non-physical pressure oscillation. The setup would fail to resolve the magnetic flux tube, which will dissipate and never rise.

A solution to this problem would be to increase resolution. NIRVANA uses a second order scheme in time and space, and the solution converges in a quadratic manner in the asymptotic case. Hence, in a perfect situation, the amplitude of the (non-physical) pressure oscillations should reduce in the same manner as the discretization error. Resolving the flux tube such that the magnetic pressure signal were 100 times larger than the non-physical pressure oscillations, would require at least a resolution which is 2^{10} larger (or 10 additional levels of refinement) than the ones mentioned in Sect. 2.5. This would lead to an effective resolution of 2^{19} grid points in the radial direction. Such a resolution is clearly beyond the current computational capabilities.

Another solution consists in decreasing β. To ensure that the flux tube is sufficiently resolved, we constrain β to a maximum of 100 such that the numerical pressure oscillations never exceed 1% of the magnetic pressure signal. The decrease of β leads to some issues, however: the magnetic flux density of the tube becomes much larger than the one expected in the Sun. Such magnetic flux tube embedded in a convective environment will ignore any convective velocity. To solve this issue, one could argue that a stronger convection leads to a situation where both ingredients are in the same relation as in the solar case. And indeed, simulating a compressible rising magnetic flux tube in a uniformly rotating, convective interior can be achieved. However, further issues arise as soon as differential rotation is considered: does rotating convection scale in the same manner as rising magnetic flux tubes? This question is non-trivial.

The β issue is not the only problem: the inhomogeneous viscosity due to AMR; the smaller time step due to compressibility; the long relaxation time that convection needs to establish; and the fact that realistic parameters for convection are still difficult to reach. All those problems are further reasons why we decided to exclude convection from our setup, and focus on the impact of rotation on the rise of magnetic flux tubes.

2.6.2 Excluding a differentially rotating background

A rotating convective spherical shell always tends to rotate differentially. But the mechanism responsible for the generation of differential rotation remains unclear. Several authors tried to generate self-consistently the solar differential rotation and still failed to obtain the exact solar differential rotation for the expected regime (Augustson et al. 2012; Guerrero et al. 2013; Gastine et al. 2014; Karak et al. 2015). Again the issue of differential rotation is a delicate question. In solar-like stars convection is the driver of differential rotation. Since we refrain from setting up a convective interior, we have no chance to self-consistently generate a differentially rotating star.

An alternative consists in externally forcing the differential rotation profile (like done by Fan 2008). Unfortunately this approach relies on a parameterization. Another alternative is to generate differential rotation thanks to the mean-field λ-effect (Rüdiger 1989; Kitchatinov & Rüdiger 2005; Küker & Rüdiger 2011), which is the result of rotating, stratified convection and can be derived quantitatively assuming mixing length theory to hold. This alternative is kept for further investigations.

Studying the rise of magnetic flux tubes in a compressible, differentially rotating, and convective environment represents a complex issue, which needs to be addressed on a life-time career. The present work is restricted to a uniformly rotating, static background.

2.6.3 Choice of a static interior

Since we exclude convection and differential rotation from our setup, we need to focus on the static properties of the stellar interior, namely stratification and superadiabaticity.

The density ratio from the surface to the radiative zone is about a few thousands. Such a stratification is possible to simulate only with an isothermal equation of state (EOS) because of the proportionality between ρ and P. But the Sun is not isothermal and we need to consider temperature variations for our problem. The standard solution consists in excluding the last 10 to 50 megameters (Mm) toward the surface where the largest density drop occurs. Stellar evolution models suggest that between 0.68 and 0.96 solar radii, the density ratio is about 45. Such a stratification can be achieved with a polytropic EOS.

Regarding the thermal character of the stellar interior, carrying a temporal and an azimuthal average of the radial profile of entropy in the convective zone leads to a slightly superadiabatic interior, $\nabla - \nabla_{\rm ad} \approx 10^{-4}$ (see Eq. (2.10) for definition of ∇). Superadiabaticity is the condition for the convective zone to be unstable against

the convective instability. But because the convective zone is only slightly unstable, a marginally stable layer is a good approximation to its thermal characteristics. Such a layer is adiabatically stratified with a polytropic index of $\gamma = 5/3$ for a mono-atomic gas.

Finally, from a stellar structure aspect differential rotation plays a minor role, whereas it becomes a crucial ingredient for the stellar dynamo mechanism. It role becomes less clear in the case of a rising magnetic flux tube. As Fan et al. (1994, Fig. 12) suggested, differential rotation and the resulting meridional circulation have a minor impact on the rise, resulting in about 5° smaller latitudinal deflection as compared to uniform rotation.

In summary, we assume that an adiabatically stratified interior with a density contrast larger than 10 and solid body rotation seems to be a relatively good approximation for the static properties of a convective interior.

Such a background stratification should be in thermal and pressure equilibrium as well as marginally stable against convection – the convective flux is zero –, and the total luminosity produced in the core should be exclusively transported to the surface by the conductive flux.

$$\mathbf{F}_{\rm tot} = \mathbf{F}_{\rm rad} \ , \tag{2.6}$$

where $\mathbf{F}_{\rm tot} = (L_0/4\pi r^2)\ \mathbf{e}_r$, and $\mathbf{F}_{\rm rad} = -\kappa\ (dT/dr)\ \mathbf{e}_r$ are the total energy flux coming from the radiative zone, and the radiative flux, respectively, with L_0, κ, and $\mathbf{e}_r$ being the total luminosity, heat conduction, and the radial unit vector in the spherical coordinate system, respectively. The force balance between the gravity and the pressure gradient guarantees pressure equilibrium. We neglect the centrifugal force and write

$$\frac{dp}{dr}\mathbf{e}_r = \rho\mathbf{g} \ , \tag{2.7}$$

with $\mathbf{g} = -\frac{GM_\star}{r^2}\ \mathbf{e}_r$; where G and $M_\star$ are the gravitational constant and the mass of the star. In order to obtain a relation between ρ, p and T, we consider the adiabatic EOS:

$$p = \frac{\rho k_{\rm B} T}{m\mu} \ . \tag{2.8}$$

Finally, we close the system with the polytropic relation of the logarithmic temperature gradient:

$$\nabla = \frac{d\ln T}{d\ln p} \ . \tag{2.9}$$

From this system we obtain a numerical value for κ, a relation for ρ, and an

ordinary differential equation for T. Eq. (2.9) can be written like

$$\nabla = \frac{p}{T} \frac{dT}{dr} \frac{dr}{dp} . \tag{2.10}$$

Introducing the force balance (2.7) in the last relation, we write

$$\nabla = -\frac{p}{T\rho} \frac{dT}{dr} \frac{r^2}{GM_\star} . \tag{2.11}$$

The adiabatic EOS (2.8) tells us that $p/(T\rho)$ is a constant. Hence,

$$\frac{p}{T\rho} = \frac{k}{m\mu} = \text{const} = \frac{\mathrm{p_0}}{\mathrm{T_0}\rho_0} , \tag{2.12}$$

where the index 0 represents the values of the quantities at the top of the domain. From Eq. (2.11), we can now express the temperature gradient:

$$\frac{dT}{dr} = -\frac{T_0\rho_0}{p_0} \frac{\nabla GM_\star}{r^2} . \tag{2.13}$$

Defining the pressure scale height at the top of the domain like

$$H_{p_0} = p_0 \left.\frac{dp}{dr}\right|^{-1}_{R_0} = -\frac{p_0}{\rho_0} \frac{R_0^2}{GM_\star} , \tag{2.14}$$

we can now identify the pressure scale height in Eq. (2.13) and obtain

$$\frac{dT}{dr} = -T_0 \frac{\nabla}{H_{p_0}} \left(\frac{R_0}{r}\right)^2 . \tag{2.15}$$

This is integrated with the boundary condition $T(R_0) = T_0$,

$$T(r) = T_0 \left[1 + \frac{\nabla R_0^2}{H_{p_0}} \left(\frac{1}{r} - \frac{1}{R_0}\right)\right] , \tag{2.16}$$

and results in the radial profile of temperature in our domain. Finally, because the adiabatic EOS is a particular case of a polytrope: $p \propto T^\nabla$, we can derive the radial profiles of pressure and density:

$$p(r) = p_0 \left(\frac{T(r)}{T_0}\right)^{1/\nabla} , \tag{2.17}$$

$$\rho(r) = \rho_0 \left(\frac{T(r)}{T_0}\right)^{1/\nabla - 1} . \tag{2.18}$$

These profiles describe the static background in which we introduce the magnetic flux

tube; they are parameterized with three parameters: ∇, H_{p_0}, and R_0. It is interesting to notice that such an interior being adiabatic has a zero entropy gradient:

$$\Delta s = c_\mathrm{v} \ln(p/p_0) - c_\mathrm{p} \ln(\rho/\rho_0) \equiv 0 \ , \tag{2.19}$$

with Δs, c_v, c_p being the entropy difference, the isochoric and isobaric heat capacities, respectively. A buoyant magnetic flux tube is unconditionally unstable in such a marginally stable interior.

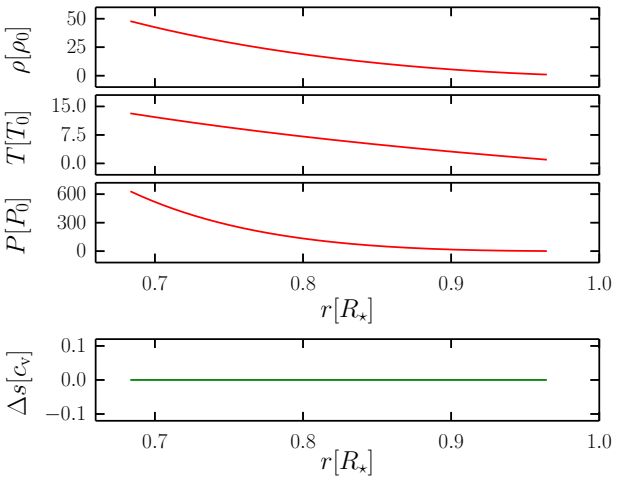

Figure 2.6: Dimensionless radial profiles of the thermodynamical quantities in the spherical shell of our setup. The three top panels represent density, temperature, and thermal pressure, scaled by their values at the top of the domain, respectively. The density ratio between the top and bottom of the domain is about 50. The bottom panel shows the specific-entropy gradient, it characterizes the adiabaticity of the stratification. Since the interior is adiabatically stratified, the entropy is constant.

In Fig. 2.6 we plot the dimensionless radial profiles of the three hydrodynamic quantities ρ, p and T and the corresponding constant entropy difference for $H_{p_0}/R_\star = 0.04$ (corresponding to the axisymmetric setup).

2.7 On the choice of boundary conditions

The total luminosity produced in the core of the star needs to be transported to the stellar surface, so we impose a constant energy flux $\mathbf{F}_\mathrm{tot}$ at the bottom of the domain. At the top boundary, we impose a constant temperature T_0 without latitudinal gradient. The latitudinal boundaries at the equator and at high latitude follow the stratification. Regarding the velocities, all boundaries are impenetrable and stress-free. For the magnetic field, the boundary conditions ensure that the field is perpendicular to the domain boundaries.

These boundary conditions are the simplest ones that can be used for such a setup. In particular, the top boundary is far from realistic and should not be compared to a stellar surface. We solve neither radiative transfer, nor cooling; the magnetic field is purely radial; we fix the temperature to a constant value; and the stratification remains much lower than in the Sun. In such a situation we focus exclusively on the dynamics of the rise throught the convection zone; emergence events at the photosphere should be addressed in a specific study.

Finally, we show the domain geometry as well as the boundary conditions and the initial condition for a non-axisymmetric rising flux tube in Fig. 2.7.

2.8 Summary

Along this chapter we introduced the numerical setup of the simulations we carried out for this work. We described the stellar background of the setup and discussed its advantages and limitations.

As a summary, we consider that magnetic flux tubes form at the tachocline, rise up to the surface and thanks to the Babcock-Leighton mechanisms reconnect with the large scale dipolar field and regenerate the poloidal field. But our simulations will focus only on the rising phase of the flux tube, because the generation phase needs too much computational time, and emergence needs to be specifically addressed because of the complexity of the processes happening at the surface.

We justified the global character of our simulations, which lead us to introduce the adaptive mesh refinement technique. This technique allows to resolve the magnetic flux tube in a large domain with a high level of precision.

Furthermore, we demonstrated on the fact that compressibility is a major aspect of our work: it is more versatile, more realistic, and has not been studied much. But it also brings constraints that force us to restrict the setup to a static background. We exclude convection because computational power still fails to achieve a realistic setup. Consequently, we exclude differential rotation because it needs convection to be self-consistent. So we chose an adiabatically stratified interior being the closest static approximation to a convective interior. We derived the static background for a $1/r^2$ gravitational acceleration, and introduced the various boundary conditions.

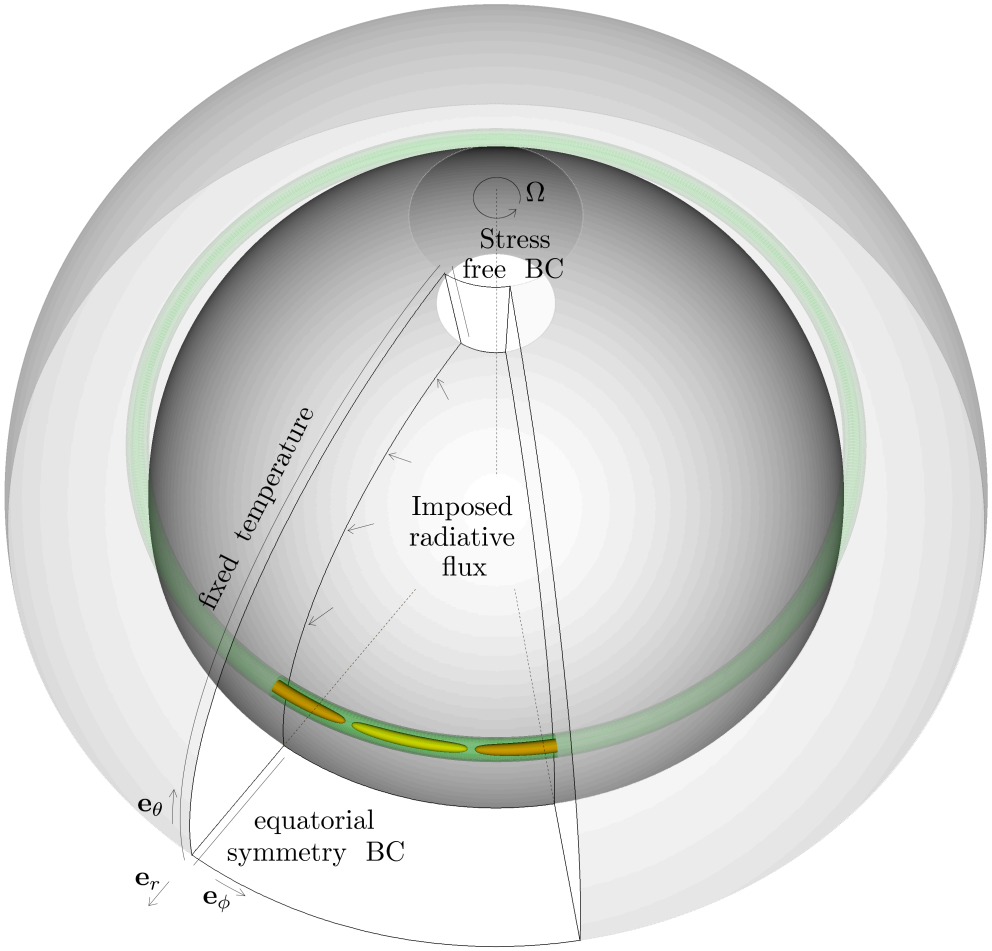

Figure 2.7: Sketch of the numerical setup for the non-axisymmetric case $m = 8$ (see Chap. 5). The simulated domain corresponds to the wedge-like shape of solid lines. At the bottom of the domain we impose a constant radiative flux; at the top a constant temperature. The latitudinal and longitudinal boundaries follow the adiabatic gradient. The boundary conditions on the velocity field are everywhere impenetrable and stress-free, except in the azimuthal direction where we impose periodic boundaries. The green contour shows a magnetic flux tube and highlight the azimuthal magnetic flux density at $r_{\rm ft} = R_{\rm ft}$ (see Chap. 4 for definitions). The yellow contour shows the part of the flux tube in non-equilibrium, which lacks entropy, called the apex. The orange contour shows the part in stable equilibrium, with an excess of entropy, called the foot.

3 Derivation of a universal parameter controling the rise of magnetic flux tubes

3.1 Introduction

In the previous chapter, we described the compressible setup that we employ to study the rise of magnetic flux tubes. In comparison to the anelastic approximation, compressibility is more realistic, but its numerical treatment limits the simulations to plasma-β up to 100. In the Sun, the plasma-β approaches 10^5 – assuming a magnetic strength at the base of the convection zone of about 10^5 G (D'Silva & Choudhuri 1993; Fan et al. 1993; Fan & Fisher 1996; Caligari et al. 1995, 1998). Can we rely on the results of compressible simulations? Simulations and reality can be compared only if the processes occurring in reality and the processes solved in the simulations occur in the same regime. Therefore, we need to identify the regime of the rise in the simulations.

Choudhuri & Gilman (1987) and later Schüssler & Solanki (1992) already addressed the question of defining the regime of the rise of a magnetic flux tube. Both teams discussed the case of the axisymmetric rise of thin magnetic flux tubes in a rotating stratified interior. They found that the magnetic Rossby number ($\mathrm{Ro_m} = v_\mathrm{A}/2H_P\Omega$) acts as a proxy for the ratio of buoyant over Coriolis force. In this chapter, we extend their work to non-axisymmetric rising flux tubes. We identify two regimes, the *buoyancy dominated* and the *rotation dominated* regime and derive a generalized form of the regime-controlling parameter they have found. In Chaps. 4 and 5, we present simulations we have carried out that verify the assumption motivating our theory (see Eq. 3.6) and that allow us to use the regime-controlling parameter to identify the nature of the regimes.

3.2 The particular case of an axisymmetric rise

The regime of a process occurring in a system is controlled by the ratio between the forces acting on the system. In the particular case of a flux tube rising in an axisymmetric manner in the rotating frame of a stratified stellar interior, magnetic and inertial forces act on the system: the magnetic buoyancy, the magnetic tension, the centrifugal force, and the Coriolis force. The centrifugal force is partially balanced by the gravitational force, it deforms the star and flattens the poles. However this effect is small in solar-like stars. We consider the star to be spherical and neglect the centrifugal force. Furthermore, in the axisymmetric case the curvature radius of the flux tube is of the order of the stellar radius, it is sufficiently large so that the tension force is also negligible.

It can be noticed that for some stellar objects these approximations do not hold. For instance, proto-stellar objects rotate much faster than main-sequence stars. In that cases the centrifugal force deforms the star significantly, affecting the direction of the buoyant force. Another example is the case of red giants. If magnetic flux tubes are still formed at the bottom of the convective zone in the deep interior of these stars, the curvature radius of flux tubes is small compared to the stellar radius and enhances the tension force. But such stellar objects are out of the scope of the current discussion. Therefore, we presume that only the buoyant force and the Coriolis force act on the system.

The ratio of $F_{\rm buoy}$ over $F_{\rm corio}$ determines which of both forces dominates the system. This ratio controls the regime of the rise of a magnetic flux tube. When this ratio is larger than unity, the regime is *buoyancy dominated*; when the ratio is less than unity, the regime is *rotation dominated*. We can express this ratio in terms of the setup parameters:

$$\frac{F_{\rm buoy}}{F_{\rm corio}} = \frac{\Delta\rho\ g}{\rho\ 2\Omega\ v_{\rm rise}}, \tag{3.1}$$

where ρ, $\Delta\rho$, $v_{\rm rise}$, $g = GM_\star/r^2$ and Ω are the the density inside the flux tube, the density difference between the flux tube and its surroundings, the rising velocity of the flux tube, the gravitational potential, and the angular velocity of the star, respectively. The only unknown is $v_{\rm rise}$, which is about $v_{\rm buoy}$ in the axisymmetric case. As in Choudhuri & Gilman (1987), the latter can be written as:

$$v_{\rm buoy} = \left[2\frac{\Delta\rho}{\rho}gl\right]^{1/2}, \tag{3.2}$$

with $l = H_p$, the local pressure scale height.

As we will see later in Chap. 4 when introducing our model of isothermal magnetic

flux tubes, the relative difference of density is equal to the inverse of the plasma-β, $\Delta\rho/\rho = 1/\beta$. Replacing $v_{\rm rise}$ and $\Delta\rho/\rho$ in Eq. (3.1), we can express the ratio of both forces as a function of their associated velocities:

$$\frac{F_{\rm buoy}}{F_{\rm corio}} = \frac{\sqrt{\gamma}}{4}\frac{v_{\rm ff}}{c_{\rm s}}\frac{v_{\rm A}}{\varpi\Omega}, \tag{3.3}$$

with $c_{\rm s}$ and $v_{\rm ff} = \sqrt{H_p g}$ being the sound speed at the bottom of the convection zone, and the free fall velocity in the stellar gravity field, respectively. $\varpi = rsin(\theta)$ is the horizontal distance from the rotation axis, such that $v_0 = \varpi\Omega$ is the rotation velocity of the flux tube. For a given star, the first factor of the rhs is a constant. So the ratio of both main forces is proportional to the ratio of the Alfvén speed and the rotation velocity at the bottom of the convection zone. We refer to this ratio as the magnetic Rossby number ($\mathrm{Ro_m}$), a slightly different number the Lehnert number (λ[1]) is used in the geo-physics community and differs from $\mathrm{Ro_m}$ by their length scales.

$$\frac{F_{\rm buoy}}{F_{\rm corio}} \propto \frac{v_{\rm A}}{\varpi\Omega} \propto \mathrm{Ro_m} \propto \lambda. \tag{3.4}$$

This number describes the balance between the magnetic energy and the kinetic energy of rotation. It is a proxy for the ratio of the two main forces and controls the regime of the rise. Again a question arises: does this number also control the regime in compressible non-axisymmetric simulations?

3.3 The effect of local tension in non-axisymmetric rise

In contrast to the axisymmetric case where magnetic flux tubes rise in the shape of an axisymmetric torus, non-axisymmetric flux tubes rise as Ω-shaped loops. We call the azimuthal wave number of their deformation m. In the present model when magnetic flux tubes enter the convective envelope and start their buoyant rise toward the surface, we assume that the wavenumber of their deformation m originates from the most unstable mode of the Parker instability. Unfortunately, the latter remains unknown, therefore the parameter m is an input parameter in our model. In the present scenario, magnetic flux tubes enter the convective envelope with alternating azimuthal chunks in stable equilibrium and chunks in non-equilibrium (cf. Fig. 2.7). The axisymmetric rise reduces to the case $m = 0$, where the flux tube is everywhere in non-equilibrium; the non-axisymmetric case consists of deformations with $m > 0$, where the flux tube is partially in non-equilibrium.

[1] In the present work λ will never refer to the Lehnert number, except in Eq. (3.4)

In contrast to axisymmetric loops, the Ω-shape of the non-axisymmetric loops enhance the tension force. Magnetic tension can be approximated as

$$F_{\rm tens} = \frac{2p_{\rm m}}{\mathcal{R}} \quad , \tag{3.5}$$

where $p_{\rm m}$ and $\mathcal{R}$ are the magnetic pressure and the curvature radius, respectively. The curvature radius of an axisymmetric flux tube ($m = 0$) is the distance between the center of the tube and the rotation axis (ϖ); the curvature radius of an Ω-shaped flux tube (m $>$ 0) is the radius of the circle fitting the shape of the Ω-loop. This radius is by construction smaller than the distance to the rotation axis. Therefore, the larger the azimuthal wavenumber m, the smaller the curvature radius ($\mathcal{R}$) and the larger the tension force. In non-axisymmetric setups, the tension force becomes the third relevant force acting on the system, with the particularity that it never dominates over the other forces – in our context, the *tension dominated* regime does not exist –, it only reduces the rising velocity, and impacts the balance between the Coriolis and the buoyant force.

The curvature radius does not only depend on the azimuthal wave number m, but also on the asymmetry of the Ω-loop. For a given m, Ω-loops are narrower in a *rotation dominated* regime than in a *buoyancy dominated* regime: the curvature radius decreases with the increase of rotation (see Chap. 5). So magnetic tension impacts the balance between the Coriolis and buoyant force, and simultaneously, the balance itself affects the magnetic tension. The magnetic Rossby number does not catch the non-linearity present in non-axisymmetric rises, this regime-controlling parameter needs to be modified to cover the general case.

From our understanding of the problem, we make the hypothesis that the reduction of the rise velocity due to magnetic tension force is inversely proportional to the curvature radius of the flux tube. We formulate this assumption as

$$\frac{v_{\rm rise}}{v_{\rm buoy}} = k\frac{\mathcal{R}}{R_\star} \quad . \tag{3.6}$$

where k is a factor which depends on several parameters (such as the viscous force, the magnetic twist, the stratification of the stellar interior, and the aspect ratio of the star) acting on the flux tube. k is influenced by m but it does not depend on the balance between the Coriolis and buoyant force. Relation (3.6) identifies the curvature radius as the characteristic length scale of the system.

3.4 Derivation of the generalized scaling parameter

From Eq. (3.6) we can extract $v_{\rm rise}$, and replace it in Eq. (3.1):

$$\frac{F_{\rm buoy}}{F_{\rm corio}} = \frac{1}{k}\,\frac{\Delta\rho\; g}{\rho\; 2\Omega\; v_{\rm buoy}}\,\left(\frac{R_\star}{\mathcal{R}}\right). \tag{3.7}$$

Because the curvature radius $\mathcal{R}$ appears in Eq. (3.7), this new relation catches the non-linearity of the non-axisymmetric rise and reveals the impact of the magnetic tension on the balance of the main forces by reducing the rising velocity. But the curvature radius itself depends on the balance between buoyant and Coriolis force. We need to formulate this back-reaction on $\mathcal{R}$ to derive a generalized definition of the scaling parameter. We use the general ansatz

$$\mathcal{R} = \varpi\beta^{f_1}\mathcal{M}_{\rm rot}^{f_2}, \tag{3.8}$$

with $\mathcal{M}_{\rm rot} = \varpi\Omega/c_{\rm s}$ being the Mach number of the rotation velocity. In Eq. (3.8), f_1 controls the back-reaction of buoyancy, f_2 of the Coriolis force. Both will be constrained later, when we explore the morphology of a rising flux tube in simulations. But we can already mention that when β decreases, the buoyancy gets stronger; the flux tube rises faster as a wide, symmetric Ω-loop and the corresponding curvature radius is large (see Chap. 5). The fact that the relation between β and the curvature radius is inverse constrains f_1 to be negative. In a similar manner, when $\mathcal{M}_{\rm rot}$ increases, rotation has a stronger influence; the flux tube rises slowly and develops narrow asymmetric loops: the curvature radius is small. Again f_2 must be negative. The $m = 0$ case further constrains the exponents since then $\mathcal{R} = \varpi$, whence $f_1 = f_2 = 0$. From Eq. (3.8) and the constraints we fixed, we replace $\mathcal{R}$ in Eq. (3.7) and rewrite the ratio of $F_{\rm buoy}/F_{\rm corio}$ as a function of three dimensionless parameters: $\mathcal{M}_{\rm ff}$, $\mathcal{M}_{\rm rot}$ and β.

$$\frac{F_{\rm buoy}}{F_{\rm corio}} = \frac{1}{2k\sqrt{2}}\,\mathcal{M}_{\rm ff}\,\left(\frac{1}{\mathcal{M}_{\rm rot}}\right)^{1+f_2}\left(\frac{1}{\beta}\right)^{\frac{1}{2}(1+2f_1)}, \tag{3.9}$$

where $\mathcal{M}_{\rm ff} = \sqrt{gR_\star}/c_{\rm s}$ is the Mach number of the free fall velocity. Eq. (3.9) is the general form of the ratio of the two main forces acting on the system. In contrast to Eq. (3.3), Eq. (3.9) is valid for any m including $m = 0$.

We can now introduce a new dimensionless number $\Gamma_{\alpha_1}^{\alpha_2}$ as

$$\Gamma_{\alpha_1}^{\alpha_2} = \left[\frac{v_{\rm A}^{\alpha_1} c_{\rm s}^{1-\alpha_1}}{\varpi\Omega}\right]^{\alpha_2} \tag{3.10}$$

where α_1 and α_2 are both functions of f_1 and f_2, whence functions of m, such that

$$\begin{aligned} \alpha_1 &= \frac{1+2f_1}{1+f_2}, \\ \alpha_2 &= 1+f_2. \end{aligned} \tag{3.11}$$

Identifying $\Gamma_{\alpha_1}^{\alpha_2}$ in Eq. (3.9), we obtain a simplified version of this relation:

$$\frac{F_{\text{buoy}}}{F_{\text{corio}}} = \left[\frac{\mathcal{M}_{\text{ff}}}{2k\sqrt{2}}\left(\frac{\gamma}{2}\right)^{\frac{\alpha_1\alpha_2}{2}}\right] \Gamma_{\alpha_1}^{\alpha_2} \tag{3.12}$$

And because the first factor of the rhs is a constant (for a given m), $\Gamma_{\alpha_1}^{\alpha_2}$ acts as a proxy for the ratio of the main forces. $\Gamma_{\alpha_1}^{\alpha_2}$ is a general form of the scaling parameter that controls the regime of the rise of magnetic flux tubes.

In the axisymmetric case ($m = 0$) where α_1 and α_2 are unity, $\Gamma_{\alpha_1}^{\alpha_2}$ equals Ro_m. Γ_1^1 controls the regime of the axisymmetric case. In the non-axisymmetric cases, $\Gamma_{\alpha_1}^{\alpha_2}$ also controls the regime, but because of the lack of constraints on α_1 and α_2 and their dependence on m, we need to extract them from the simulations. In the next section, we suggest a method to compute f_1 and f_2 and thereby α_1 and α_2.

3.5 A method to verify the hypothesis

We suppose that magnetic tension – due to the Ω-shape of the rising loops – reduces the rise velocity. Therefore, the reduction is inversely proportional to the curvature radius $\mathcal{R}$. Thanks to this assumption, we derived a general form of the scaling parameter $\Gamma_{\alpha_1}^{\alpha_2}$.

Schüssler & Solanki (1992) introduced the relative rise time $\tilde{\tau}_{\text{rise}}$ of an axisymmetric thin flux:

$$\tilde{\tau}_{\text{rise}} = \frac{\tau_{\text{rise}}}{P_{\text{rot}}}, \tag{3.13}$$

with τ_{rise} and P_{rot} being the rise time of the flux tube and the rotation period of the star, respectively. They have shown that $\tilde{\tau}_{\text{rise}}$ scales with Γ_1^1. Therefore, our theory predicts that for a given $\Gamma_{\alpha_1}^{\alpha_2}$ there will be a unique relative rise time independently of β and $\mathcal{M}_{\text{rot}}$. So if we verify the scaling behavior of $\tilde{\tau}_{\text{rise}}$ with $\Gamma_{\alpha_1}^{\alpha_2}$, we will confirm our assumption.

In order to verify the scaling behavior of $\tilde{\tau}_{\text{rise}}$ with $\Gamma_{\alpha_1}^{\alpha_2}$, we first need to study the impact of compressibility – carrying out *axisymmetric*, *compressible* simulations, see Chap. 4 – and the impact of non-axisymmetry – carrying out *non-axisymmetric*, *compressible* simulations, see Chap. 5. Non-axisymmetry poses a problem: we miss numerical values for α_1 and α_2. To obtain this values, we suggest to measure the

curvature radius of the Ω-loops. The resulting dependence of $\mathcal{R}$ on β and $\mathcal{M}_{\rm rot}$ will provide the missing numerical values to predict $\Gamma^{\alpha_2}_{\alpha_1}$.

- If the relative rise time indeed scales with $\Gamma^{\alpha_2}_{\alpha_1}$, this will justify the hypothesis Eq. (3.6) and show that the magnetic tension of the Ω-loops does influence the dynamics of the rise.
- If the relative rise time does not scale, two conclusions can be made. The method we use to compute the curvature radius lacks precision; or the magnetic tension is not a major player in the force balance controlling the regime, and other effects need to be considered such as viscous force, thermal conduction, and kink instability.

But the theory has some inherent limits. We are allowed to compare real stars and numerical simulations only when they operate in the same regime. But obviously this only holds for scalable quantities (e.g. $\tilde{\tau}_{\rm rise}$). The plasma-β, $\mathcal{M}_{\rm rot}$ and $\mathcal{R}$ clearly do not belong to this category; for a given $\Gamma^{\alpha_2}_{\alpha_1}$, their values can differ, but the balance of their effects remains the same. Therefore, in contrast to anelastic simulations where β can be of the order of realistic values (10^5), compressible simulations ($\beta < 100$) always overestimate the curvature radius with respect to reality. For a given regime, Eq. (3.9) allows us to write a relation between β and $\mathcal{M}_{\rm rot}$

$$\mathcal{M}_{\rm rot} \propto \beta^{-\alpha_1/2}. \tag{3.14}$$

This relation can be reintroduced in Eq. (3.8) and

$$\mathcal{R} \propto \beta^{(\alpha_1-1)/2}. \tag{3.15}$$

So, for $\beta_{\rm real}/\beta_{\rm sim} = 10^3$ the simulation overestimates $\mathcal{R}_{\rm real}$ such that

$$\mathcal{R}_{\rm real} \approx \mathcal{R}_{\rm sim} 10^{3(\alpha_1-1)/2}\ , \tag{3.16}$$

where the index $(.)_{\rm real}$ and $(.)_{\rm sim}$ refer to the quantity that should be observed in reality, and the quantity we measure in compressible simulation that operates in a realistic regime, respectively. This overestimation naturally varies with m. In the axisymmetric case for instance, the curvature radius remains ϖ independently of the regime ($\alpha_1 = 1$ so there is no overestimation). For larger m, the overestimation will grow according to α_1. In Chap. 5 we will show that for the $m = 8$ case $\alpha_1 = 0.793$. In that case, $\mathcal{R}_{\rm real} \approx \mathcal{R}_{\rm sim}/2$.

A further issue resides in the proportionality between $\Gamma^{\alpha_2}_{\alpha_1}$ and $F_{\rm buoy}/F_{\rm corio}$. As seen in Eq. (3.12), we could derive the proportionality factor, but k remains unknown, and

prevents us from identifying when $F_{\text{buoy}}/F_{\text{corio}}$ becomes unity. So far, the theory fails in differentiating the nature of the regime. But in Chaps. 4 and 5, we will estimate k thanks to a morphologie argument. We will demonstrate there that the factor in front of $\Gamma_{\alpha_1}^{\alpha_2}$ in Eq. (3.12) approximates 0.7 for the axisymmetric case and 0.4 for the non-axisymmetric $m = 8$ case.

3.6 Summary

Along this chapter, we have designed a theory extending the original work of Choudhuri & Gilman (1987) to non-axisymmetric geometry. The theory regards the effect of the magnetic tension on the rising Ω-loops in non-axisymmetric simulations. The tension force acts on the balance between the buoyant and Coriolis forces by reducing the rise velocity. We have derived a generalized proxy ($\Gamma_{\alpha_1}^{\alpha_2}$) for the ratio of the buoyant and Coriolis forces, which controls the regime. In contrast to former results, the generalized proxy is valid for axisymmetric and non-axisymmetric geometries. This proxy allows us to justify that, even though the numerical parameters are far from the realistic parameter space (about three orders of magnitude off), we can guess the regime of the simulations, and therefore design numerical experiments obeying the same regime as in the solar case. We have suggested a method to verify the hypothesis carrying the theory: verifying that the relative rise time scales with the predicted scaling parameter in compressible axisymmetric and non-axisymmetric simulations. We also underlined the intrinsic limits of the scaling procedure: an overestimation of the curvature radius and the failing of $\Gamma_{\alpha_1}^{\alpha_2}$ in identifying the exact limit between the regimes and provides only an order of magnitude. Finally, we want to underline that convection and differential rotation are not present in our model, and therefore are excluded from the theory. Both ingredients affect the relative rise time and considering them may change our conclusions. The present work focuses on the behavior of rising magnetic flux tubes in non-convective and uniformly rotating interiors, so that we could evaluate quantitatively (and not just qualitatively) the impact of convection and differential rotation, when it will be possible to carry out such complex numerical experiments for compressible MHD.

4 Validation of the setup in 2D

4.1 Introduction

In the first chapter, we described the stellar environment of our setup, in the second chapter we introduced a theory predicting the behavior of the magnetic flux tube in such an interior, for axisymmetric and non-axisymmetric simulations. The present chapter aims to validate the setup.

To do so we carry out a relatively large series of about 30 simulations and verify that the relative rise time scales with Γ_1^1 as predicted in the last chapter.

By identifying the existence of two regimes, we qualitatively compare our results with the ones obtained from thin flux tube simulations. We study the morphological characteristics of the rising magnetic flux tube: its path and its latitudinal deflection; and discuss the relevance of compressibility for these aspects of the rise.

The final goal of this chapter is to extract a scaling relation for the relative rise time, which we plan to introduce in a delayed Babcock-Leighton dynamo.

But before going any further, we need to discuss the precise initial state of the magnetic flux tube and underline the assumption it implies: namely axisymmetry.

4.2 The numerical experiment

4.2.1 An unstable axisymmetric flux tube a the bottom of the convection zone

We define an axisymmetric flux tube as a torus being bounded by twisted magnetic field lines. The magnetic flux going through a meridional section of such a coherent magnetic structure stays constant all along its azimuthal span. This magnetic configuration has been shown to be unstable in an adiabatically stratified medium. The stability criterion is $\nabla - \nabla_{\rm ad} > -1/\gamma\beta$ (Parker 1955; Spruit & van Ballegooijen 1982), therefore in the case of an adiabatically stratified medium $\nabla - \nabla_{\rm ad} \equiv 0 > -1/\gamma\beta$, the flux tube is unconditionally unstable. In the present scenario we introduce an unstable axisymmetric flux tube at the bottom of the convective zone, and let it rise toward the surface. We plan to extract the relative rise

time of a magnetic flux tube, excluding the time needed by the Parker instability to develop. The formation phase of magnetic flux tubes lasts longer than the rise time (Schüssler 1979), therefore, like Fan (2008) and Jouve & Brun (2009), we exclude this phase from the simulations and save computational time. Instead, we assume that the azimuthal mode with the largest growth rate has a wavenumber $m = 0$. At $t = 0$, the flux tube enters the convective zone as an axisymmetric torus being in buoyant non-equilibrium everywhere.

4.2.2 Description of the initial condition

A flux tube consists of concentric magnetic tube-shaped surfaces. In order to define its position and shape, it is useful to consider the line going through the common centers of the meridional sections of the tubes. At $t = 0$, $(r_\mathrm{i}, \theta_\mathrm{i})$ are the coordinates of the center of the concentric magnetic surfaces on a given meridional section. Because of the axisymmetry, $(r_\mathrm{i}, \theta_\mathrm{i})$ are both independent of ϕ, and we can simulate the rise of an axisymmetric flux tube in any meridional section of the star.

We are interested in "thick" flux tubes, i.e. the thermal and magnetic properties of the flux tube vary across its diameter. We parameterize the profile of the magnetic flux density in the flux tube's reference frame. The coordinates of a given point in this frame are $(r_\mathrm{ft}, \theta_\mathrm{ft})$. Where r_ft is the distance of a point to the center of the flux tube $(r_\mathrm{i}, \theta_\mathrm{i})$ and θ_ft is a "latitudinal" coordinate of the same point in the flux tube reference frame. From such a frame we design profiles for the different components of the magnetic field. The longitudinal component is defined as:

$$B_\mathrm{l}(r_\mathrm{ft}) = B_0 \ \exp\left(-\frac{r_\mathrm{ft}^2}{R_\mathrm{ft}^2}\right), \tag{4.1}$$

where B_l, B_0, and R_ft are the longitudinal magnetic field, the magnetic flux density at the center, and the radius of the flux tube, respectively. In the case of an axisymmetric flux tube, B_l is purely azimuthal, and corresponds to the ϕ-component of the magnetic field vector. It depends only on r_ft (and therefore on both spherical coordinates r and θ). R_ft defines the circle enclosing about 98% of the total magnetic flux (see Cheung et al. 2006), we call it the flux tube radius. Constructed as such, the radial profile of the longitudinal magnetic field is divergence free.

While rising, the viscous force may disturb the magnetic flux tube; it loses coherence and eventually magnetic flux. To avoid such a situation, the flux tube needs to be twisted (Moreno-Insertis & Emonet 1996; Moreno-Insertis 1997), therefore it has a poloidal component B_p. To ensure that the poloidal component is divergence-free,

we derive it from the vector potential A_l:

$$-\frac{dA_\mathrm{l}}{dr_\mathrm{ft}} = B_\mathrm{p}(r_\mathrm{ft}) = \lambda \frac{r_\mathrm{ft}}{R_\mathrm{ft}} B_\mathrm{l}(r_\mathrm{ft}) \ , \tag{4.2}$$

where A_l is the longitudinal component of the magnetic vector potential $\mathbf{A}$. λ is the so called *twist* parameter. In this experiment we use $\lambda = 0.5$ (alike in Jouve & Brun 2009).

The various dimensionless magnetic profiles we described are plotted in Fig. 4.1. We show the longitudinal magnetic profile, the poloidal magnetic profile, and the resulting total magnetic pressure; in the frame of a twisted magnetic flux tube.

We refer to B_0 as the magnetic flux tube strength, because as seen in Fig. 4.1, its value corresponds to the maximum of the magnetic field inside the flux tube (for a twist parameter less than unity).

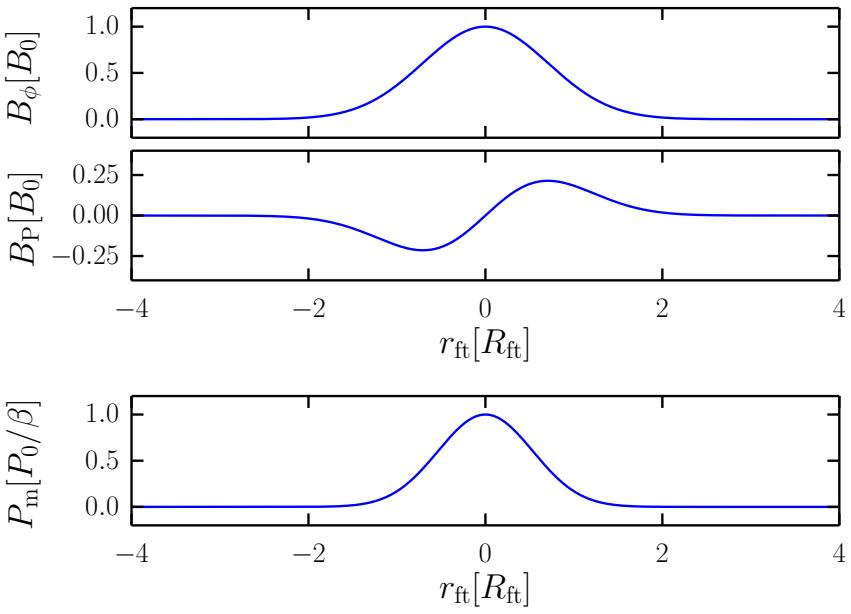

Figure 4.1: Magnetic profiles in the frame of a twisted magnetic flux tube, with $\lambda = 0.5$. Here, we plot the radial profiles (in units of the flux tube radius R_ft) of the two components of the magnetic field: B_ϕ and B_p in units of B_0; we also plot the magnetic pressure in units of P_0/β. This unit system was chosen so that the profiles are valid for any β.

Now that we introduced a complete description of the magnetic components of the flux tube, we need to describe its thermal state. All along its rise, the flux tube stays in pressure balance at all points:

$$p_\mathrm{i} + p_\mathrm{m} = p_\mathrm{e}, \tag{4.3}$$

where p_i, p_m are the thermal and magnetic pressure ($B^2/2\mu_0$) inside the flux tube,

respectively. p_e is the thermal pressure at the corresponding depth in the absence of a flux tube. Thanks to $\beta = p_e/p_m$, we can transform Eq. (4.3) into a dimensionless relation:

$$\frac{p_i}{p_e} = 1 - \frac{p_m}{p_e} = 1 - \frac{1}{\beta}, \tag{4.4}$$

with β being the plasma-β with respect to the stellar interior, not to be confused with the plasma-β of the flux tube itself: $\beta_{ft} = p_i/p_m$. The dimensionless pressure equilibrium Eq. (4.4) measures the impact of the magnetic pressure on the thermal pressure in the absence of flux tubes. But this is not sufficient, we need to close the system to find the relation between pressure, temperature, and density.

In the present scenario, the simulation starts when the flux tube enters the convective zone. At that point in time, the instability is fully developed, and the flux tube is everywhere in buoyant non-equilibrium. Regarding the various relevant time scales, the destabilization phase lasts for about 6 years (Schüssler 1979), whereas the rising phase lasts for about one month (Schüssler et al. 1994). The temperatures outside and inside the flux tube adjust on a time scale of about $\tau_{cond} = R_{ft}^2/\kappa$, which is a few months; it is short compared to the destabilization phase, and long compared to the rising phase. Therefore, during the destabilization phase, the temperature adjusts nearly instantaneously ($\tau_{cond} \ll 6\,\mathrm{yr}$). The magnetic flux tube remains in thermal equilibrium with its surrounding, it is isothermal: $T_i = T_e$. But in the rising phase, τ_{cond} lasts longer than the dynamical time scale: the flux tube does not remain isothermal. Considering the adiabatic equation of state (EOS) and an isothermal flux tube, the ratio of pressures initially equals the density ratio,

$$\frac{p_i}{p_e} = \frac{\rho_i}{\rho_e}. \tag{4.5}$$

Using Eq. (4.4) and Eq. (4.5) we write the density difference between the flux tube and the stellar interior (considering β greater than 1, see discussion in Sect. 2.2 of Jouve et al. 2013) as

$$\frac{\Delta\rho}{\rho_e} = \frac{1}{\beta}. \tag{4.6}$$

Therefore, the buoyancy, in the case of an isothermal flux tube, depends directly on the β parameter.

We have now completely described the magnetic flux tube: it is defined by its position (r_i, θ_i), its radius R_{ft}, its magnetic field strength B_0, its twist λ, its thermal state (isothermal) and the choice of an EOS, in that case adiabatic. These parameters defining the magnetic flux tube are summarized in Table 4.1 in the section "Flux tube parameters". Note that one of the input parameters is β, from which B_0 will be computed.

Describing the flux tube is not sufficient to entirely describe the simulation. We need to constrain the stellar interior. As discussed in Chap. 2, three parameters are sufficient: ∇, $\chi = H_{p0}/R_\star$ and R_0, their respective values are summarized in Table 4.1 in the section "Stellar parameters".

The last missing ingredient is rotation. As we already mentioned, two forces mostly act on the flux tube: the buoyant force, controlled by β; and the Coriolis force, controlled by the rotational Mach number $\mathcal{M}_{\rm rot} = \varpi\Omega/c_{\rm s}$ with ϖ, Ω and $c_{\rm s}$ being the distance between $(r_{\rm i}, \theta_{\rm i})$ and the rotation axis of the star, the angular velocity of the star, and the sound speed at $r = r_{\rm i}$, respectively. For a given stellar interior and a given flux tube, this dimensionless parameter is the second input parameter. It allows to compute the angular velocity of the star Ω.

Table 4.1: Parameters and initial conditions for the STD-2D case.

Numerical parameters			
Resolution			$[512 \times 1024]$
AMR levels			2 levels
Effective resolution			$[2048 \times 4096]$
Domain definitions			
Radial domain		$[R_\star]$	$[0.684 - 0.964]$
Latitudinal domain		$[\pi]$	$[0.05 - 0.5]$
Flux tube parameters			
Initial depth:	$r_{\rm i}$	$[R_\star]$	0.71
Initial latitude:	$\theta_{\rm i}$		$20°$
Initial radius:	$R_{\rm ft}$	$[R_\star]$	10^{-3}
Initial twist:	λ		0.5
Plasma-β:	β		input
Stellar parameters			
Reference radius:	R_0	$[R_\star]$	0.964
Adiabaticity:	∇		0.4
Pressure scale height:	χ		0.013
Stratification:	$\rho_{\rm bot}/\rho_{\rm top}$		≈ 50
Rotational Mach number:	$\mathcal{M}_{\rm rot}$		input

4.3 Verifying the scalability of the setup

Our setup has two input parameters: β and $\mathcal{M}_{\rm rot}$. To compare our results with former studies, we should ensure that the simulations occur in a compatible regime. The values of the input parameters used in the literature are, however, out of reach for compressible simulations. As usual when carrying out numerical experiments, resolution is the limiting factor. Since compressible simulations are fully non-linear, we cannot resolve the entropic signal of a realistic flux tube. This lack of precision leads to a maximum limit on the plasma-β of up to 10^2, which differ from the probable solar value by three orders of magnitude. Is it possible to realize a simulation with a lower β but still in the same regime as the Sun?

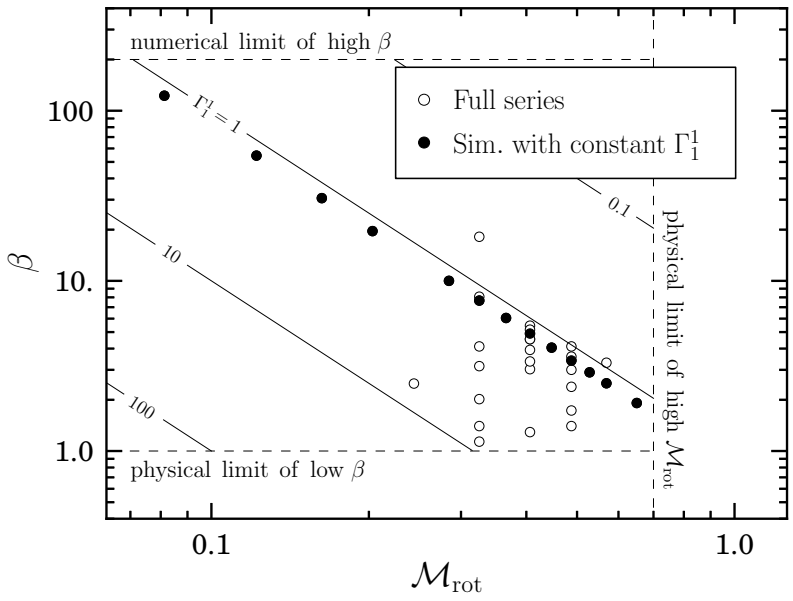

Figure 4.2: Graphical representation of the parameter study. Each symbol represents a simulation. The symbol's coordinates are the input parameters of the corresponding simulation. The exact values are listed in Table A.1. The closed symbols correspond to a subcategory of the series with a constant $\Gamma_1^1 = 1.217$. The dashed lines represent the numerical and physical limits, crossing them leads to unreliable results. The thin solid lines are isolines for Γ_1^1 with the indication of their respective value.

4.3.1 Carrying out a parameter study

Schüssler & Solanki (1992) have shown that the relative rise time $\tilde{\tau}_{\rm rise}$ of an axisymmetric thin magnetic flux tube scales with Γ_1^1. We want to verify if this holds for compressible simulations. In order to demonstrate the scalability of the setup, we carry out a parameter study in the (β, $\mathcal{M}_{\rm rot}$) parameter plane. In Fig. 4.2 we plot

each simulation as a point whose coordinates are the input parameters in the (β, $\mathcal{M}_{\mathrm{rot.}}$) plane. The figure also shows that our setup is framed with numerical and physical boundaries. Across these boundaries, we consider simulations either unphysical or not reliable because of numerical artefacts. Above the high-β boundary, the resolution fails to resolve the entropy signal of the flux tube. The low-β and the high-$\mathcal{M}_{\mathrm{rot}}$ limits are physical boundaries. When β becomes lower than unity, the plasma becomes magnetically dominated, while in solar-like stars the plasma of the convective zone is thermally dominated. Even though the setup may scale and thereby allow us to use non-realistic β, the nature of the plasma should remain thermally dominated. In the same manner, the solar rotation flow is subsonic, therefore $\mathcal{M}_{\mathrm{rot}}$ should be less than unity.

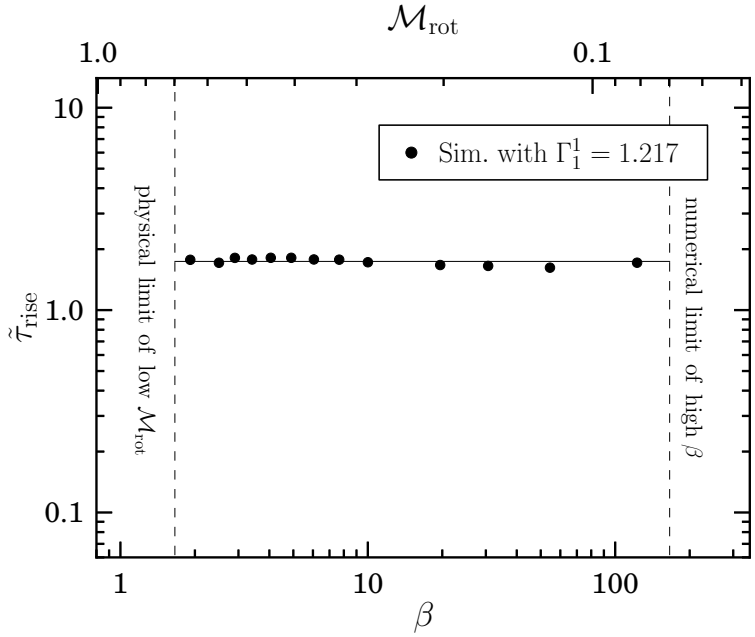

Figure 4.3: Plot of the relative rise time of the sub-series with $\Gamma_1^1 = 1.217$ (the black points on Fig. 4.2) over β and the corresponding $\mathcal{M}_{\mathrm{rot}}$ (upper axis). The thin solid line is a least-squares fit of the data points. For a given Γ_1^1, the relative rise time ($\tilde{\tau}_{\mathrm{rise}}$) remains constant. The dashed lines correspond to the numerical and physical limits of the setup.

4.3.2 Verifying the scalability of the setup

In order to verify the scalability of our setup we focus on the relative rise time of the magnetic flux tube and on the path taken by the flux tubes. In Fig. 4.2 the closed symbols correspond to simulations with a constant $\Gamma_1^1 = 1.217$. In Fig. 4.3 we plotted the relative rise time $\tilde{\tau}_{\mathrm{rise}}$ of these simulations versus their respective β

parameter. In the same figure, the upper axis indicates the corresponding $\mathcal{M}_{\rm rot}$. We vary β and $\mathcal{M}_{\rm rot}$ by two and one order of magnitude, respectively, and still recover the same relative rise time. This plot suggests that the setup can be scaled according to Γ_1^1: we are confident that even with a $\beta = 10^5$, if the $\mathcal{M}_{\rm rot}$ is set such that Γ_1^1 stays constant, the relative rise time will remain unchanged. This agrees with both, the prediction we have made in Chap. 3, and the former studies of Choudhuri & Gilman (1987) and Schüssler & Solanki (1992).

Not only the relative rise time scales with Γ_1^1, but also the path of the rise. It can be seen in panel (*a*) of Fig. 4.4: we show the paths taken by two different magnetic flux tubes, rising in the same regime with different rotation rates. The red contours represent the magnetic flux density of a weak magnetic flux tube, rising in a slow rotating star; the green contours show a strong magnetic flux tube, rising in a fast rotating interior. In both cases the magnetic flux tube takes an identical path, and emerges at the same latitude. Both setups have a Γ_1^1 of 1.217.

This proves that our setup does scale, and that Γ_1^1 is indeed a scaling parameter controlling the regime of axisymmetric rises.

4.4 A qualitative exploration of the morphological characteristics

Two main forces act on the magnetic flux tube while rising: the buoyant force and the Coriolis force. Which of the two dominates depends on the regime. We take the example of a standard simulation with Γ_1^1 about unity and discuss the differences between a *buoyancy dominated* regime and a *rotation dominated* regime.

Initially, the flux tube sits at the bottom of the convective zone. The flux tube is everywhere in non-equilibrium, and only the buoyant force acts on it (magnetic tension in such a tube is negligible). The flux tube rises in the radial direction. In our setup, numerical diffusion transfers less than 5% of the flux tube's angular momentum to the stellar interior along the entire rise. Therefore, we assume that the angular momentum within the flux tube is a conserved quantity.

The path taken by the flux tube results from the competition between the inertial and buoyant forces. The inertial force attempts to maintain the magnetic flux tube at $\varpi = \text{const}$; the buoyant force moves the magnetic flux tube radially. Initially the buoyant force is larger than the inertia, is that it moves away from the rotation axis and decelerates azimuthally to conserve angular momentum. While the magnetic flux tube rises, the external pressure decreases. Because of pressure balance, the flux tube is forced to extend and its buoyancy decreases. As a result, inertia may

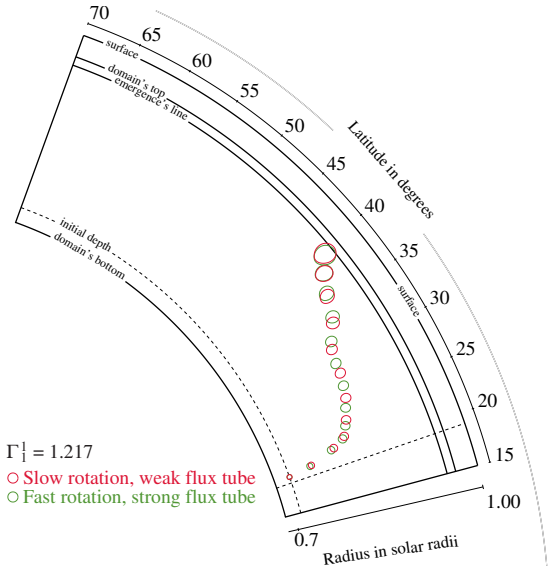

(*a*) two different cases in the same regime

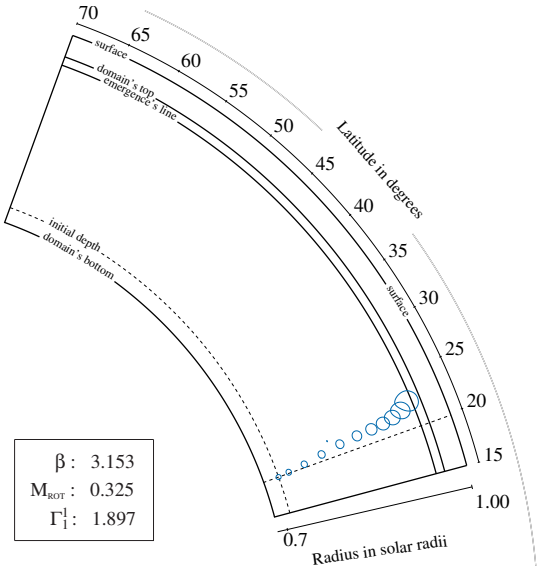

(*b*) case for stars rotating more slowly than the Sun or with stronger flux tubes

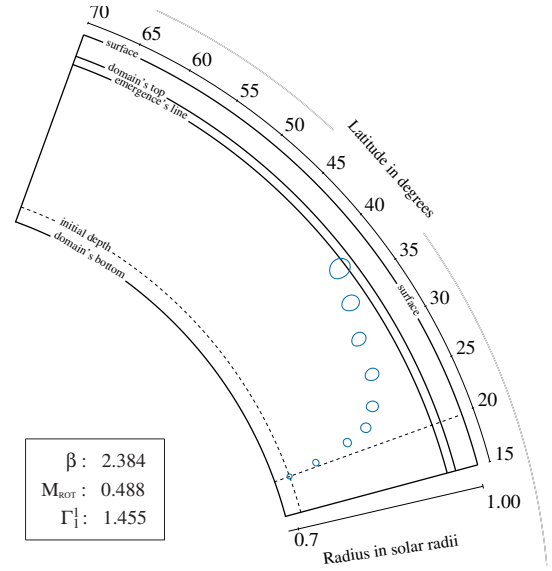

(*c*) case closest to the solar case

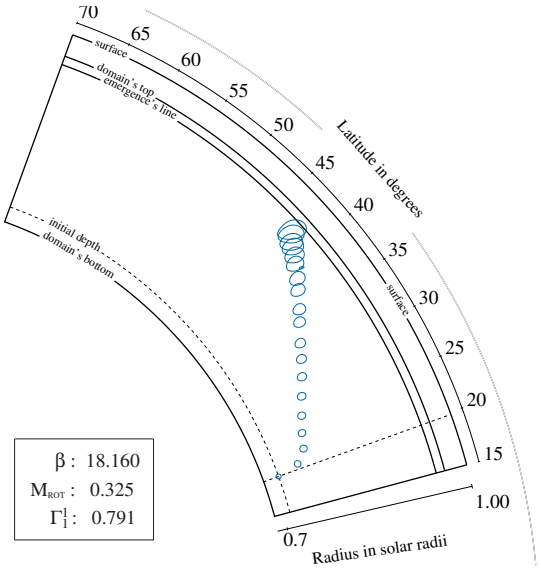

(*d*) case for stars rotating faster than the Sun or with weaker flux tubes

Figure 4.4: Cross-sections of magnetic flux tubes at various times for five representative simulations. The series of cross-sections illustrate the path taken by the flux tube all along its rise. (*a*) is a plot of two simulations with the same Γ_1^1 (same regime): the green contours correspond to a strongly buoyant flux tube in a rapidly rotating interior (*a*1 in Table A.1), the red contours correspond to a weakly buoyant flux tube in a slowly rotating interior (*a*2 in Table A.1). (*b*), (*c*), and (*d*) show the paths for three different Γ_1^1. For the *buoyancy dominated* regime (high Γ_1^1) in (*b*), the path is mainly radial, whereas in (*c*) and (*d*), the path becomes more and more parallel to the axis of rotation as Γ_1^1 decreases and the regime becomes more *rotation dominated*. The input parameters of the simulations can be found in Table A.1, referred to their respective labels.

dominate buoyancy at some point and the magnetic flux tube follows a path parallel to the rotation axis. In the rotating frame, this may be translated as follow: the azimuthal deceleration of the flux tube builds up a Coriolis force, that acts in the perpendicular direction to the rotation axis, pointing toward the rotation axis. This force balances the horizontal component of the buoyant force, until the horizontal, resulting force vanishes. As a results, the flux tube rises in a purely axial manner. When the buoyant force dominates during the entire rise, the flux tube emerges almost at its initial latitude θ_i, whereas when inertia dominates the magnetic flux tube is deflected latitudinally and emerges at higher latitude (Fan 2008, Sect. 3.1).

On the other hand, while the flux tube rises, it cools due to thermal conduction. Conduction is driven by κ which we keep constant in all series. Because of the constraint of pressure balance, as temperature decreases, density has to increase accordingly. The reduced lack of density decreases buoyancy and thereby the rise velocity of the flux tube. Because the conduction time scale $\tau_\mathrm{cond} = R_\mathrm{ft}^2/\kappa$ lasts about 10 rise times, this effect does not play a major role in our simulations, but it has been discussed in detail by Weber & Fan (2015).

To conclude, the azimuthal deceleration caused by the conservation of angular momentum deflects the magnetic flux tube toward the poles. The time needed for the inertial force (Coriolis force in the rotating frame) to build up depends on the regime of the rise. The scaling parameter Γ_1^1 controls the regime and thereby the path taken by the flux tube.

In Fig. 4.4 the panels (*b*), (*c*) and (*d*) consist of three representative simulations in different regimes. The (*b*) panel represents a rising magnetic flux tube in the *buoyancy dominated* regime. The buoyant force acting on the magnetic flux tube dominates its inertia during its entire rise. The resulting Coriolis force builds up slowly and the deflection appears late in the rise. One can notice that deflection starts shortly before emergence.

The further the regime tends toward the *rotation dominated* regime, the earlier inertia takes over buoyancy and the earlier the Coriolis effect appears and thereby the latitudinal deflection of the flux tube. This can be seen in the panels (*c*) and (*d*). In panel (*c*), the flux tube rises in a *balanced regime*, inertia starts to dominate at about half of the rise. At the beginning, it rises in a radial manner, and while the Coriolis force builds up, the horizontal component of the resulting force diminishes, and the path taken by the flux tube becomes progressively vertical. In panel (*c*), one can notice how the flux tube oscillates slightly around a constant angular momentum line: the vertical line crossing the surface at about 43° latitude. These oscillations have been already discussed in Moreno-Insertis et al. (1992).

In panel (*d*) the effect of the Coriolis force appears at the earliest. The flux tube

is in a *rotation dominated* regime. The buoyant force is weak and inertia takes over very early in the rise, and the Coriolis force grows on a short time scale. As a result the flux tube deflects from the radial direction in very beginning of its rise. It forces the flux tube to follow a line of constant ϖ. Unlike panel (*c*) the flux tube does not oscillate, because the response time scale of the Coriolis force is much shorter in this regime. This regime leads to the largest deflection, therefore to the highest latitude of emergence.

4.5 The scaling relation of the relative rise time

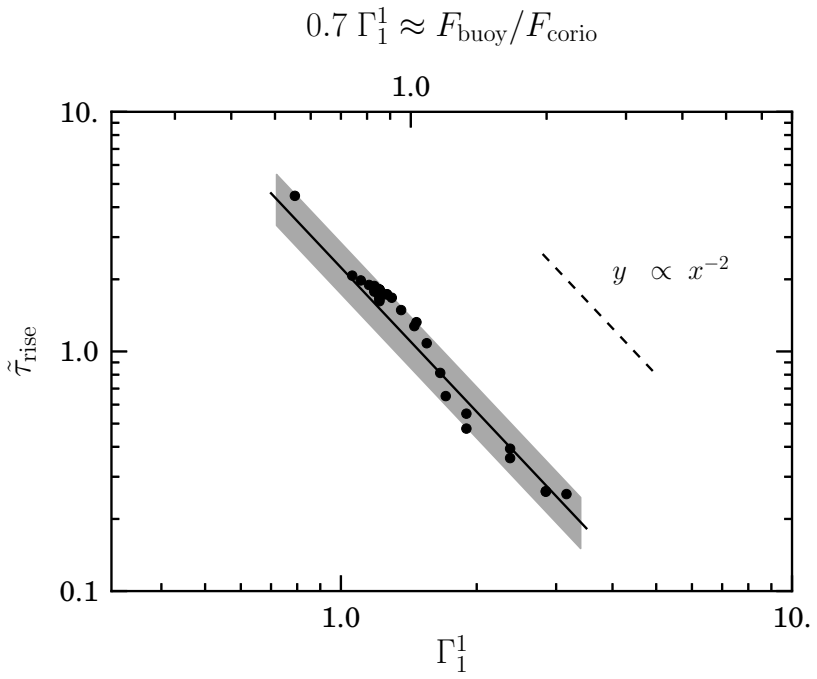

Figure 4.5: Plot of the relative rise time versus the proxy for the force ratio, Γ_1^1. The solid line is a least squares fit of the data points. The dashed line indicates a power of -2. On the upper axis, we indicate the corresponding $0.7\Gamma_1^1$ values which are the closest estimates of $F_{\rm buoy}/F_{\rm corio}$ we could extract from our simulations. The grey zone marks the spread of data points from the fit and gives an idea of the scatter.

As we just discussed, the path and the rise velocity change accordingly to the regime. A *buoyancy dominated* rising flux tube takes a short path at a high rise velocity. On the contrary, a *rotation dominated* rising flux tube, takes a longer path at a slower rising velocity. The relative rise time of the flux tube varies with the regime. We extract the relative rise time of each simulation and plot it (in a log-log scale) in Fig. 4.5 against the scaling parameter Γ_1^1. The resulting function has a small scatter, which confirms the uniqueness of the solution: for a given Γ_1^1 we

obtain a single relative rise time. This function is scale-free, it is a powerlaw:

$$\tilde{\tau}_{\text{rise}} \propto \left(\Gamma_1^1\right)^{-2} \tag{4.7}$$

The relative rise time follows a powerlaw of exponent -2. This result agrees with Schüssler & Solanki (1992), who found the same exponent under the thin flux tube approximation. We can conclude that compressibility does neither influence the regime, nor the relative rise time.

In Chap. 3, Eq. (3.12), we have shown that Γ_1^1 is a proxy for the ratio of the main forces and therefore Γ_1^1 controls the regime of the rise, but the proportionality factor remains unknown. We suggest a way to obtain an order of magnitude of this factor thanks to a morphological argument. In panel (c) of Fig. 4.4, the path of the flux tube starts to deflect at about half of the convective zone. In that case the main forces balance each other, the ratio is about unity. In this simulation $\Gamma_1^1 \approx 1.5$, therefore the proportionality factor is near 0.7. On the upper axis of Fig. 4.5, we indicate 0.7 Γ_1^1, representing the closest estimate of the main-forces ratio we can compute. This estimation and Fig. 4.5 tell us that a magnetic flux tube rising in a *balanced regime* will reach the surface in about a rotation period. In the solar case, this results in a flux tube with a magnetic field strength of $B_0 \approx 5 \cdot 10^4$ G. This results agrees qualitatively with former results (Fan et al. 1994; Choudhuri & Gilman 1987; Schüssler et al. 1994).

4.6 Summary

The aim of this chapter is to validate the setup we introduced in Chap. 2. We discussed the scenario of the simulations we carried out. An unstable magnetic flux tube sitting in the tachocline develops a Parker instability and rises toward the surface. The major assumption is that the wavenumber of the azimuthal mode with the largest growth rate is $m = 0$.

We described the initial conditions of the simulations and listed the relevant parameters. We defined a magnetic flux tube and underlined the input parameters of our numerical experiments, β and $\mathcal{M}_{\text{rot}}$.

We carried out a parameter study on these parameters, and demonstrate that the relative rise time does scale with the proxy parameter described in Chap. 3: Γ_1^1.

For a given Γ_1^1 the relative rising time remains a constant independently of β. Therefore, choosing $\mathcal{M}_{\text{rot}}$ according to Γ_1^1, we demonstrate that we could simulate the rise of a magnetic flux tube in a realistic regime even though $\beta < 100$. The estimation of the regime allowed us to compare morphologically our results with

the literature. We focused on the path taken by the flux tube and the latitudes of emergence. We have shown that our conclusions agree with former ones and that compressible simulations could reproduce results obtained under the thin flux tube approximation. Finally, we extracted the scaling relation between the relative rise time and the proxy Γ_1^1. We obtained a scale-free relation: $\tilde{\tau}_{\text{rise}} = 2.24\,(\Gamma_1^1)^{-2}$. Again the exponent of the powerlaw agrees with the literature. We also estimated the proportionality factor between the ratio of the main forces and the proxy, based on a morphologic argument, to be about 0.7.

In Chap. 3, we predicted that the axisymmetric behavior of a rising flux tube differs from the non-axisymmetric one. Now that we validated the setup, we move on to the non-axisymmetric case.

5 Extension to 3D

5.1 Introduction

The relative rise time of axisymmetric flux tubes scales with the predicted scaling parameter Γ_1^1, and the axisymmetric setup reproduces similar morphological results as found in the literature. However, according to Fan (2008), the dynamics of a non-axisymmetric rise differs from axisymmetric ones. The extra degree of freedom allows the flux tube to redistribute angular momentum along its own axis; as a result, the flux tube emerges at lower latitude, develops tilt and writhe. In Chap. 3 we have shown that the tension force influences the rise, we predicted that the relative rise time of a non-axisymmetric flux tube scales with a scaling parameter different from Γ_1^1.

In the present chapter, we investigate how non-axisymmetry influences the rise of magnetic flux tubes: we verify that the non-axisymmetric relative rise time $\tilde{\tau}_{\text{rise}}$ scales with the predicted scaling parameter derived in Chap. 3; we study the morphology of the flux tube while rising and compare it to anelastic simulations (Fan 2008; Jouve & Brun 2009; Jouve et al. 2013); finally, we extract the relation between the relative rise time and the regime of the rise. But before going any further, we point out a few numerical differences between the axisymmetric and non-axisymmetric setups.

5.2 Numerical setup: differences to the axisymmetric case

5.2.1 Introducing the concept

We consider a magnetic flux tube situated at the bottom of the convection zone. The magnetic flux tube is perturbed with an azimuthal entropic wave; resulting into a flux tube with alternating sections in *stable equilibrium* and sections in *non-equilibrium*. These sections are distributed in azimuth according to the azimuthal wave number m. The latter aims to represent the most unstable mode of the Parker instability,

but since we skip the destabilization phase, m is chosen arbitrarily. Because the only studies that addressed the formation of magnetic flux tubes from the destabilization of a magnetic layer were done in Cartesian boxes the most unstable mode of the Parker instability is still unknown. Future studies may provide an empirical or analytical value for m.

The symmetry limits the axisymmetric setup to $m = 0$, but the non-axisymmetric setup is not limited. In this chapter we will focus on non-axisymmetric modes ($m > 0$) and particularly on the case $m = 8$. With such a high m, the non-axisymmetric case sufficiently differs from the axisymmetric one to notice the influence of the magnetic tension on the rising magnetic flux tube. In addition, thanks to the periodic boundary conditions in the azimuthal direction, a high m also saves computational time.

In order to verify that the periodic character of the azimuthal boundaries does not influence the results, we carried out non-axisymmetric simulations for $m = 4$ with and without periodic boundaries and find that the results are identical.

For the $m = 8$ case the magnetic flux tube enters the convective zone with 16 alterning sections, 8 in *stable equilibrium*, 8 in *non-equilibrium*. Eventually the rising sections (the apexes) reach the surface and form what we call *active regions*. Suppressing the symmetry property in the non-axisymmetric setups implies modifications. We will now introduce these modifications and discuss the issues they address.

5.2.2 Stable equilibrium and non-equilibrium

Magnetic flux tubes are coherent magnetic structures. The magnetic intensity peaks at the center of the flux tube and decreases outward. Since the magnetic flux tube stays coherent, the thermal pressure force (directed inward) must balance the magnetic pressure force (directed outward). Therefore thermal pressure is reduced inside the magnetic flux tube. The lack of thermal pressure is reflected by density and/or temperature drops inside the flux tube. In Fig. 5.1 we plotted the responses of density and temperature to magnetic pressure. We identify two extreme situations:

- the *isothermal state*, where the temperature difference between the flux tube and its surrounding vanishes, and the lack of pressure is only reflected by a density drop;

- the *neutrally buoyant state*, where the density inside and outside the flux tube equals, and the lack of pressure mirrors only in temperature (“cool flux tube”, see Yoshimura 1985).

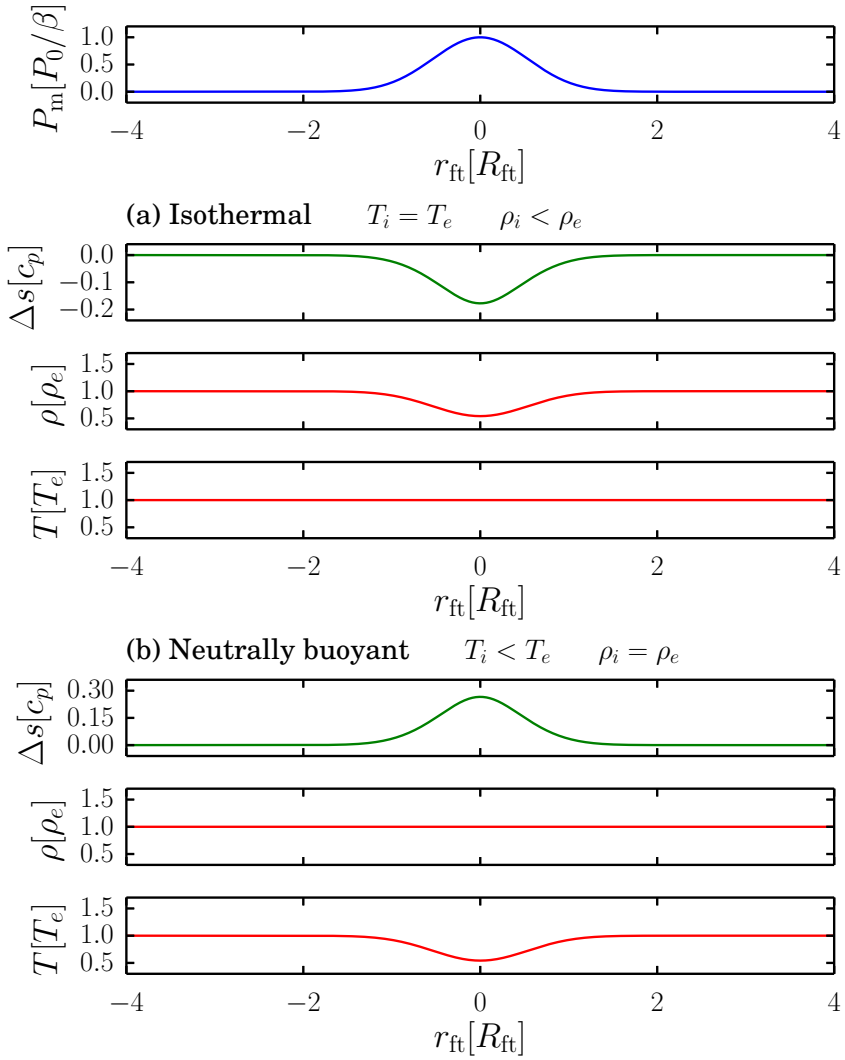

Figure 5.1: Radial profile of the magnetic and thermodynamical quantities in the flux tube frame. The top panel represents the magnetic pressure. The first and the second ensembles of panels, (a) and (b), represent the dimensionless radial profiles of the entropy difference, the density, and the temperature, in an isothermal and neutrally buoyant flux tube, respectively.

In panel (*a*), the *isothermal* state exhibits a negative entropy gradient. A section of a magnetic flux tube in that state is in *non-equilibrium*, it rises. In panel (*b*), the *neutrally buoyant* state exhibits a positive entropy gradient, a section in such a state is in *stable equilibrium* – under the condition that the stellar interior of the setup is adiabatically stratified ($\nabla = 0.4$) –, it remains anchored in the deep interior.

From the thermal states of the flux tube, the wavenumber of the most unstable mode, the EOS and the magnetic profiles, we can characterize the whole flux tube. The magnetic profiles and the EOS are identical to the ones described in Chap. 4, the wavenumber m equals 8, and the azimuthal density profile follows a cosine function which oscillates between an *isothermal* and *neutrally buoyant* state. The azimuthal

density profile reads

$$\rho_{\mathrm{i}}^{(m)} = \rho_{\mathrm{iso}} + \frac{1}{2}\left(\rho_{\mathrm{e}} - \rho_{\mathrm{iso}}\right)\left[1 - \cos(m\phi)\right], \tag{5.1}$$

where the index (m) represents the azimuthal wavenumber of the initial perturbation. ρ_{i}, ρ_{e} and ρ_{iso} represent the density at the center of the flux tube, the density outside the flux tube, and the density inside an *isothermal* flux tube, respectively. This density profile is the generalized form of the density profile presented in Chap. 4, valid for any $m \geq 0$.

It is interesting to remark that according to Weber & Fan (2015) (thin flux tube approximation) the most unstable mode depends on the conduction κ and the sub-adiabaticity ∇. For their initial conditions they have found that both $m = 2$ and $m = 3$ may be the most unstable modes, but it is unclear if this conclusion holds in the general case of solar-like stars.

5.2.3 From 2D to 3D: effects of reducing the resolution

Suppressing the axisymmetry in the setup costs computation time: we resolve the azimuthal direction of the flux tube with 320 grid points. The number of operations per time step increases by about a factor of 320. To save time, we reduce the base resolution by a factor of two, imposing further modifications.

As we discussed in Chap. 2, the top pressure scale height H_{P_0} needs to be resolved with a minimum of ten points So a lower resolution requires to increase the top pressure scale height, leading to a reduction of the density ratio between the top and the bottom of the domain. Resolving H_{P_0} with about 20 grid points, leads to a reduction of the density ratio from 50 (in the 2D case) to 11.

As discussed in Chap. 4, the angular momentum and the magnetic flux should be conserved. To match this constraints, we increased the radius of the flux tube by a factor of 10. Even though the resolution decreases, we resolve the non-axisymmetric flux tube 5 times better than in the axisymmetric case. As a results, the numerical diffusion decreases and allows a better conservation of the flux. Although the drag force is proportional to the radius of the magnetic flux tube, the flux tube remains small compared to the local pressure scale height, and the numerical viscosity is sufficiently low so that the drag force remains negligible in our setup. In any case, the drag force is independent of β and $\mathcal{M}_{\mathrm{rot}}$ and will therefore only impact the proportionality factor k which is not critical for our conclusions.

In addition, because of the larger radius, we had to make sure that the bottom boundary does not alter the initial condition of the magnetic flux tube and therefore we also modify the initial depth at which we insert the magnetic flux tube: from

0.71 to 0.73 solar radii.

Finally, to convince ourselves that the various changes we implemented remain unimportant for the rise, we carried out two axisymmetric simulations with the axisymmetric and the non-axisymmetric resolution, stratification and flux tube radius. We found that the relative rise time, the path and the latitude of emergence change by less than a percent.

We summarize the parameters of the setup in Table 5.1. Note the change of resolution, initial depth, initial radius, pressure scale height, and stratification as compared with the STD-2D setup.

Table 5.1: Parameters for the numerical setup and the initial conditions for the STD-3D case.

Numerical parameters			
Resolution			$[128 \times 256 \times 80]$
AMR levels			2 levels
Effective resolution			$[512 \times 1024 \times 320]$
Domain definitions			
Radial domain		$[R_\star]$	$[0.684 - 0.964]$
Latitudinal domain		$[^\circ]$	$[0 - 81]$
Longitudinal domain		$[^\circ]$	$[0 - 45]$
Flux tubes parameters			
Initial depth:	r_i	$[R_\star]$	0.73
Initial latitude:	θ_i		20°
Initial radius:	R_ft	$[R_\star]$	10^{-2}
Stellar parameters			
Reference radius:	R_0	$[R_\star]$	0.964
Adiabaticity:	∇		0.4
Pressure scale height:	χ		0.04
Stratification:	$\rho_\mathrm{bot}/\rho_\mathrm{top}$		≈ 11

5.3 Verifying the scaling behavior

5.3.1 Parameter study

Following the same method as in Chap. 4, we carry out a parameter study in the (β, $\mathcal{M}_{\mathrm{rot}}$) parameter space. In Fig. 5.2, each point represents a simulation, whose

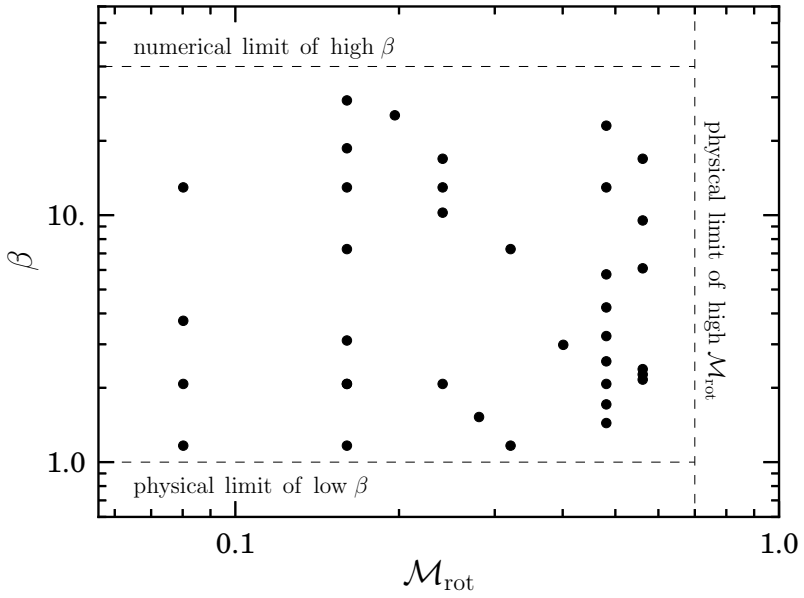

Figure 5.2: Graphical summary of the parameter study. Each symbol represents a simulation. The symbol's coordinates are the input parameter of the corresponding simulation. The exact values can be found in Table A.2. The dashed lines represent the boundaries of the numerical and physical domains, outside of these limits we consider our setup unreliable.

coordinates represent the values of the input parameters. In that case, we cover about one order of magnitude in both directions. The numerical limit of the study (high-β) is reduced compared to the 2D case, owning to the lower resolution to about one half.

5.3.2 Computing the curvature radius $\mathcal{R}$

In Chap. 3, we suggested to carry out simulations to compute the scaling parameter that controls the regime of the rise. We have shown that identifying the regime is a requirement to compare our results with former studies and observations. Our theory suggests that the relative rise time scales with $\Gamma_{\alpha_1}^{\alpha_2}$, where α_1 and α_2 are functions of f_1 and f_2. These exponents parameterize the ansatz (3.8), with f_1 measuring the influence of β and f_2 of $\mathcal{M}_{\mathrm{rot}}$. To extract f_1 and f_2 from the simulations, we need to identify the relation between the curvature radius $\mathcal{R}$, β and $\mathcal{M}_{\mathrm{rot}}$.

There are several ways to compute the curvature radius of an Ω-shaped loop. Here, we present two possible methods: a geometrical method and a mathematical method. It is unclear to us which of the two is the most pertinent. We arbitrarily chose to present here the numerical values of f_1 and f_2 obtained from the geometrical method, but independently of the method, the obtained relations are in qualitative agreement. The mathematical method gives a factor 2 larger values for $\mathcal{R}$, but the sign of the slope of $\mathcal{R}(\beta, \mathcal{M}_{\rm rot})$ remains the same, and the values of f_1 and f_2 differ by less than 0.3%.

With the geometrical method, we select for each simulation the time when the apex reaches 0.85 solar radii. At this time all loops went through the same amount of pressure scale heights and are fully developed. From this state, we select three points: the apex – the point with the largest entropy deficit; and two leg-points, from the leading and the following legs. The leg-points are chosen such that they experience two pressure scale heights less than the apex. These three points define a circle, and we presume that the latter fits the upper part of the loop and that its radius is a good proxy for the curvature radius $\mathcal{R}$.

In Fig. 5.3, we show six examples of circles computed from the geometrical method. The points represent the minimum entropy for each azimuth. Together they represent the line going through the center of the flux tube. The black symbols represent the three selected points that define the dashed circle. Visually the circles fits the upper part of the loop, except in panel (e) and (f). Panel (e) represents the limiting case where we still rely on the result. Panel (f) corresponds to a case where the method clearly fails. Such cases happen when the shape of the flux tube becomes too complex, due to the development of a kink instability, or because deflection becomes so strong that the apex of the loop is not the highest point anymore. In Table A.2, we emphasize the failed cases by italics.

The mathematical method consists in fitting a spline through all the points defining the shape of the magnetic flux tube. From this fit, we extract the parameterized function of the spline, and compute the curvature radius at the apex.

Both methods concord that β and $\mathcal{M}_{\rm rot}$ affect $\mathcal{R}$ with about the same exponent with a slight preference for β: f_1 and f_2 are of the same order of magnitude, with $f_2/f_1 \approx 0.9$.

To compute the numerical values of f_1 and f_2, we use an optimization method: we plot the curvature radii obtained by the geometrical method against $\beta^{f_1}\mathcal{M}_{\rm rot}^{f_2}$ varying f_1 and f_2; and chose the pair that minimizes the residual of a linear fit in log-log space. The result can be seen in Fig. 5.4. We find $f_1 = -0.161$ and $f_2 = -0.145$. These values agree with our predictions: both are negative and less than unity. It indicates that at least the sign predictions made in Chap. 3 were

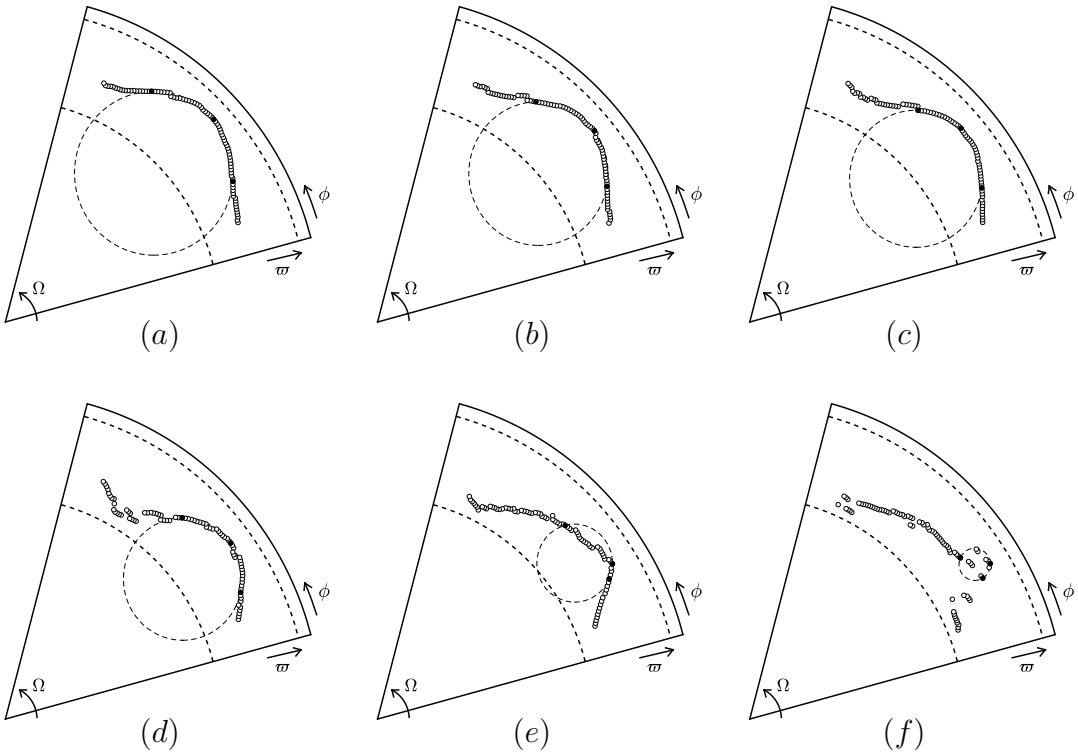

Figure 5.3: Six top-views representing the projection of the magnetic flux tube on a horizontal plane cutting the northern hemisphere of the Sun at $z = 0.34\ R_\star$ (with z being the cylindrical coordinate parallel to the rotation axis). The solid contours represent the physical domains of the stellar wedge. The computational domains are indicated by the thick dashed arcs. Each point represents the projected position of the minimum entropy inside the flux tube for a given meridional plane. We consider that these points build the center-line of the magnetic flux tube. The few black points are the selected points that build the dashed circles, their radii are a proxy for the curvature radii $\mathcal{R}$ of the flux tubes at the apex. We ordered the simulations from large to small radius.

correct.

5.3.3 Computing the scaling parameter $\Gamma_{\alpha_1}^{\alpha_2}$

According to the numerical values of f_1 and f_2 and Eq. (3.11), we can compute $\alpha_1 = 0.793$ and $\alpha_2 = 0.855$. Therefore, the theory (discussed in Chap. 3) predicts that $\Gamma_{0.793}^{0.855}$ should control the regime of the rise of a magnetic flux tube with an azimuthal wavenumber $m = 8$, and thereby that the relative rise time $\tilde{\tau}_{\text{rise}}$ should scale with that parameter.

5.3.4 Verifying the hypothesis with the simulations

In Fig. 5.5 we plot the relative rise time $\tilde{\tau}_{\text{rise}}$ extracted from the simulations against $\Gamma_{0.793}^{0.855}$. The data points align, with a low scatter, to a powerlaw. The low scatter of this plot demonstrates the uniqueness of the relative rise time for a given $\Gamma_{0.793}^{0.855}$,

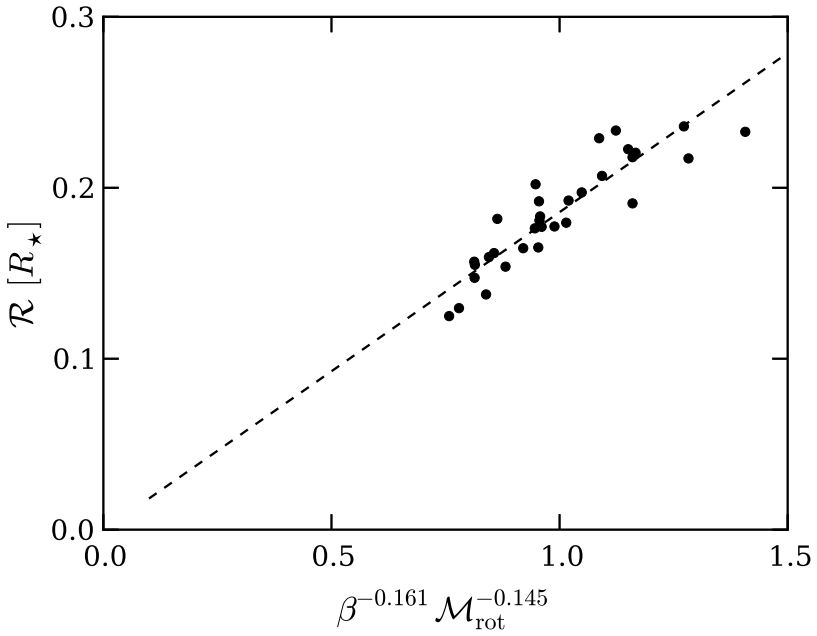

Figure 5.4: Curvature radius, $\mathcal{R}$, of the selected simulations (see Appendix) computed from the geometrical method, over a combination of β and $\mathcal{M}_{\rm rot}$. The dashed line is a least-squares fit of the data points and demonstrates the correlation between $\mathcal{R}$ and $\beta^{-0.161}\,\mathcal{M}_{\rm rot}^{-0.145}$.

that exhibits the scalability of our setup.

The scalability of the setup and the agreement between the numerical and theoretical results have three implications: it allows us to compare our numerical results with observations; it shows the reliability of the method we used to compute the curvature radius; and it validates the hypothesis on which the theoretical predictions were based.

5.4 Discussion on the morphological differences

The latitude of emergence of magnetic flux tubes depends mostly on the initial latitude of the flux tube $\theta_{\rm i}$ and the latitudinal deflection of the magnetic flux tube during its rise. Fan (2008) showed that due to the Ω-shape of the loop a pressure gradient builds between the apex and the feet. This additional force flows mass in the opposite direction than the azimuthal deceleration of the magnetic flux tube, that reduces the angular velocity of the flux tube (see Fan 2008, Fig. 5), and results into a redistribution of angular momentum along the tube's axis. The Coriolis force is reduced accordingly, and the flux tube rises radially. In our simulations, we also find a smaller latitudinal deflection compare to the axisymmetric case As seen in Fig. 5.6, the latitudinal deflection of the flux tube remains close to zero, independently of the regime. In comparison, in the 2D case, the latitudinal deflections were up to 25° for

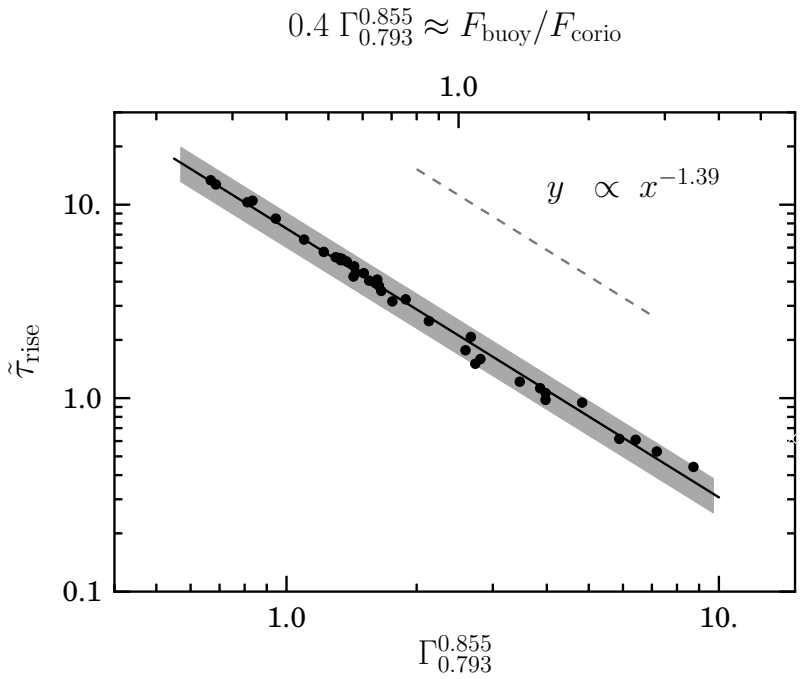

Figure 5.5: Relative rise time, $\tilde{\tau}_{\rm rise}$ versus the scaling parameter $\Gamma_{0.793}^{0.855}$. The solid line is a least-squares fit of the data points. The dashed line indicates a power of -1.39. On the upper axis, we indicate the corresponding $0.4\ \Gamma_{0.793}^{0.855}$ values that are the closest estimates of $F_{\rm buoy}/F_{\rm corio}$ we could extract from our simulations. The grey zone gives an idea of the scatter.

rotation dominated rises.

The tilt angle of emerging regions has been extensively discussed in the literature and our study would be incomplete without mentioning it. Unfortunately, the tilt angles obtained from our numerical experiments can not be directly compared to the ones found in the literature. The tilt angles visible at the solar surface are supposed to be the results of the combined effect of the initial twist and of the wirth due to the Coriolis effect. But due to the high initial twist all our simulations are kink unstable; the kink instability leads to strong wirth that enhance the final tilt angles to unrealistic values. In most of the presented experiments the ratio of the rise time over the time scale of the kink instability is of the order of unity. For the few experiments where the ratio is sufficiently large to ignore the effect of the kink on the wirth, the tilt angles qualitatively agree with former studies; the tilt has the correct sign and decreases for stronger flux tubes. Moreover, the relative rise time remains constant independently of the importance of the kink instability.

In 3D cases, there is one further morphological property that may be addressed: the azimuthal deflection of the apex of the magnetic flux tube. As seen in Fig. 5.7, the azimuthal deflection depends on the regime, the more it tends toward *rotation*

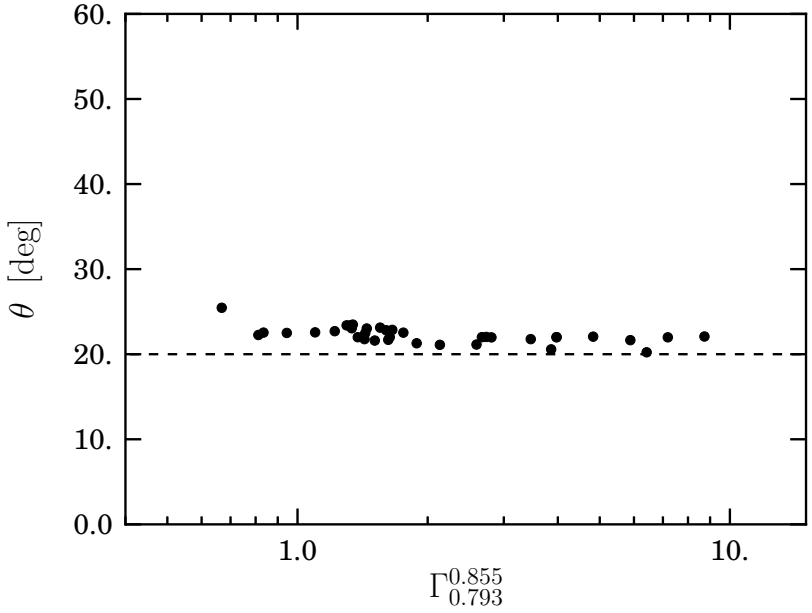

Figure 5.6: Emergence latitude, θ, of the magnetic flux tube against the scaling parameter $\Gamma_{0.793}^{0.855}$. The dashed line indicates the initial latitude where we inject the magnetic flux tube.

dominated one, the more the apex deflects in the azimuthal direction. Furthermore,

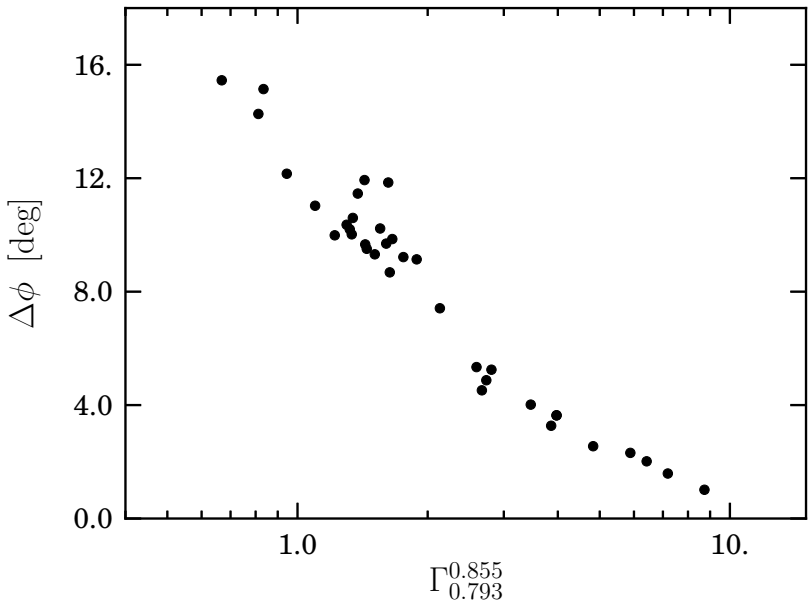

Figure 5.7: Azimuthal deflection, $\Delta\phi$, of the apex of the magnetic loop when it reaches the top of the domain, against the scaling parameter $\Gamma_{0.793}^{0.855}$.

Jouve et al. (2013) have shown that the asymmetry of the Ω-loop increases with the azimuthal deflection. We also find that effect as illustrated in Fig. 5.8. The panels

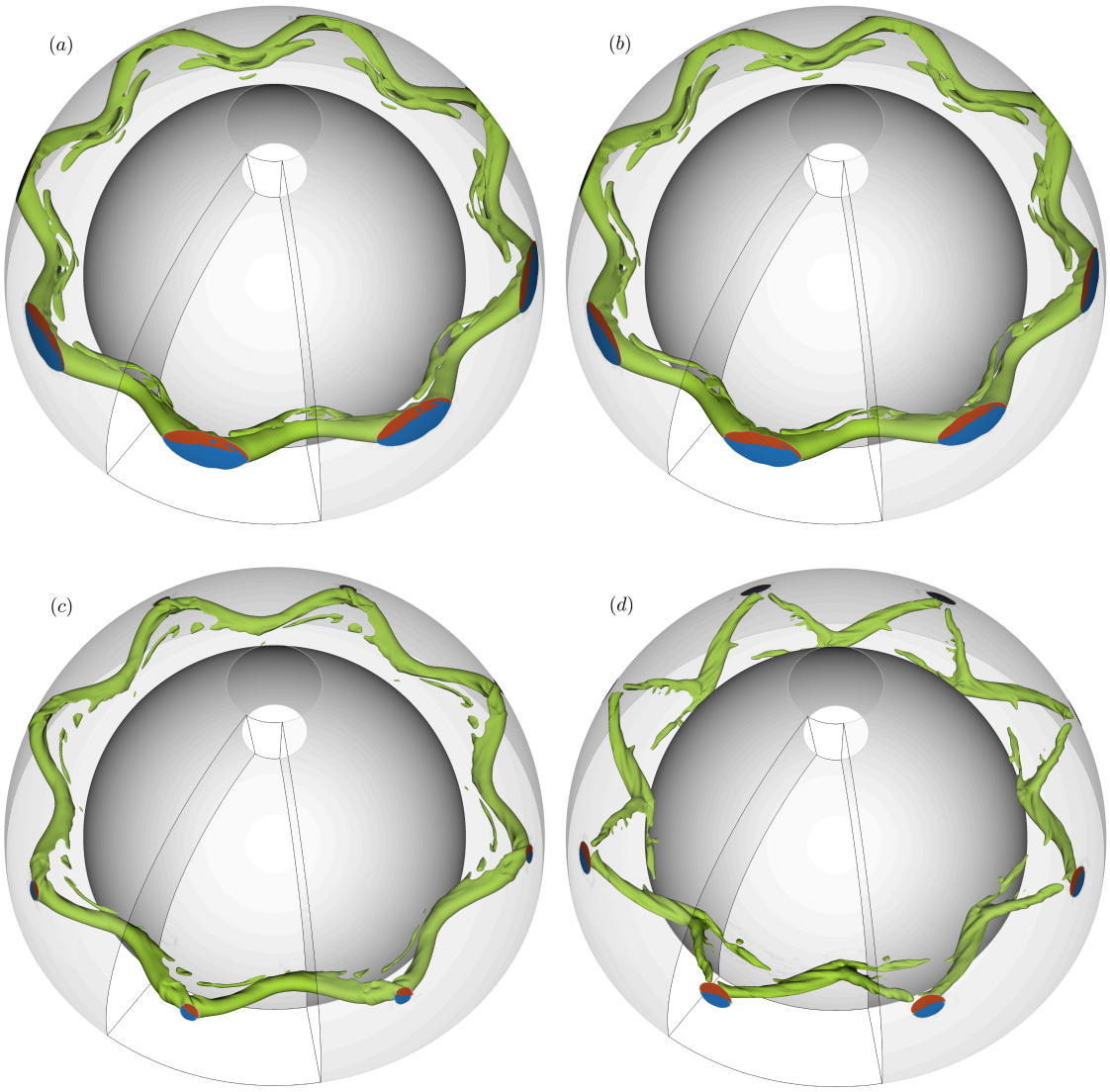

Figure 5.8: Snapshot of four representative simulations ordered from a *buoyancy dominated* regime (high $\Gamma_{0.793}^{0.855}$) to a *rotation dominated* regime (low $\Gamma_{0.793}^{0.855}$). The transparent half-sphere represents the reconstructed simulated domain, where the real domain is indicated by the solid wedge-shape. The green contour represents the magnetic pressure where it reaches about 10% of the maximum. The red (blue) surfaces represent the positive (negative) radial component of the magnetic flux density emerging at the top of the domain. The input parameters of these simulations can be found in Table A.2, referred with their respective labels.

(a), (b), (c) and (d) are ordered by decreasing $\Gamma_{0.793}^{0.855}$, i.e. increasing influence of rotation. In a *buoyancy dominated* regime, the loop rises fast as a wide, symmetric Ω-shaped loop (a). In a *rotation dominated* regime, the flux tube rises slowly as a narrow, asymmetric loop (d).

In summary, our non-axisymmetric simulations reproduce the same morphologic characteristics as found in the literature: there is nearly no latitudinal deflection of the apex; the azimuthal deflection and the asymmetry of the legs both increase with

the rotational character of the regime.

5.5 Extracting the scaling relation between the relative rise time and the regime

We verified that $\Gamma^{0.855}_{0.795}$ controls the regime of the rise for $m = 8$, and that the results agree qualitatively with the literature. We now focus on the relative rise time $\tilde{\tau}_{\rm rise}$. From Fig. 5.5, we obtain a powerlaw and extract the following relation

$$\tilde{\tau}_{\rm rise} = 7.53 \left(\Gamma^{0.855}_{0.793}\right)^{-1.39} \tag{5.2}$$

As in the axisymmetric case, in non-axisymmetric simulations, the relative rise time follows a negative power of the scaling parameter, but with a different exponent – called α_3 – of about -1.4.

Because $\Gamma^{0.855}_{0.795}$ is just a proxy for the force ratio, we need to find the *balanced regime* to determine the unknown k. As in Chap. 4 we can use a morphological argument to estimate the proportionality factor between the force ratio and the proxy. Panel (c) of Fig. 5.8 illustrates the minimum $\Gamma^{0.855}_{0.795}$ showing an asymmetry. We consider this magnetic flux tube rising in the *balanced* regime. The value of $\Gamma^{0.855}_{0.795}$ is 2.5, the proportionality factor is therefore about 0.4. We indicate $0.4\,\Gamma^{0.855}_{0.795}$ on the upper axis of Fig. 5.5 which represents the closest estimate we have for $F_{\rm buoy}/F_{\rm corio}$.

Considering the estimate of k to be valid, Fig. 5.9 shows that the power laws relating $\tilde{\tau}_{\rm rise}$ and $F_{\rm buoy}/F_{\rm corio}$ for the $m = 0$ and $m = 8$ cases, cross each other for $F_{\rm buoy}/F_{\rm corio} \approx 0.33$. So for a given regime, when $F_{\rm buoy}/F_{\rm corio}$ exceeds 0.33, non-axisymmetric flux tubes rise more slowly than axisymmetric ones, whereas when $F_{\rm buoy}/F_{\rm corio} < 0.33$ the situation inverses.

However, Fig. 5.9 also shows that for a given star (a given $\mathcal{M}_{\rm rot}$) and a given magnetic flux density (a fixed β) magnetic flux tubes do not necessarily rise in the same regime. For instance in the solar case, assuming flux tubes with a magnetic flux density larger than 600kG, the higher the azimuthal wave number of the flux tube, the more the regime tends toward *buoyancy dominated*.

Furthermore, as underlined by Fan (2008), in the solar case (e.g. $\mathcal{M}_{\rm rot} = 6 \cdot 10^{-3}$) weak magnetic flux tubes rise faster for $m = 8$ than for $m = 0$. But this conclusion does not hold for the general case. Fig. 5.9 shows indeed that for magnetic flux densities larger than 200 kG the situation inverses and axisymmetric flux tubes rise faster than the non-axisymmetric ones. Again the characteristics of the rise depend on the regime. For *buoyantly dominated* rises, the paths taken by flux

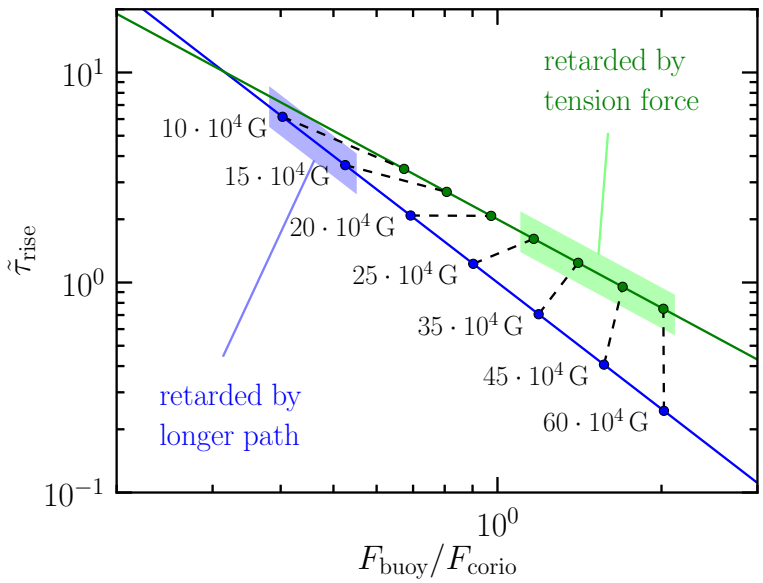

Figure 5.9: Relative rise time, $\tilde{\tau}_{\mathrm{rise}}$, versus the force ratio defining the regime of the rise. It should be noticed that $F_{\mathrm{buoy}}/F_{\mathrm{corio}}$ is a result of rotation and the rise velocity, and therefore of the tension force. The blue and the green solid lines are powerlaws with exponents -2 and -1.4, respectively, and represent the relations we obtained for axisymmetric and non-axisymmetric flux tubes. Both relations are valid for any solar-like star, but the green and blue symbols with actual values are computed for the solar case, for various magnetic flux densities, with $\mathcal{M}_{\mathrm{rot}} = 6 \cdot 10^{-3}$. The colored areas indicate the causes for the longer relative rise times.

tubes are in both cases almost radial, therefore the difference in the relative rise time arises exclusively from the tension force, which reduces the rise velocity of non-axisymmetric rising flux tubes (green area in Fig. 5.9). On the contrary, in the *rotation dominated* regime, the longer relative rise time of axisymmetric flux tubes results from their latitudinal deflection, leading to longer paths (blue area in Fig. 5.9).

Finally, Eq. (5.2) shows that the exponent of the powerlaw decreases compared to axisymmetric simulations. This decrease is out of the scope of the theory described in Chap. 3, but we can suggest an interpretation. The pressure gradient along the tube is the only ingredient that is independent of the regime (it only depends on the stratification) and is present in the non-axisymmetric case and absent in the symmetric one. In the case of an axisymmetric simulation the longer path taken by the flux tube causes the difference in relative rise time between a *rotation dominated* and a *buoyant dominated* regime. In the non-axisymmetric simulations the difference between the paths reduces through a weaker deceleration of the azimuthal velocity. We suggest that the pressure gradient, which imposes a more radial path to the

flux tube, reduces the exponent of the powerlaw α_3. Such an explanation implies that $m = 4$ simulations should exhibit an exponent α_3 between -2 and -1.4, which would agree with the exponent found by Moreno-Insertis (1986) where the author found -1.8. This may be explored by further series varying m, which could lead to a general function for $\alpha_3(m)$. This will allow us to predict the relative rise time of a magnetic flux tube depending on the characteristics of the star and the large-scale magnetic field.

5.6 Summary and discussion on the limits

Along this chapter, we investigated the impact of non-axisymmetry on the rise of magnetic flux tubes. We first discussed the differences we had to introduce in the numerical setup to reduce the computational time in order to achieve a parameter study: we reduced the resolution and the density ratio between top and bottom of the numerical domain, and we increased the radius of the magnetic flux tube. We also introduced the initial condition of the non-axisymmetric setup. The magnetic flux tube is injected at the bottom of the convective zone alternating between two thermal states – *isothermal* and *neutrally buoyant* – with a wavenumber of $m = 8$.

Then we verified the scalability of the setup by carrying out a parameter study. We first had to compute the predicted scaling parameter (see Chap. 3), by measuring the curvature radius $\mathcal{R}$ of the magnetic flux tube. We introduced two methods to compute $\mathcal{R}$, and discussed the results of the geometrical one. We could extract α_1 and α_2 and compute the theoretical scaling parameter $\Gamma^{0.855}_{0.793}$. Afterward we could verify that the setup does indeed scale with the latter. We showed the uniqueness of the relative rise time for a given $\Gamma^{0.855}_{0.793}$. The uniqueness of $\tilde{\tau}_{\text{rise}}$ confirms the scalability of our setup and justifies the assumptions of our theory.

Then, we discussed the morphological behavior of the rise of the magnetic flux tube and qualitatively compared it with former anelastic results. We found that both agree, justifying the use of the anelastic approximation in solar-like stars for the study of magnetic flux tubes.

Finally we focused on our main interest – the relative rise time – and extract a relation between the latter and $\Gamma^{0.855}_{0.793}$. We found that the powerlaw that the relative rise time follows has a exponent of -1.4, which is shallower than the exponent of -2 found in the axisymmetric case. We suggested that this reduction results from the radial paths of non-axisymmetric rises. We also found that the scaling parameter is limited in predicting the *balanced regime*. So we followed a morphological argument and found that the proportionality factor between the force ratio and the proxy approaches 0.4.

A few issues need to be discussed, however. First, the method we used to compute $\mathcal{R}$ may be criticized and improved. But we have shown that it delivers the expected sign for the trend of $\mathcal{R}(\beta, \mathcal{M}_{\rm rot})$, and provides values for f_1 and f_2 that lead to a $\Gamma_{\alpha_1}^{\alpha_2}$ which indeed controls the regime of the rise; as we have predicted in Chap. 3.

We may also criticize the absence of convective motions, differential rotation, and meridional circulations in our setup. These ingredients surely impact the rise of the magnetic flux tube. But as we mentioned in the first chapter, simulating compressible rising flux tubes in rotating convective environments is still far beyond the computational limits of the current massively parallel computing.

Finally, we suggest to carry out further series to extract a relation between α_3 and the wavenumber m. This function – combined with the dependence of the most unstable mode of the Parker instability on the strength of the magnetic flux tubes – will allow us to predict the rise time of magnetic flux tubes through the stellar activity cycle. But the conclusions of the present chapter already incite us to investigate the impact of α_3 on a delayed Babcock-Leighton dynamo. In the next chapter, we will discuss and present results on these matters.

6 Application to stellar objects

6.1 Introduction

This chapter aims to apply the scaling law we obtained from direct numerical simulations to a dynamo model for the large-scale magnetic field.

The scaling relation we have found has the great advantage, that it applies to any star that meets the requirements of our scenario. The latter assumes the presence of magnetic flux tubes, – and therefore requires a tachocline – and a convective envelope that spans over about one third of the stellar radius. Main-sequence solar-like stars meet those requirements. We consider that our scaling law applies to solar-like stars from the zero-age main sequence to the late main sequence.

The scaling law relates the relative rise time of a magnetic flux tube $\tilde{\tau}_{\rm rise}$ to the parameters of its stellar host β and $\mathcal{M}_{\rm rot}$. We found that both the regime of the rise (controlled by $\Gamma_{\alpha_1}^{\alpha_2}$) and the exponent of the scaling relation α_3 depend on the azimuthal wave number of the Ω-shaped loop m.

In this chapter, we focus on the particular flux transport dynamo that we call the *flux tube/Babcock-Leighton dynamo*. Similar to Jouve et al. (2010), we implement this dynamo in a different manner than the traditional version. We consider that the rise time of magnetic flux tubes is not negligible compared to the magnetic cycle. We modify the *flux tube/Babcock-Leighton dynamo* by introducing a delay in the term mimicking the emergence of active regions and being responsible for the regeneration of the dipolar field (the *Babcock-Leighton effect*). We constrain that delay with the universal scaling law (Eq. 6.5) we have found and study its impact on the dynamo solutions.

Before discussing these results, we suggest to explore the meaning of our former conclusions for the rise time of magnetic flux tubes in solar-like stars.

6.2 Determining the rise time of magnetic flux tubes in solar-like stars

6.2.1 Rotation-activity diagram

Nowadays, astronomers have the opportunity to observe stellar activity, e.g. by measuring the ratio of X-ray luminosity over the total bolometric luminosity, $R_{\mathrm{X}} = L_{\mathrm{X}}/L_{\mathrm{bol}}$. It has been empirically shown that the relative X-ray luminosity of the Sun is a good proxy for the magnetic flux density in the corona (e.g. Preminger et al. 2010). This ratio is therefore considered as a proxy for the magnetic stellar activity. The level of stellar activity exhibits two branches: the slow, and the fast rotation branch. Stellar activity on the slowly rotating branch depends on the rotation period, whereas on the fast rotating branch, activity seems to be independent of rotation (Strassmeier et al. 1994; Saar 2002; Böhm-Vitense 2007; Barnes & Kim 2010; Wright et al. 2013; Reiners et al. 2014). The corresponding results by Wright et al. (2013) are reproduced in Fig. 6.1. It can be underlined that the $R_X - \mathrm{Ro}$ relation

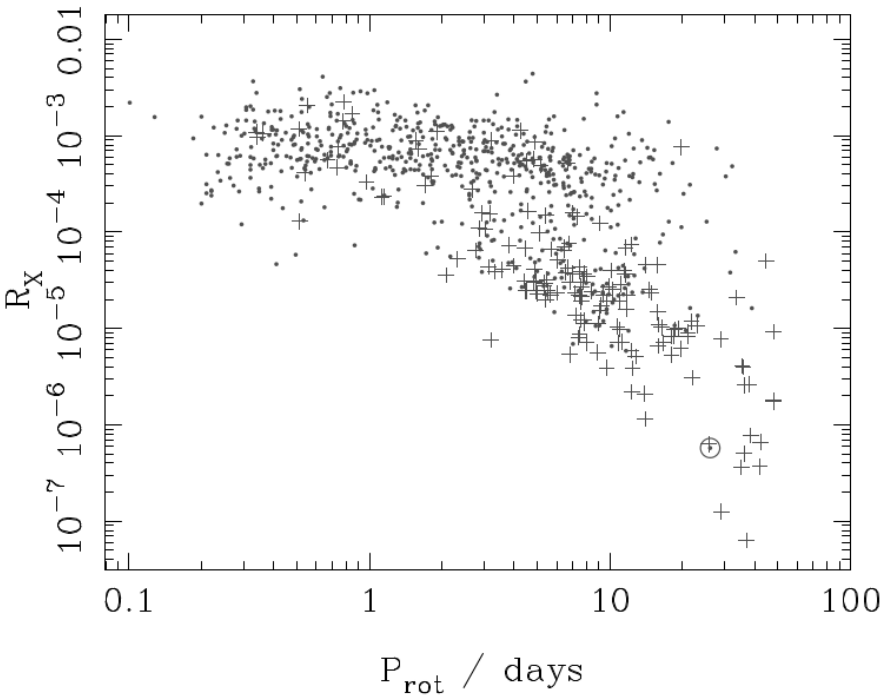

Figure 6.1: Left-panel of Fig. 1 from Wright et al. (2013) (adapted). The stellar sample presented in Wright et al. (2011) includes 824 late-type stars. The plus symbols identify binaries and the Sun is indicated by the solar symbol. $R_{\mathrm{X}} = L_{\mathrm{X}}/L_{\mathrm{bol}}$.

exhibits a lower scatter than the $R_X - P_{\mathrm{rot}}$ relation shown in Fig. 6.1. However, the Rossby number Ro ($= P_{\mathrm{rot}}/\tau_{\mathrm{conv}}$) requires the convective turn overtime τ_{conv} which is a weakly constrained quantity and not directly accessible from observations. We

prefer to concentrate on a relation involving fewer unknowns.

We first focus on the slowly rotating branch. The latter shows an inverse square relation with rotation:

$$\frac{L_{\rm X}}{L_{\rm bol}} \propto P_{\rm rot}^{-2}. \tag{6.1}$$

In Vidotto et al. (2014), the authors suggest a relation between activity and the large-scale dipolar field (their Fig. 6). They found the following relation:

$$\frac{L_{\rm X}}{L_{\rm bol}} \propto \langle |B_{\rm v}| \rangle^{1.6}, \tag{6.2}$$

where $\langle |B_{\rm v}| \rangle$ is the average vertical magnetic field over the full stellar surface. We assume that it represents a proxy for the stellar dipolar field $B_{\rm dip}$. Combining Eqs. (6.1) and (6.2), we obtain a relation between the dipolar field and the stellar rotation for the slowly rotating branch:

$$B_{\rm dip} \propto P_{\rm rot}^{-1.25} \tag{6.3}$$

For the fast rotating branch, the exponent approaches zero, therefore the dipolar field depends weakly on rotation: $B_{\rm dip} \approx$ const.

6.2.2 From dipolar field to flux tubes

So far, we considered that flux tubes form from the toroidal magnetic field at the bottom of the convective zone. In flux transport dynamos the toroidal magnetic field is maintained by the winding up of the large-scale poloidal field by differential rotation: the shear, taking place predominantly at the bottom of the convection zone, generates toroidal magnetic flux. We can reasonably suppose that this field is proportional to the large-scale dipolar field, with a dependence on the shear due to differential rotation. Küker & Rüdiger (2011) have shown that the mean-field theory of the λ-effect predicts that the absolute differential rotation is nearly independent of rotation. This prediction has been confirmed by observations (Reinhold et al. 2013), but exhibits a large observational scatter. We follow the conclusion of Küker & Rüdiger (2011) and presume that the shear at the bottom of the convective zone is independent of rotation. We can relate the dipolar field to the strength of the magnetic flux tubes: $B_0 \propto B_{\rm dip}$.

This path of thought allows us to relate the strength of the magnetic flux tube to the rotation period:

$$B_0 \propto P_{\rm rot}^{-1.25}. \tag{6.4}$$

This relation is valid for the slowly rotating branch. It tells us that the slower the

star rotates, the weaker are the magnetic flux tubes forming at its tachocline.

Following the same argumentation for the fast rotating branch, we find a constant magnetic flux density independent of stellar rotation: $B_0 = \text{const}$.

6.2.3 Impact on the scaling

The main conclusion of our work is the scaling relation between the relative rise time and the regime of the rise. We found that

$$\tilde{\tau}_{\text{rise}} \propto \left(\Gamma_{\alpha_1}^{\alpha_2}\right)^{\alpha_3}, \tag{6.5}$$

where $\Gamma_{\alpha_1}^{\alpha_2}$ is defined in Eq. (3.10); and where α_1, α_2 and α_3 depend on the azimuthal wave number of the initial perturbation m. For a given stellar structure, ϖ as well as c_s are constant, and v_A depends exclusively on B_0, as a result we can simplify Eq. (3.10):

$$\Gamma_{\alpha_1}^{\alpha_2} \propto \left(\frac{B_0^{\alpha_1}}{\Omega}\right)^{\alpha_2}. \tag{6.6}$$

Now, combining Eqs. (6.5) and (6.6) and replacing B_0 by its equivalent for the slowly rotating branch (cf. Eq. 6.4), we can write:

$$\tilde{\tau}_{\text{rise}}^{(m)} \propto P_{\text{rot}}^{[\alpha_3\alpha_2(1-1.25\alpha_1)]} \tag{6.7}$$

In the $m = 8$ case, $\alpha_1 = 0.793$, $\alpha_2 = 0.855$ and $\alpha_3 = -1.4$. We find $\alpha_3\alpha_2(1 - 1.25\alpha_1) \approx -0.014$. For the $m = 0$ case, $\alpha_1 = \alpha_2 = 1$, and $\alpha_3 = -2$: the exponent equals 0.5. So it seems that in the extreme cases of $m = 0$ on the one hand, and of $m = 8$ on the other hand, the relative rise time does not depend much on rotation for slowly rotating stars.

In the fast rotating branch the situation is different. Observations indicate that B_0 is independent of rotation, hence Eq. (6.6) implies:

$$\Gamma_{\alpha_1}^{\alpha_2} \propto P_{\text{rot}}^{\alpha_2} \tag{6.8}$$

The relative rise time becomes a function of rotation:

$$\tilde{\tau}_{\text{rise}}^{(m)} \propto P_{\text{rot.}}^{\alpha_2\alpha_3} \tag{6.9}$$

with $\alpha_2\alpha_3$ varying between -2 and -1.2 for $m = 0$ and $m = 8$, respectively. So in fast rotating stars, it seems that the relative rise time depends strongly on rotation.

But these relations are incomplete, we can extract their trend, but we miss a point of reference to fix the curves. We suggest to use the solar value as a reference.

In Weber et al. (2011), the authors find that a flux tube of 10^5G perturbed with an $m = 2$ azimuthal wave number rises about 40 days that is about 1.5 rotation period. We can reasonably assume that the corresponding $m = 0$ $\tilde{\tau}_{\rm rise}$ is about unity. Note that 10^5 G is about $5/3\,B_{\rm eq}$ (cf. Section 4.1 of Jouve & Brun (2009) giving $B_{\rm eq} \approx 60$ kG)

If we consider that a magnetic flux tube rises in the same regime for the $m = 0$ and the $m = 8$ cases then $0.7\,\Gamma_1^1 = 0.4\,\Gamma_{0.793}^{0.855}$ (cf. Chaps. 4 and 5). In Fig. 4.5, a relative rise time of $\tilde{\tau}_{\rm rise}^{(0)} = 1$ corresponds to a regime $0.7\,\Gamma_1^1$ about unity. For the same regime in the $m = 8$ case ($0.4\,\Gamma_{0.793}^{0.855} = 1$) we can read in Fig. 5.5 that the relative rise time $\tilde{\tau}_{\rm rise}^{(8)} \approx 2$. From the scaling relation we compute the corresponding relative rise time for an equipartition flux tube: $\tilde{\tau}_{\rm rise}^{(m)}(B_{\rm eq}) = \tilde{\tau}_{\rm rise}^{(m)}(B_0)\ (3/5)^{\alpha_1\alpha_2\alpha_3}$. By continuity, we construct the functions $\tau_{\rm rise}^{(m)}(B_{\rm eq})$ against $P_{\rm rot}$ for both branches, taking as reference points

$$\tau_{\rm rise}^{(0)}(B_{\rm eq}) = 74.8 \text{ d},$$
$$\tau_{\rm rise}^{(8)}(B_{\rm eq}) = 108.5 \text{ d}.$$

Fig. 6.2 shows a comparison of the observed magnetic cycle – as a function of stellar rotation – with the rise time of various magnetic flux tubes. The red lines correspond to fits from Saar (2002, see left-panel of his Fig. 3). They represent the dependence of the magnetic cycle on stellar rotation for the three activity branches: *inactive*, *active*, and *super-active*. We plotted in green and blue the upper limits for the rise time of magnetic flux tubes for $m = 0$ and $m = 8$. For these upper limits the proportionality factor relating B_0 and $P_{\rm rot}$ are chosen such that, for a given rotation period, the predicted rise time is of the same order of magnitude as the stellar cycle. The corresponding values of B_0 are 25% and 8% of $B_{\rm eq}$, respectively. So Fig. 6.2 illustrates that, for stars of rotation periods ranging between 5 and 50 days, any magnetic flux tube with a magnetic flux density lower than 25% (8%) of the equipartition value $B_{\rm eq}$, will lead to a rise time longer than the cycle period. This statement contradicts the general paradigm of standard *flux tube/Babcock-Leighton dynamos*, which assume the rise of magnetic flux tubes to be instantaneous.

An open question remains: are these flux tubes sufficiently buoyant to reach the surface without being destroyed by the convective motions?

This issue has been addressed by several authors (Fan et al. 2003; Murray et al. 2006) and it seems clear that isothermal magnetic flux tubes need to be in superequipartition with the convective flows to ignore the effect of convection. Jouve & Brun (2009) suggested a minimum field of $3\,B_{\rm eq}$. However, weaker magnetic flux tubes may still reach the surface. Thin flux tube simulations (Weber et al. 2011)

have shown that magnetic flux tubes with magnetic flux densities of $0.3\,B_{\rm eq}$ (40 kG in that paper) still reproduce solar-like characteristics. Additionally, convection may also positively contribute to the rise, and magnetic flux tubes may also form within the convective zone (Nelson et al. 2014). In such a case flux tubes as low as 2% of $B_{\rm eq}$ have been shown to reach the surface. Therefore, we would like to consider the possibility that subequipartition flux tubes with say $B_0 \gtrsim 0.1 B_{\rm eq}$ may still participate to the dynamo mechanism.

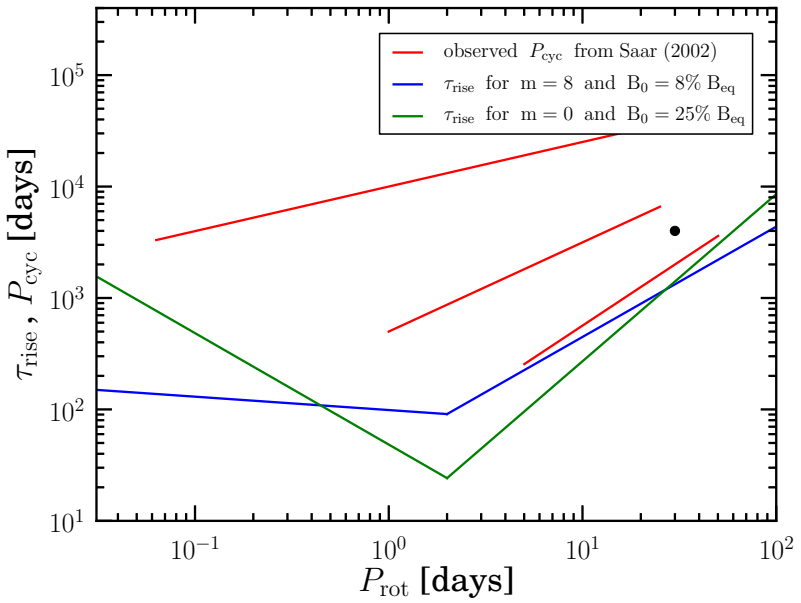

Figure 6.2: Observed magnetic cycles, $P_{\rm cyc}$, and theoretical rise time, $\tau_{\rm rise}$, plotted against rotation period. The red lines are fits to observational data from Saar (2002), for the *inactive* (lowest), *active* (middle), and *super-active* (uppermost red line) branches (cf. their Fig. 3). The green (blue) line represents the rise time of a magnetic flux tube with a magnetic flux density of $25\%\,B_{\rm eq}$ ($8\%\,B_{\rm eq}$) as a function of various rotation periods, for $m = 0$ ($m = 8$). The black dot represents the magnetic cycle of the Sun.

6.2.4 Conclusions

We used observations to illustrate the implications of our theory. We have shown that it could lead to situations where the rise of magnetic flux tubes may become a significant fraction of the cycle period, at least for *inactive* stars.

But Fig. 6.2 raises several questions: what happened to the dynamo mechanism when the majority of the magnetic flux tubes are so weak that they need a full stellar cycle to reach the surface? Can the Babcock-Leighton dynamo survive?

In order to answer these questions and to make predictions on observations, we need to introduce the scaling law obtained in the previous sections into a *flux*

tube/Babcock-Leighton dynamo and study how the magnetic cycle reacts when it experiences the various constraints the scaling law imposes.

6.3 Delayed Babcock-Leighton Dynamo

In the frame of a *flux tube/Babcock-Leighton dynamo*, the Ω-effect operates at the bottom of the convection zone, where it generates toroidal magnetic field. The reversal of the poloidal field results from the *Babcock-Leighton effect*, that accounts for a series of processes taking place at the surface. These processes are the cancelation of magnetic flux due to magnetic reconnection, the diffusion of magnetic flux because of the strong mixing of turbulence, and the advection of magnetic flux toward the poles resulting from the combined effect of the random walk of granulation and the meridional circulation. Applied to the magnetic flux of tilted active regions, the remaning net poloidal magnetic flux cancels with the polar magnetic field and produces the reversal.

The drivers of the dynamo mechanism namely the Ω-effect and the *Babcock-Leighton effect* are located at two different places. But how active regions can form at the surface from the toroidal magnetc field generated at the bottom of the convection zone? The buoyant rise of magnetic flux tubes is responsible for the transport and the Coriolis effect for the tilt of the emerging magnetic flux.

The toroidal magnetic flux sitting at the bottom of the convective zone varies, throughout the stellar magnetic cycle. Traditionally, it is considered that the time scale of the variation of toroidal magnetic flux lasts much longer than the rise time of a magnetic flux tube ($P_{\mathrm{cyc.}} \gg \tau_{\mathrm{rise}}$). The rise time is considered instantaneous, and the *Babcock-Leighton effect* applies to the toroidal magnetic flux at the emerging time ($t = t_{\mathrm{emerg}}$). But as seen in Fig. 6.2, for a reasonable range of magnetic flux densities the rise time of magnetic flux tubes lasts for a significant fraction of the stellar magnetic cycle. For these magnetic flux densities the instantaneous treatment of the rise time is not valid anymore. In order to account for the rise time, we design a *delayed flux tube/Babcock-Leighton dynamo*, where the *Babcock-Leighton effect* applies to the magnetic flux at a time $t = t_{\mathrm{emerg}} - \tau_{\mathrm{rise}}$. We constrain τ_{rise} with the scaling law we obtained from our direct numerical simulations.

6.3.1 The numerical setup of a delayed Babcock-Leighton dynamo

There are several ways to design a mean-field *Babcock-Leighton dynamo*. We chose to simplify the setup as much as possible. We consider that the molecular magnetic

diffusion is small compared to the turbulent magnetic diffusion: $\eta \ll \eta_t$. We suppose that turbulence is homogeneous in the stellar interior and fix η_t to a constant value. In order to non-dimensionalize the system, we set $R_\star$ (the stellar radius), $\tau_{\text{diff}} = R_\star^2/\eta_t$ (the diffusion time), and $B_{\text{eq}} = u_{\text{conv}}\sqrt{\rho\mu_0}$ (the magnetic flux density in equipartition with convective motion, u_{conv}) as the "typical" length, time scale and magnetic flux density of the system.

Considering these assumptions and this unit system, we can solve the reduced mean-field induction equations thanks to the pseudo-spectral code developed by Rainer Hollerbach, see Hollerbach (2000) for more details.

We solve the following dimensionless mean-field formulation of the *Babcock-Leighton dynamo*:

$$\begin{aligned}
\partial_t B_\phi &= \left(\nabla^2 - \frac{1}{\varpi^2}\right) B_\phi \\
&\quad - \text{Re}\, \varpi \mathbf{u}_\text{P} \cdot \nabla \left(\frac{B_\phi}{\varpi}\right) - \text{Re}\, B_\phi \nabla \cdot \mathbf{u}_\text{P} \\
&\quad + C_\Omega\, \varpi\, [\nabla \times (\varpi A_\phi \mathbf{e}_\phi)] \cdot \nabla(\Omega), \\
\partial_t A_\phi &= \left(\nabla^2 - \frac{1}{\varpi^2}\right) A_\phi \\
&\quad - \text{Re}\, \frac{\mathbf{u}_\text{P}}{\varpi} \cdot \nabla(\varpi A_\phi) + C_S S,
\end{aligned} \tag{6.10}$$

where, B_ϕ, $\mathbf{u}_\text{P}$, ϖ, A_ϕ, Ω and S are the azimuthal component of the magnetic field, the meridional circulation, the cylindrical radius, the azimuthal magnetic potential, the angular velocity, and the source term of the Babcock-Leighton effect, respectively. Furthermore, the ∇ operators are in spherical coordinates. Three dimensionless parameters control the system: the Reynolds numbers of the meridional flow Re and of the rotation C_Ω and the dynamo number C_S are defined as follows,

$$\text{Re} = \frac{u_0 R_\star}{\eta_t}\ ;\ C_\Omega = \frac{\Omega_0 R_\star^2}{\eta_t}\ ;\ C_S = \frac{S_0 R_\star}{\eta_t}\ , \tag{6.11}$$

where u_0, Ω_0, and S_0 are the "typical" strength of the meridional circulation, the angular velocity, and the Babcock-Leighton source term, respectively. The profiles of $\mathbf{u}_\text{P}$ and Ω normalized by u_0 and Ω_0 are shown on Fig. 6.3. These profiles are obtained from computations from Manfred Küker, where he solved the average angular momentum and temperature equations, closed with the λ-effect (Küker & Rüdiger 2011). So in the frame of the λ-effect theory (Rüdiger 1989) the differential rotation and the meridional circulation are consistent with each other.

The last missing ingredient in our setup is the meridional profile of the Babcock-

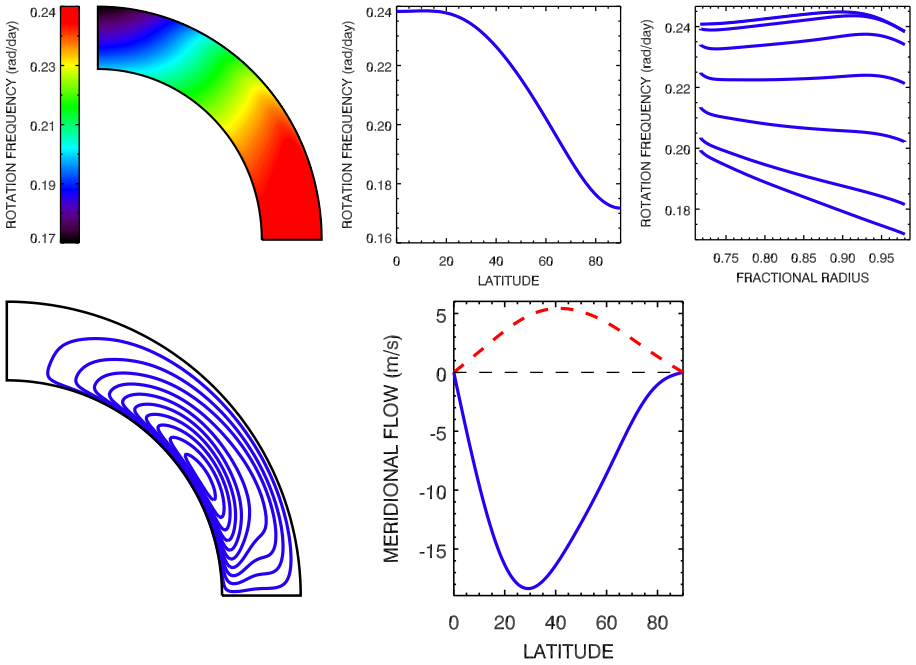

Figure 6.3: From Küker & Rüdiger (2011), solar-like differential rotation profile and meridional circulation obtained from λ-effect solutions.

Leighton source term. In order to obtain finite solutions of the mean-field induction equations, the the source term needs to be quenched by some non-linear mechanism. In the present scenario the quenching arises from the low tilt of strong magnetic flux tubes. In the *buoyancy dominated* regime the effect of rotation is small, magnetic flux tubes rise in a symmetric manner with a lower tilt than their *rotation dominated* peers. A low tilt results in a smaller net flux transport to the pole: the source term loses efficiency as the magnetic flux tube gains buoyancy. The meridional profile of the quenched source term can be written as:

$$S(r,\theta,t) \;=\; f(r,\theta) \sum_{n\,:\,t_n=t-\tau_{\rm rise}(n)} \left[\left[1+\left(\frac{B_{\rm delay}(\theta,t_n)}{B_{\rm quench}}\right)^2\right]^{-1} B_{\rm delay}(\theta,t_n)\right],$$

$$\text{for} \qquad |B_{\rm delay}(\theta,t_n)| > B_{\rm threshold}\ ,\ \ S=0 \text{ otherwise}\ , \tag{6.12}$$

where n and $B_{\rm delay}(\theta,t_n) = B_\phi(r_0,\theta,t-\tau_{\rm rise}(n))$ are the time step's index and the toroidal magnetic field at the bottom of the convective zone ($r_0 = 0.7$) at $t-\tau_{\rm rise}(n)$; $B_{\rm quench}$ is the magnetic flux density at which the source term is quenched, as suggested by the work of Rempel (2006), we choose $B_{\rm quench} = B_{\rm eq}$ with $B_{\rm eq}$ being the magnetic flux density in equipartition with the convective motions at t_n; f is a dimensionless profile of the source term. The sum is done over all time steps, n, such that $t_n + \tau_{\rm rise}(n) = t$ and $B_{\rm delay}(\theta,t_n) > B_{\rm threshold}$. The Babcock-Leighton

source term is effective only at the surface, for $r > 0.9$

$$f(r,\theta) = \frac{1}{2}\left[1 + \mathrm{erf}\left(\frac{r-0.9}{0.02}\right)\right]\cos\theta\sin^2\theta\ . \tag{6.13}$$

The factor $\cos\theta\sin^2\theta$ ensures that the contribution of flux tubes is maximum between 0 and 40° latitude, as it is observed for the solar-case. $B_{\mathrm{threshold}}$ is introduced in this formulation to prevent magnetic flux tubes that are too weak from reaching the surface and contributing to the source term. We set the threshold such that magnetic flux tubes weaker than 6kG ($10\%B_{\mathrm{eq}}$) do not participate to the dynamo mechanism.

6.3.2 Introduction of the delay

Now that we described the setup, we still need to extract the τ_{rise} from the scaling law. We have shown that

$$\tilde{\tau}_{\mathrm{rise}} \propto \left(\Gamma_{\alpha_1}^{\alpha_2}\right)^{\alpha_3} \propto \left(\frac{B_0^{\alpha_1}}{\Omega}\right)^{\alpha_2\alpha_3}\ , \tag{6.14}$$

hence, considering a given star, rotation is a constant, and Eq. (6.14) connects τ_{rise} to B_0 at the bottom of the convective zone:

$$\tau_{\mathrm{rise}} \propto \left(\frac{B_0}{B_{\mathrm{eq}}}\right)^{\alpha_u}\ , \tag{6.15}$$

with α_u being the universal power. This number is a function of m only. It is defined as

$$\alpha_u = \alpha_1\alpha_2\alpha_3\ . \tag{6.16}$$

It leads to two functions for $m = 0$ and $m = 8$:

$$\begin{aligned} \tau_{\mathrm{rise}}^{(0)} &\propto \left(\frac{B_0}{B_{\mathrm{eq}}}\right)^{-2}, \\ \tau_{\mathrm{rise}}^{(8)} &\propto \left(\frac{B_0}{B_{\mathrm{eq}}}\right)^{-0.95}. \end{aligned} \tag{6.17}$$

To treat the delay numerically, we compute and memorized the source term S and its corresponding delay τ_{delay} at each time step. At t_{emerg} the contribution of the source term is added to all other contributions of further magnetic flux tubes emerging at the same time. The delay is computed as follows:

$$\tau_{\mathrm{rise}} = \tau_0\ \sin\theta\ \left(F_{\mathrm{amp}}\left|\frac{B_\phi}{B_{\mathrm{eq}}}\right|\right)^{\alpha_u}\ , \tag{6.18}$$

where τ_0 is the "typical" delay of an equipartition magnetic flux tube (with $B_0 = F_{\rm amp} B_\phi = B_{\rm eq}$). From the direct numerical simulations, we know that τ_0 depends on m. The factor $sin\,\theta$ is inherited from the tension force acting on the flux tube: close to the pole, the curvature radius, $\mathcal{R}$, becomes sufficiently small such that the tension force takes over buoyancy and the flux tube does not rise. $F_{\rm amp}$ is the amplification factor, it represents the missing ingredient of our scenario of how magnetic flux tubes form. How does their strength depend on the strength of the magnetic layer they emerge from? As we mentioned in the introduction, this discussion is out of the scope of the present work, and will be addressed in future studies. However, Rempel & Schüssler (2001) shows that the 'explosion' instability which may occur at the bottom of the convective zone can amplify the magnetic flux density of a stable magnetic layer up to one order of magnitude. In reality, this parameter might vary with B_ϕ, rotation, stellar structure, or how deep the flux tube forms. This issue has not been addressed yet and needs to be studied. But without further constraints at hand, we arbitrarily chose to set $F_{\rm amp}$ to 10. Note that introducing $F_{\rm amp}$ prevents magnetic flux tubes weaker than $B_0 = F_{\rm amp} B_{\rm threshold}$ from rising. We suppose that $B_0 = 0.1 B_{\rm eq}$ is the weakest magnetic flux density that leads to an emerging magnetic flux tube, therefore the threshold on the toroidal field at the bottom of the convective zone should be $B_{\rm threshold} = 0.01 B_{\rm eq}$.

Now that we have fully described the delayed *flux tube/Babcock-Leighton dynamo*, we present some results of a parameter study on τ_0, C_S and α_u.

6.3.3 Preliminary results

Along this section we will demonstrate that introducing a delay in the *flux tube/Babcock-Leighton dynamo* reduces the critical C_S required to obtain an antisymmetric oscillatory solution. And that this reduction does not only extend the standard solutions but also reveals a **new dynamo regime**.

We carried out a parameter study, varying the equipartition delay (τ_0) and the control-parameter C_S, with the following fixed parameters:

$$B_{\rm threshold} = 0.01 \;\; ; \;\; C_\Omega = 1.25\ 10^4 \;\; ; \;\; {\rm Re} = 440 \;\; ; \;\; \alpha_u = -2 \; .$$

In the case of $\tau_0 = 0$, we could reproduce identical results as in the non-delayed Babcock-Leighton dynamo. In Fig. 6.4, we illustrate the resulting toroidal field at the bottom of the convective zone ($r = 0.71$) and the squared toroidal field (at the same depth) at 20 degrees latitude for $C_S = 300$. Note that this latter quantity can be seen as a proxy for the sunspots number. This simulation is supercritical and delivers a standard solution: setting the rotation period to the solar

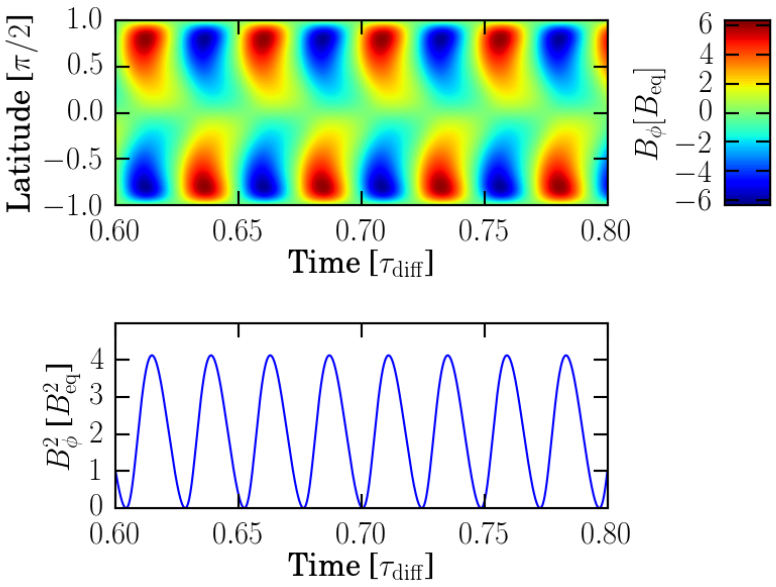

Figure 6.4: Toroidal magnetic field at the bottom of the convective zone (top panel) for a non-delayed flux tube/Babcock-Leighton dynamo versus time, and the evolution of the same quantity squared at 20 degrees latitude (lower panel).

value ($P_{\rm rot}$ = 25 d) and a meridional circulation of 10 m/s, we obtain a 22-year magnetic cycle, a diffusion time of 440 years, and a maximum amplitude of about the equipartition value.

In Fig. 6.5, we plot the maximum of the absolute B_ϕ against C_S, for four different τ_0. The black solid line represents the series with $\tau_0 = 0$, those dynamos decay with a C_S smaller than $C_0^{\rm crit} \equiv C_S^{\rm crit}(\tau_0 = 0) \approx 72$. In the same plot, series with a non-zero τ_0 (colored lines) show a lower maximum B_ϕ for values of $C_S < C_0^{\rm crit} = 72$, but the dynamos do not decay. Those dynamos differ from the super-critical [1] ones, we identified a 'new' regime.

In Fig. 6.6, we illustrate two examples of dynamos with $\tau_0 = 10^{-3}$: a 'super-critical dynamo' with $C_S = 300$, and a non-decaying 'sub-critical dynamo' with $C_S = 15$. Three remarkable characteristics differ: the period of the magnetic cycle lasts about twice longer in the sub-critical case; the maximum B_ϕ stays at lower values; and the cycle is less sinusoidal.

In the bottom panels of Fig. 6.6 we illustrate the relation between the various relevant times scales. The green and the red solid lines represent the delay of a magnetic flux tube of $B_0 = B_{\rm eq}$, and the period of the magnetic cycle, respectively. The blue oscillating curve represents the effective delay ($\tau_{\rm delay}$) computed from the $B_\phi(t)$ such that $t + \tau_{\rm delay} = t_{\rm emerg}$; with $B_\phi(t)$ taken a the bottom of the convective

[1] In the present case we call 'super-critical' solutions the ones with a $C_S > C_0^{\rm crit}$ and 'sub-critical' solutions the ones with $C_S < C_0^{\rm crit}$, they are linearly sub-critical without time delay, but they nonlinearly saturates to a finite amplitude when the time delay is introduced.

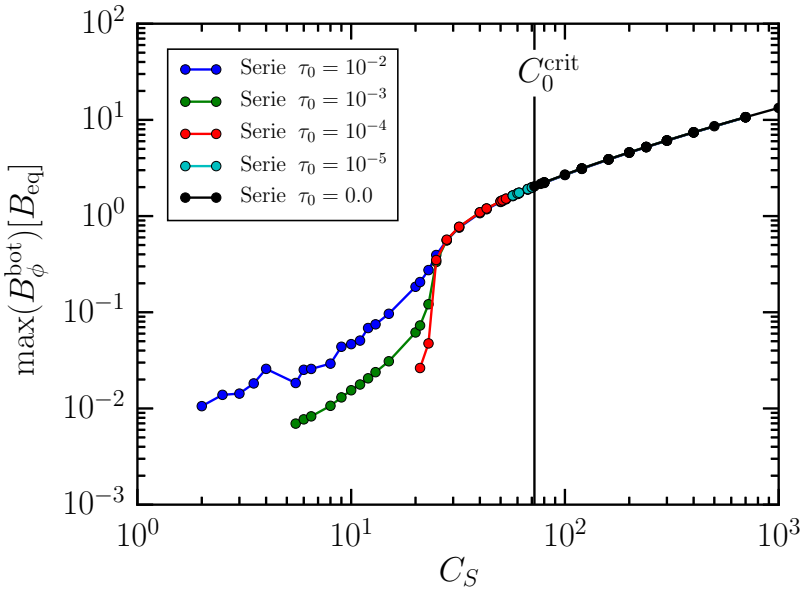

Figure 6.5: Maximum field amplitude at the bottom of the convection zone, $B_\phi^{\rm bot}$ in units of $B_{\rm eq}$, of delayed and non-delayed Babcock-Leighton dynamos versus the dynamo number C_S. Each point represent a dynamo solution. The black solid curve represents the case of a non-delayed Babcock-Leighton dynamo. The colored curves represent various series of delayed Babcock-Leighton dynamos with different equipartition delays τ_0: the blue, green, red, and cyan lines represent the series with τ_0 of 10^{-2}, 10^{-3}, 10^{-4} and 10^{-5} ($\tau_{\rm diff}$), respectively. The vertical black solid line indicates the critical $C_{\rm S}$ for the non-delayed *Babcock-Leighton dynamo*.

zone and at 20 degrees latitude. The dashed blue line represents the minimum effective delay computed from the maximum value of B_ϕ at all latitude and $r = 0.71$.

In the super-critical case (panel (a)), most of the time the effective delay is less than 1% of the magnetic cycle. In those dynamos, the effective delay remains small compared to the magnetic cycle and the dynamo delivers a solution similar to the non-delayed dynamos.

The non-decaying sub-critical solution (panel (b)) instead exhibits most of the time an effective delay that lasts longer than the magnetic cycle. It is only at maximum activity that $\tau_{\rm delay}$ is shorter than the cycle period. Those dynamos self-adjust and deliver oscillatory solutions.

In Fig. 6.7 we plot the minimum of the relative delay ($\tau_{\rm delay}/P_{\rm cyc}$) against C_S. For all sub-critical dynamos, independently of τ_0, the ratio of the delay over the cycle period is close to unity. A question arises: *does the delay determine the cycle?*

In Fig. 6.8, we plot the magnetic cycle for various C_S and τ_0. Each solid curve represents a series obtained from a given τ_0. As we vary τ_0 the magnetic cycle remains invariant. In the super-critical regime the cycle period is almost constant, alike non-delayed dynamos. When C_S reaches the $C_0^{\rm crit}$ of the non-delayed Babcock-

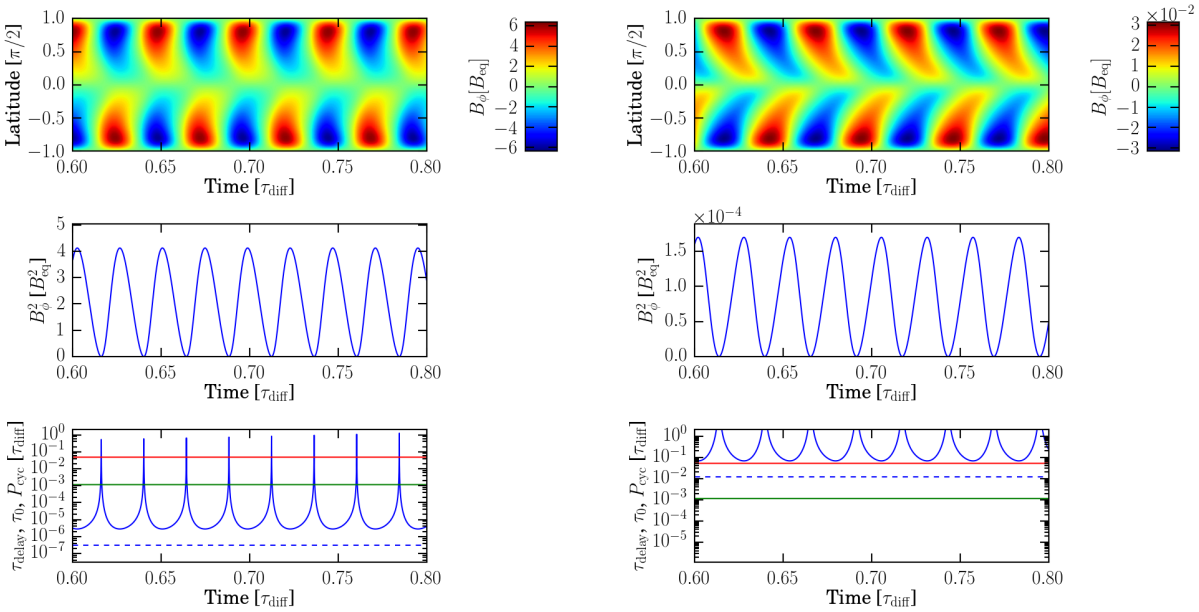

Figure 6.6: These plots represent the various relevant quantities for representative examples of both super-critical (left column) and non-decaying sub-critical (right column) dynamos. The upper panels represent the toroidal magnetic field, B_ϕ, at the bottom of the convective zone over latitude against time. The middle panels are a slice at 20 degrees latitude of squared B_ϕ. The lower panels represent various important time scales. The red and green solid lines represent the cycle period and the delay of a magnetic flux tube of $B_0 = B_{\rm eq}$, respectively. The blue curve represents the effective delay in the source term at 20 degrees latitude. The blue dashed line represents the minimum of the effective delay at all latitudes.

Leighton dynamo the magnetic cycle period increases, following a power law with exponent -1.

So in the sub-critical regime, the delay does not determine the cycle, on the contrary it adjusts to the magnetic cycle independently of τ_0. This adjustment is illustrated in Figs. 6.5 and 6.8: the maximum B_ϕ increases with τ_0 (Fig. 6.5) such that the minimum delay always remains lower than the magnetic cycle (Fig. 6.8).

An opened question remains, what determines the magnetic cycle? We suggest two explanations: the cycle may arise from a resonance between the effective delay and either the diffusion time, or the meridional circulation time-scale. Further studies are needed to clarify that issue.

Fig. 6.7 tells us that in the sub-critical regime, the effective delay adjusts to a large fraction of the cycle. And as C_S decreases this fraction gets larger, until it reaches the cycle period. In those cases, the sub-critical dynamo delivers a decaying solution.

Introducing a delay into the Babcock-Leighton dynamo, we already obtained remarkable insight; the main result of the previous chapters demonstrates that the de-

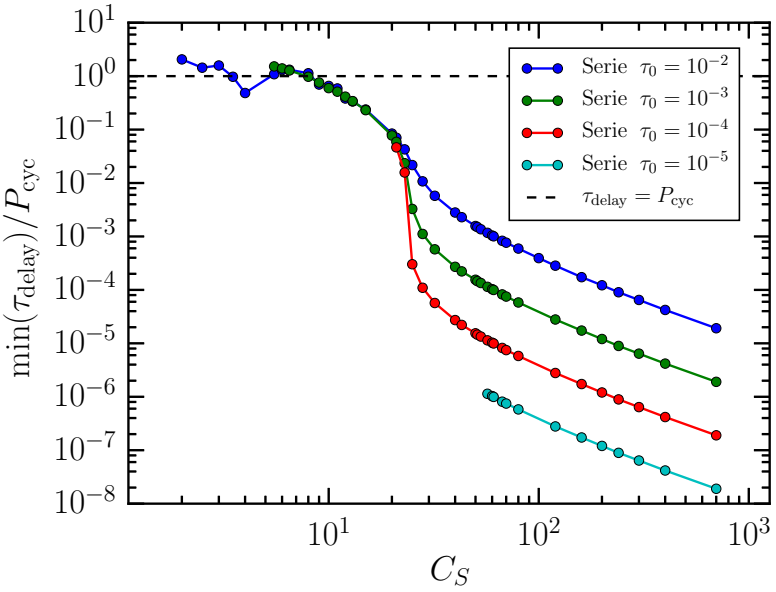

Figure 6.7: Here we plot the minimum effective delay, $\tau_{\rm delay}$ normalized by $P_{\rm cyc}$ against the dynamo number C_S. Each point represents a dynamo solution. The effective delay at a time t is computed from B_ϕ at the bottom of the convective zone, and 20 degrees latitude at the same time. This delay represent some sort of measurement of the latitudinal average of the minimum delay. The colored lines represent various series of delayed Babcock-Leighton dynamos with different equipartition delay τ_0. The blue, green, red and cyan lines represent the series with τ_0 of 10^{-2}, 10^{-3}, 10^{-4} and 10^{-5} ($\tau_{\rm diff}$), respectively.

lay follows various power laws, whose exponents depend on the preferred wavenumber m. We carried out a further parameter study on α_u. We vary α_u from -0.95 ($m = 8$) to -2 ($m = 0$). Those series demonstrate on the one hand that the super-critical regime remains unaffected. On the other hand, the sub-critical regime reacts: the decrease of α_u reduces the maximum of B_ϕ and the relative effective delay; the magnetic cycle remains unchanged.

6.3.4 Discussion

There are limitations in our dynamo model. As mentioned earlier, the amplification parameter $F_{\rm amp}$ needs to be studied. We can not predict how B_ϕ, rotation or any further stellar properties may control $F_{\rm amp}$. We also need to figure out which parameters determine the preferred wavenumber m, and if several modes could be present simultaneously. These free parameters need to be constrained thanks to direct numerical simulations. Furthermore, our model considers only anti-symmetric latitudinal modes, symmetric modes may also be present in the solution.

In any case these results suggest that a few strong emergence events are sufficient to maintain a sub-critical dynamo. But this is not sufficient for suggesting such

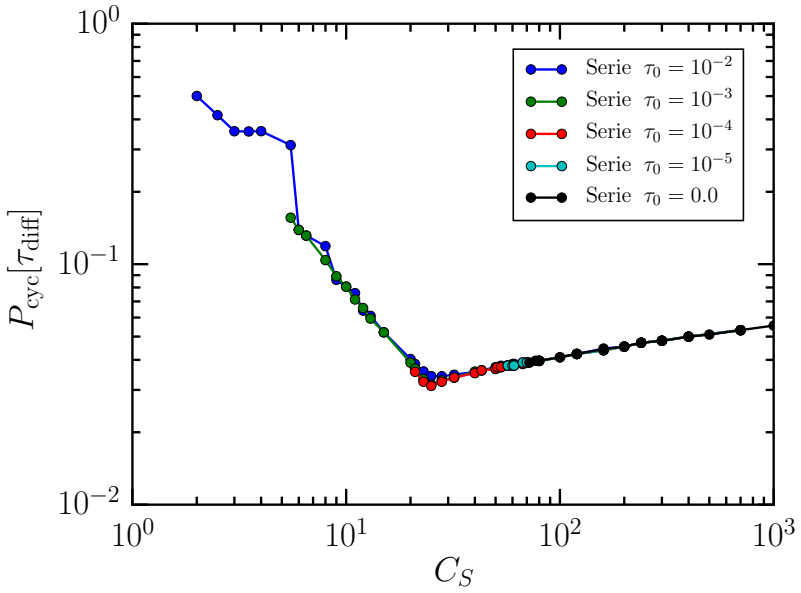

Figure 6.8: Magnetic cycle period, $P_{\rm cyc}$, against the dynamo number C_S. Each point represents a dynamo solution. The black curve represents the non-delayed case ($\tau_0 = 0$). The colored curves represent various series of delayed Babcock-Leighton dynamos with different equipartition delay τ_0. The blue, green, red and cyan curves represent the series with τ_0 of 10^{-2}, 10^{-3}, 10^{-4} and 10^{-5} ($\tau_{\rm diff}$), respectively.

a mechanism to be present in the solar dynamo. In the solar case, these strong events may still originate from sub-equipartition magnetic flux tubes, which may not reach the surface because of the destructive convective motions. In the case of fast rotating stars – like a young Sun – according the scaling law we found in Chap. 5 magnetic flux tubes close to equipartition may rise within a magnetic cycle and lead to sub-critical dynamos.

6.4 Summary

Along this work, we have shown that the rise time of the magnetic flux tube can reach a significant fraction of the observed cycle period of inactive stars Fig. 6.2. This motivates us to study delayed *flux tube/Babcock-Leighton* dynamos.

We constrained the delay thanks to the results of our direct numerical simulations. We introduced the constrained delay into the Babcock-Leighton dynamo and obtained a sub-critical regime that has not yet been found in kinematic dynamo models. This dynamo regime has the particularity to self-adjust such that even for long delays – of the order of the cycle period – the solution remains oscillatory.

7 Conclusions

Figuring out how the dynamo mechanism operates in cool stars remains a major challenge for the stellar community. The *flux tube/Babcock-Leighton* dynamo seems to be a good candidate to explain the dynamics of solar-like stars' magnetic fields. The traditional version of this dynamo assumes that the rise time of magnetic flux tubes may be neglected compared to the magnetic cycle. This assumption may be acceptable for the solar case, but is not obviously valid for faster rotators. In a similar manner as Jouve et al. (2010), we extended the *flux tube/Babcock-Leighton* dynamo by considering a non-instantaneous rise of magnetic flux tubes. As an improvement to their work, we constrain the delay with the rise time derived from our numerical simulations.

Therefore, we need a relation that links the rise time of magnetic flux tubes to the relevant characteristics of their stellar host. Since solar-like stars exhibit a wide range of rotation rates Ω – which have been shown to depend on the stellar age – and magnetic activity, the magnetic flux density of the flux tube and the rotation period are the most relevant parameters to determine the rise time of magnetic flux tubes.

To obtain such a relation we designed a numerical setup that simulates the rise of magnetic flux tubes in stellar interiors. We designed a fully compressible setup of a rising magnetic flux tube in an adiabatically stratified spherical shell, which rotates uniformly. We carried out axisymmetric and non-axisymmetric versions of these simulations and extracted the necessary relation which we finally introduced into a *delayed flux tube/Babcock-Leighton* dynamo.

The large disparity between the sound speed, c_s, and the velocity of the convective motions, which supposedly occur in the convective envelopes of solar-like stars, limits the time scale of the studied problem. This limit prevents us from simulating a magnetic flux tube in a compressible convective environment. To solve this issue, we consider a static, adiabatically stratified interior that mimics the quasi-stationary character of a convective zone. Another issue arises from the compressible character of the setup that prevents us from simulating magnetic flux tubes of high plasma-β like the one expected in the Sun (10^5). In order to solve this crucial problem, we needed to investigate a possible scaling relation, which would allow us to carry out

simulations at lower β.

Simulations can be compared with reality only if the relevant processes occur in realistic regimes. Because the realistic parameter space (β, $\mathcal{M}_{\rm rot}$) is out of reach, we need to find a parameter that controls the regime of the rise. Schüssler & Solanki (1992) already addressed that question. They found that in axisymmetric rises only the buoyant force and the Coriolis force act on the rise of magnetic flux tubes. They found that the magnetic Rossby number $\mathrm{Ro_m}$ controls the nature of the regime:

$$\frac{F_{\rm buoy}}{F_{\rm corio}} \propto \mathrm{Ro_m} \propto \frac{\mathrm{v_A}}{\varpi\Omega} \ .$$

A low magnetic Rossby number indicates a *rotation dominated* regime, while a high magnetic Rossby number denotes a *buoyancy dominated* regime. We extended their work to the non-axisymmetric case by considering the impact of the magnetic tension arising from the Ω-shape of non-axisymmetric magnetic loops, and designed a scaling parameter that unifies axisymmetric and non-axisymmetric results:

$$\frac{F_{\rm buoy}}{F_{\rm corio}} \propto \Gamma_{\alpha_1}^{\alpha_2} = \left(\frac{v_{\rm A}^{\alpha_1}\, c_{\rm s}^{1-\alpha_1}}{\varpi\Omega} \right)^{\alpha_2} ,$$

where α_1 and α_2 both depend on the azimuthal wave number m that is preferred during the rise. In the particular case of axisymmetric rises ($m = 0$) we found α_1 and α_2 both being unity. The scaling parameter reduces to Γ_1^1 which is indeed proportional to the magnetic Rossby number.

By considering the influence of magnetic tension on the rise of magnetic flux tubes, we have predicted that $\Gamma_{\alpha_1}^{\alpha_2}$ controls the nature of the regime: for a given m, two simulations with the same $\Gamma_{\alpha_1}^{\alpha_2}$ should give the same result, independently of the values of Ω and β. This powerful tool allowed us to carry out simulations with a lower β but still in a realistic regime. Ensuring the realistic character of the regime allows us to compare our simulations with observations.

But before verifying our prediction, we needed to make sure that our numerical setup behaves in a proper manner. We compared our results with former studies and found that our axisymmetric results agree with former conclusions obtained with the thin flux tube approximation. The rise time, the latitudes of emergence, as well as the path taken by the magnetic flux tubes are all compatible. We extended the setup to the $m = 8$ non-axisymmetric mode and found that the morphological properties of the rise were again compatible to anelastic and thin flux tube conclusions. We concluded that our setup behaves properly and that the thin flux tube and the anelastic approximations are both well justified in the bulk of the solar convection zone.

The axisymmetric study also demonstrates that the axisymmetric setup indeed scales with Γ_1^1.

For the non-axisymmetric case, we first needed to compute α_1 and α_2, from the relation between the curvature radius $\mathcal{R}$ of the Ω-shaped loops with β and the stellar rotation. For the $m = 8$ case, we found $\alpha_1(8) = 0.793$ and $\alpha_2(8) = 0.855$. As predicted the numerical simulations show a scaling with $\Gamma_{0.793}^{0.855}$. Such a scaling behavior demonstrates that the assumption that magnetic tension influences the regime of the rise of magnetic flux tubes should be correct, and that it is possible to simulate axisymmetric as well as non-axisymmetric compressible rising magnetic flux tubes in a regime that is comparable to the solar one.

From the direct numerical simulations, we extracted the relation linking the relative rise time and the regime of the rise for both $m = 0$ and $m = 8$. In both cases, we obtained a power law:

$$\tilde{\tau}_{\text{rise}} \propto \left(\Gamma_{\alpha_1}^{\alpha_2}\right)^{\alpha_3},$$

with $\alpha_3 = -2$ and a proportionality factor of 2.24 in the axisymmetric case; and $\alpha_3 = -1.4$ and a proportionality factor of 7.53 in the $m = 8$ case.

These two relations for $m = 0$ and $m = 8$ can already be used to constrain a *flux tube/Babcock-Leighton* dynamo. The latter requires the link between the rise time and both the magnetic flux density of the flux tube and stellar rotation. $\Gamma_{\alpha_1}^{\alpha_2}$ has the advantage of containing both, and the universality of its relation to the relative rise time makes it valid for any solar-like star. But the fact that we just have access to discrete values of α_3 and the proportionality factor already reveal the limits of our theoretical work.

The proportionality factor itself depends on several stellar parameters such as heat conduction, viscosity, the aspect ratio of the star and obviously m. Further studies are required to derive a theoretical expression for this factor. In the present case we constrain the latter by simulations.

We suggest that the α_3 dependence on m can be explained by the pressure gradient arising between the apex and the feet of non-axisymmetric loops. Additional studies are needed to clarify that particular issue. Again, we constrain α_3 with the results obtained from simulations.

We have also shown that the regime of the rise does not only depend on the magnetic flux density of the flux tube and the stellar rotation period, but also on the azimuthal wave number m that is preferred along the rise. Unfortunately, the question of which mode is preferred during the rise, is still open. Studying the formation of magnetic flux tubes in spherical coordinates may give some hints toward a final answer.

Finally, our setup neither takes convection nor differential rotation into account. At least convection will inevitably alter the results (Weber et al. 2011) – while the effect of differential rotation appears to be small (Fan et al. 1994). Nevertheless, when larger computational power will permit extending the setup to convective and differentially rotating interiors, our results will provide a solid base of comparison.

Despite these limits, the universality of the power law that relates the relative rise time and the regime of the rise can be used to constrain the delay in a *delayed flux tube/Babcock-Leighton* dynamo.

The numerical simulations tell us that the rise time, i.e. the delay, depends on the toroidal magnetic field:

$$\tau_{\mathrm{delay}} = \tau_0 \left(F_{\mathrm{amp}} \frac{B_\phi}{B_{\mathrm{eq}}} \right)^{\alpha_u},$$

with $\alpha_u = -2$ in the axisymmetric case and $\alpha_u = -0.95$ in the $m = 8$ case. Because of the limits we discussed along this work, τ_0 and F_{amp} remain free parameters, while B_{eq} is usually constrained with the convective velocity from stellar models. Considering reasonable values for these three parameters, we found that being delayed, the *flux tube/Babcock-Leighton* dynamo exhibits two regimes: a super-critical regime and a non-decaying sub-critical regime.

This dissertation has shown that the relative rise time of magnetic flux tubes in solar-like stars follows a powerlaw of $\Gamma_{\alpha_1}^{\alpha_2}$, that allows us to constrain a delayed *flux tube/Babcock-Leighton dynamo*. We have shown that for dynamo numbers that lead to decay in the non-delayed case, a long delay – that lasts for a significant fraction of the cycle – does not necessarily deliver a decaying solution and we identified a new dynamo regime. The question of the existence of this regime in stellar objects remains open. But such a regime seems to be a good candidate for solar-like stars rotating in a few days and exhibits weak magnetic activity.

Our work has demonstrated the importance of the azimuthal wavenumber m that is preferred during the rise of magnetic flux tubes. The fact that m remains unknown is an issue. And it becomes clear that the study of the formation of magnetic flux tubes has never been so crucial to figure out where the dynamo mechanism operates in solar-like stars.

Appendix: List of simulations

Table A.1: List of all axisymmetric simulations based on the STD-2D setup. The labels refer to the panels in Fig. 4.4, with (a.1) and (a.2) referring to the green and red contours of panel (a), respectively.

Series 2D	$m = 0$	$\alpha_1 = 1$	$\alpha_2 = 1$	
$\Gamma_{\alpha_1}^{\alpha_2}$	$\mathcal{M}_{\rm rot}$	β	$\tilde{\tau}_{\rm rise}$	labels
3.162	0.325	1.135	0.254	
2.846	0.325	1.401	0.260	
2.846	0.244	2.491	0.261	
2.372	0.406	1.291	0.359	
2.372	0.325	2.018	0.393	
1.897	0.488	1.401	0.477	
1.897	0.325	3.153	0.550	(b)
1.708	0.488	1.730	0.651	
1.660	0.325	4.118	0.814	
1.550	0.406	3.026	1.082	
1.470	0.406	3.360	1.325	
1.455	0.488	2.384	1.276	(c)
1.360	0.406	3.929	1.488	
1.297	0.488	3.001	1.676	
1.265	0.406	4.540	1.732	
1.217	0.650	1.914	1.772	
1.217	0.569	2.501	1.713	
1.217	0.528	2.900	1.811	
1.217	0.488	3.404	1.778	
1.217	0.447	4.050	1.813	(a.1)
1.217	0.406	4.901	1.813	(a.2)
1.217	0.366	6.051	1.779	
1.217	0.325	7.658	1.775	
1.217	0.285	10.00	1.723	

Continued on next page

Continued from previous page

$\Gamma_{\alpha_1}^{\alpha_2}$	$\mathcal{M}_{\text{rot}}$	β	$\tilde{\tau}_{\text{rise}}$	labels
1.217	0.203	19.60	1.670	
1.217	0.163	30.63	1.653	
1.217	0.122	54.45	1.621	
1.186	0.488	3.587	1.876	
1.186	0.406	5.166	1.815	
1.186	0.325	8.072	1.777	
1.154	0.406	5.453	1.895	
1.107	0.488	4.118	1.979	
1.059	0.569	3.303	2.072	
0.791	0.325	18.16	4.460	(d)

Table A.2: List of all non-axisymmetric simulations based on the STD-3D setup. The letters of the labels refer to the panels in Figs. 5.3 and 5.8, respectively referred by their number. The lines in italics refer to the simulations where the computation of the curvature radius is not reliable.

Series 3D $m = 8$ $\alpha_1 = 0.793$ $\alpha_2 = 0.855$

$\Gamma_{\alpha_1}^{\alpha_2}$	$\mathcal{M}_{\text{rot}}$	β	$\tilde{\tau}_{\text{rise}}$	labels
8.733	0.08	1.166	0.441	$(a$ 5.8$)$
7.185	0.08	2.073	0.53	
6.419	0.04	16.605	0.609	
5.885	0.08	3.735	0.616	
4.828	0.16	1.166	0.948	$(a$ 5.3$)/(b$ 5.8$)$
3.973	0.16	2.073	0.98	
3.973	0.16	2.073	1.062	
3.86	0.08	12.957	1.125	
3.463	0.16	3.108	1.216	
2.809	0.241	2.073	1.593	$(b$ 5.3$)$
2.733	0.281	1.523	1.505	
2.669	0.321	1.166	2.072	
2.594	0.16	7.288	1.768	$(c$ 5.8$)$
2.134	0.16	12.957	2.502	
1.886	0.16	18.658	3.24	

Continued on next page

Continued from previous page

$\Gamma_{\alpha_1}^{\alpha_2}$	$\mathcal{M}_{\text{rot}}$	β	$\tilde{\tau}_{\text{rise}}$	labels
1.757	0.481	1.44	3.162	(c 5.3)
1.657	0.481	1.713	3.582	
1.634	0.241	10.237	3.816	
1.621	0.16	29.153	4.1	
1.604	0.401	2.985	3.94	
1.553	0.481	2.073	4.05	
1.509	0.241	12.957	4.425	
1.446	0.481	2.559	4.44	
1.434	0.321	7.288	4.8	
1.429	*0.196*	*25.374*	*4.251*	
1.378	0.241	16.923	5.085	
1.343	0.561	2.159	5.257	
1.335	0.481	3.239	5.16	
1.321	0.561	2.265	5.299	
1.299	0.561	2.38	5.348	(d 5.3)
1.219	0.481	4.231	5.7	
1.098	0.481	5.759	6.6	(d 5.8)
0.944	0.561	6.092	8.47	
0.834	*0.481*	*12.957*	*10.482*	
0.812	*0.561*	*9.519*	*10.29*	(e 5.3)
0.686	*0.481*	*23.034*	*12.72*	(f 5.3)
0.668	*0.561*	*16.923*	*13.37*	

Bibliography

Abbett, W. P., Fisher, G. H., & Fan, Y. 2001, ApJ, 546, 1194 ..... p. 15

Arlt, R., Leussu, R., Giese, N., Mursula, K., & Usoskin, I. G. 2013, MNRAS, 433, 3165 ..... p. 4

Augustson, K. C., Brown, B. P., Brun, A. S., Miesch, M. S., & Toomre, J. 2012, ApJ, 756, 169 ..... p. 24

Babcock, H. W. 1961, ApJ, 133, 572 ..... p. 2 and 13

Baranyi, T. 2015, MNRAS, 447, 1857 ..... p. 5

Barnes, S. A. & Kim, Y.-C. 2010, ApJ, 721, 675 ..... p. 70

Barnes, S. A., Weingrill, J., Fritzewski, D., Strassmeier, K. G., & Platais, I. 2016, ApJ, 823, 16 ..... p. 3

Brown, B. P., Browning, M. K., Brun, A. S., Miesch, M. S., & Toomre, J. 2010, ApJ, 711, 424 ..... p. 8

Brown, T. M., Christensen-Dalsgaard, J., Dziembowski, W. A., et al. 1989, ApJ, 343, 526 ..... p. 3

Brun, A. S., Miesch, M. S., & Toomre, J. 2004, ApJ, 614, 1073 ..... p. 8

Böhm-Vitense, E. 2007, ApJ, 657, 486 ..... p. 70

Caligari, P., Moreno-Insertis, F., & Schüssler, M. 1995, ApJ, 441, 886 p. 15 and 31

Caligari, P., Schüssler, M., & Moreno-Insertis, F. 1998, ApJ, 502, 481 ..... p. 31

Caligari, P., Schüssler, M., Solanki, S. K., Schaerer, D., & Stix, M. 1996, ApL&C, 34, 17 ..... p. 15

Charbonneau, P. 2010, Liv. Rev. Sol. Phys., 7, 3 ..... p. 6

Cheung, M. C. M., Moreno-Insertis, F., & Schüssler, M. 2006, A&A, 451, 303 p. 12, 17, 18, and 40

Choudhuri, A. R. 1989, Sol. Phys., 123, 217 ..... p. 10

Choudhuri, A. R. & Gilman, P. A. 1987, ApJ, 316, 788 .. p. 10, 19, 31, 32, 38, 46, and 50

Dasi-Espuig, M., Solanki, S. K., Krivova, N. A., Cameron, R., & Peñuela, T. 2010, A&A, 518, A7 ..... p. 5

Diercke, A., Arlt, R., & Denker, C. 2015, AN, 336, 53 ..... p. 4

Dorch, S. B. F., Archontis, V., & Nordlund, Å. 1999, A&A, 352, L79 ..... p. 11

D'Silva, S. & Choudhuri, A. R. 1993, A&A, 272, 621 ..... p. 31

Emonet, T. & Moreno-Insertis, F. 1998, ApJ, 492, 804 ..... p. 11

Fan, Y. 2001, ApJ, 546, 509 ..... p. 10 and 14

Fan, Y. 2008, ApJ, 676, 680 ..... p. 11, 14, 15, 24, 40, 48, 53, 61, and 65

Fan, Y., Abbett, W. P., & Fisher, G. H. 2003, ApJ, 582, 1206 ..... p. 73

Fan, Y. & Fisher, G. H. 1996, Sol. Phys., 166, 17 ..... p. 31

Fan, Y., Fisher, G. H., & Deluca, E. E. 1993, ApJ, 405, 390 ..... p. 31

Fan, Y., Fisher, G. H., & McClymont, A. N. 1994, ApJ, 436, 907 ... p. 10, 25, 50, and 88

Fan, Y., Zweibel, E. G., & Lantz, S. R. 1998, ApJ, 493, 480 ..... p. 11

Favier, B., Jouve, L., Edmunds, W., Silvers, L. J., & Proctor, M. R. E. 2012, MNRAS, 426, 3349 ..... p. 14

Folsom, C. P., Petit, P., Bouvier, J., et al. 2016, MNRAS, 457, 580 ..... p. 6

Gastine, T., Yadav, R. K., Morin, J., Reiners, A., & Wicht, J. 2014, MNRAS, 438, L76 ..... p. 24

Gilman, P. A. & Rempel, M. 2005, ApJ, 630, 615 ..... p. 14

Granzer, T. 2004, AN, 325, 417 ..... p. 15

Guerrero, G., Smolarkiewicz, P. K., Kosovichev, A. G., & Mansour, N. N. 2013, ApJ, 779, 176 ..... p. 24

Hackman, T., Lehtinen, J., Rosén, L., Kochukhov, O., & Käpylä, M. J. 2016, A&A, 587, A28 ..... p. 6

Hale, G. E. 1908, ApJ, 28, 315 ..... p. 4

Hale, G. E., Ellerman, F., Nicholson, S. B., & Joy, A. H. 1919, ApJ, 49, 153 ..p. 5

Harvey, K. L. & Zwaan, C. 1993, Sol. Phys., 148, 85 ..... p. 5

Hollerbach, R. 2000, Int. J. Numer. Meth. Fluids, 32, 773 ..... p. 76

Howard, R. F. 1991, Sol. Phys., 136, 251 ..... p. 5

Howard, R. F. 1993, in Bulletin of the American Astronomical Society, Vol. 25, 1182 p. 5

Howe, R. 2009, Liv. Rev. Sol. Phys., 6, 1 ..... p. 3

Jakimiec, J., Sylwester, B., Sylwester, J., et al. 1986, CAOSP, 15, 123 ..... p. 5

Jones, C. A., Boronski, P., Brun, A. S., et al. 2011, Icarus, 216, 120 ..... p. 15

Jouve, L. & Brun, A. S. 2009, ApJ, 701, 1300 .... p. 14, 15, 22, 40, 41, 53, and 73

Jouve, L., Brun, A. S., & Aulanier, G. 2013, ApJ, 762, 4 .p. 11, 15, 42, 53, and 63

Jouve, L., Proctor, M. R. E., & Lesur, G. 2010, A&A, 519, A68 ..... p. 69 and 85

Jouve, L., Silvers, L. J., & Proctor, M. R. E. 2012, in SF2A-2012: Proceedings of the Annual meeting of the French Society of Astronomy and Astrophysics, eprint: arXiv:1210.7999, 409–413 ..... p. 11 and 14

Käpylä, P. J., Korpi, M. J., Brandenburg, A., Mitra, D., & Tavakol, R. 2010, AN, 331, 73 ..... p. 8

Käpylä, P. J., Mantere, M. J., & Brandenburg, A. 2012, ApJ, 755, L22 ..... p. 8

Karak, B. B., Käpylä, P. J., Käpylä, M. J., et al. 2015, A&A, 576, A26 ..... p. 24

Kővári, Z. & Oláh, K. 2014, Space Sci. Rev., 186, 457 ..... p. 13

Kitchatinov, L. L. & Rüdiger, G. 2005, AN, 326, 379 ..... p. 24

Kraft, R. P. 1967, ApJ, 150, 551 ..... p. 3

Küker, M. & Rüdiger, G. 2011, AN, 332, 933 ..... p. 24, 71, 76, and 77

Lantz, S. R. & Fan, Y. 1999, ApJS, 121, 247 ..... p. 16

Leighton, R. B. 1964, ApJ, 140, 1547 . . . . . p. 2

Matthews, P. C., Hughes, D. W., & Proctor, M. R. E. 1995, ApJ, 448, 938 . . p. 14

McClintock, B. H. & Norton, A. A. 2013, Sol. Phys., 287, 215 . . . . . p. 5

Meibom, S., Barnes, S. A., Platais, I., et al. 2015, Nature, 517, 589 . . . . . p. 3

Mengel, M. W., Fares, R., Marsden, S. C., et al. 2016, MNRAS, 459, 4325 . . . p. 6

Miesch, M. S. 2005, Liv. Rev. Sol. Phys., 2, 1 . . . . . p. 14

Moreno-Insertis, F. 1986, A&A, 166, 291 . . . . . p. 19 and 67

Moreno-Insertis, F. 1997, in 1st Advances in Solar Physics Euroconference. Advances in Physics of Sunspots, ed. B. Schmieder, J. C. del Toro Iniesta, & M. Vazquez, Vol. 118, 45–65 . . . . . p. 40

Moreno-Insertis, F., Caligari, P., & Schüssler, M. 1994, Sol. Phys., 153, 449 . p. 15

Moreno-Insertis, F. & Emonet, T. 1996, ApJ, 472, L53 . . . . . p. 40

Moreno-Insertis, F., Schüssler, M., & Ferriz-Mas, A. 1992, A&A, 264, 686 . . p. 10, 19, and 48

Murray, M. J., Hood, A. W., Moreno-Insertis, F., Galsgaard, K., & Archontis, V. 2006, A&A, 460, 909 . . . . . p. 73

Nelson, N. J., Brown, B. P., Sacha Brun, A., Miesch, M. S., & Toomre, J. 2014, Sol. Phys., 289, 441 . . . . . p. 74

Oláh, K. & Kolláth, Z. 1999, in ASP Conf. Ser., Vol. 158, 174 . . . . . p. 5

Parker, E. N. 1955, ApJ, 122, 293 . . . . . p. 9 and 39

Parker, E. N. 1993, ApJ, 408, 707 . . . . . p. 8

Preminger, D., Nandy, D., Chapman, G., & Martens, P. C. H. 2010, Sol. Phys., 264, 13 . . . . . p. 5 and 70

Racine, E., Charbonneau, P., Ghizaru, M., Bouchat, A., & Smolarkiewicz, P. K. 2011, ApJ, 735, 46 . . . . . p. 8

Rädler, K. H., Kleeorin, N., & Rogachevskii, I. 2003, Geo. & Astrophys. Fluid Dyn., 97, 249 . . . . . p. 6

Reiners, A., Schüssler, M., & Passegger, V. M. 2014, ApJ, 794, 144 . . . . . p. 70

Reinhold, T., Reiners, A., & Basri, G. 2013, A&A, 560, A4 ..... p. 71

Rempel, M. 2004, ApJ, 607, 1046 ..... p. 10

Rempel, M. 2006, ApJ, 647, 662 ..... p. 77

Rempel, M. & Schüssler, M. 2001, ApJ, 552, L171 ..... p. 79

Rempel, M., Schüssler, M., & Tóth, G. 2000, A&A, 363, 789 ..... p. 10 and 14

Rüdiger, G. 1989, Differential rotation and stellar convection. Sun and the solar stars (Berlin, Akademie Verlag) ..... p. 3, 24, and 76

Saar, S. 2002, in ASP Conf. Ser., Vol. 277, 311 ..... p. 13, 70, 73, and 74

Schatzman, E. 1962, Annales d'Astrophysique, 25, 18 ..... p. 3

Schüssler, M. 1979, A&A, 71, 79 ..... p. 10, 40, and 42

Schüssler, M. 1983, in Solar and Stellar Magnetic Fields: Origins and Coronal Effects, Vol. 102, 213–234 ..... p. 10

Schüssler, M., Caligari, P., Ferriz-Mas, A., & Moreno-Insertis, F. 1994, A&A, 281, L69 ..... p. 10, 42, and 50

Schüssler, M. & Solanki, S. K. 1992, A&A, 264, L13 ..... p. 19, 31, 36, 44, 46, 50, and 86

Semel, M. 1989, A&A, 225, 456 ..... p. 6

Senthamizh Pavai, V., Arlt, R., Diercke, A., Denker, C., & Vaquero, J. M. 2016, ArXiv e-prints, 1603, arXiv:1603.02510 ..... p. 5

Skumanich, A. 1972, ApJ, 171, 565 ..... p. 3

Spitzer, L. 1962, Physics of Fully Ionized Gases (New York, London, Wiley and Sons) ..... p. 6

Spruit, H. C. 1981, A&A, 102, 129 ..... p. 9

Spruit, H. C. & van Ballegooijen, A. A. 1982, A&A, 106, 58 ..... p. 39

Steenbeck, M. & Krause, F. 1966, Zeitschrift Naturforschung Teil A, 21, 1285 p. 8

Strassmeier, K. G. 2009, A&A Rev., 17, 251 ..... p. 5 and 6

Strassmeier, K. G., Handler, G., Paunzen, E., & Rauth, M. 1994, A&A, 281, 855 p. 70

van Ballegooijen, A. A. 1982, A&A, 113, 99 ..... p. 10

Vidotto, A. A., Gregory, S. G., Jardine, M., et al. 2014, MNRAS, 441, 2361 .. p. 6 and 71

Vogt, S. S. 1981, ApJ, 250, 327 ..... p. 6

Waite, I. A., Marsden, S. C., Carter, B. D., et al. 2015, MNRAS, 449, 8 ..... p. 6

Wang, Y.-M., Colaninno, R. C., Baranyi, T., & Li, J. 2015, ApJ, 798, 50 ..... p. 5

Weber, M. A. & Fan, Y. 2015, Sol. Phys., 290, 1295 ..... p. 48 and 56

Weber, M. A., Fan, Y., & Miesch, M. S. 2011, ApJ, 741, 11 .. p. 11, 15, 73, and 88

Wilson, O. C. 1978, ApJ, 226, 379 ..... p. 5

Wissink, J. G., Hughes, D. W., Matthews, P. C., & Proctor, M. R. E. 2000, MNRAS, 318, 501 ..... p. 10 and 14

Wright, N. J., Drake, J. J., Mamajek, E. E., & Henry, G. W. 2011, ApJ, 743, 48 p. 70

Wright, N. J., Drake, J. J., Mamajek, E. E., & Henry, G. W. 2013, AN, 334, 151 p. x, 5, and 70

Yoshimura, H. 1985, PASJ, 37, 171 ..... p. 54

Zeeman, P. 1897, ApJ, 5, 332 ..... p. 4

Ziegler, U. 2011, J. Comp. Phys., 230, 1035 ..... p. 17

Acknowledgements

As any scientific work, the present thesis is not just the work of a single individual but the result of a collection of experiences, advices, and discussions. For this very reason, I would like to thank a few collaborators and friends, who supported my efforts all along this adventure that has been my PhD study.

First, I would like to thank my supervisors Klaus G. Strassmeier and Rainer Arlt. I want to thank them for their trust in my capacity of carrying out my PhD at the AIP, but most important for the time and energy they have invested in teaching me what it is to be a scientist.

Second, I would like to thank the reviewers for their time and corrections.

Then, I would like to thank Guillaume Ribert for being the only lecturer who encouraged me to follow my dream and become an astrophysicist. I would also like to thank Udo Ziegler, who has been the first scientist who actually gave me the opportunity to enter the world of astrophysics, co-supervising my master thesis.

I would like to further thank a number of colleagues from the AIP: Marcus Gellert, Federico Spada, Sydney Barnes, Senthamizh Pavai Valliappan, Philipp Gast, Andreas Künstler, Erik Johansson and Manfred Küker; but also from all over the world: Laurène Jouve, Jörn Warnecke, Timo Reinhold, Illa R. Losada, Oliver Gressel, Laurent Gizon, Sacha Brun, Axel Brandenburg, and Robert Cameron, for their advices, critics, questions, and for making me feel welcome in such a diverse and healthy community.

Finally, I would like to thank the ones who encouraged me on a more personal level for their patience, unconditional support, and the amount of love they have given me all along these years. I would like to thank Levana, Mum, Eric, Papa, Malia, Thibaut, Kike, Wally, Momo, Oliv, Alex, Theo, Dahlia, Pierro, Gab, Thomas, Tiny, Norman, Tiff, Janusch, Volker, and my Anika.

Selbständigkeitserklärung

Hiermit versichere ich, dass ich die vorliegende Dissertation mit dem Titel
"Dynamics of the rise of magnetic flux tubes in stellar interiors"
selbständig angefertigt, nicht anderweitig für Prüfungszwecke vorgelegt, alle benutzten Quellen und Hilfsmittel angegeben, sowie wörtliche und sinngemäße Zitate gekennzeichnet habe.

Potsdam, den 20. Juni 2016 ....

Yori Fournier